



DISSERTATION

Titel der Dissertation

“Fundamental Characteristics of the
SOI Slot Waveguide Structure”

angestrebter akademischer Grad

Doktor/in der Naturwissenschaften (Dr. rer.nat.)

Verfasserin / Verfasser:	Mag. rer. nat. Paul Müllner
Matrikel-Nummer:	9408217
Dissertationsgebiet (lt. Studienblatt):	A 091 411
Betreuerin / Betreuer:	Ao. Univ.Prof. Dr. Martin Neumann

Wien, am

20.12.10

Contents

1	Introduction	7
2	Fundamentals	9
2.1	Introduction	9
2.2	The infinite 2D slab system	11
2.2.1	The effective index of the two dimensional slot waveguide	13
2.2.2	Fields and Poynting vector of the two dimensional slot waveguide	18
2.3	Types of slot waveguides	26
2.4	Conclusion	30
3	Simulation methods	31
3.1	The Finite Element Method	31
3.2	The Variational Mode Matching method of MaxWave	33
3.3	Comparison of the two methods	34
3.4	General notes on the performed simulations	35
3.5	Perfectly matched layers (PML's)	35
4	Modal behavior	37
4.1	Effective index of the first order odd mode in the 2D case	37
4.2	Mode characteristic of 3D slot waveguides	38
4.2.1	Fundamental characteristics	38
4.2.2	Second order mode characteristic	43
5	Power optimization	47
5.1	Structural optimization	47
5.2	Optimization with respect to single mode behavior	50
6	Leakage behavior of slot waveguides	53
6.1	Substrate leakage	54
6.2	Lateral Leakage	56
6.2.1	Fundamentals	56
6.2.2	Fully symmetric slot waveguide structure	62
6.2.3	Semi-analytic leakage criterion	63
6.2.4	Influence of asymmetries	64

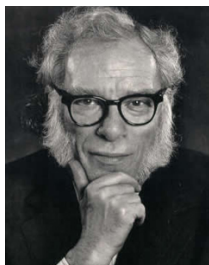
6.2.5	Influence of geometry	64
6.2.6	Resonance effects for slot waveguides with asymmetries	65
6.2.7	Asymmetric slot waveguide structures	68
6.2.8	Influence of imperfections	70
6.3	Conclusion	72
7	Nonlinearities of slot waveguides	75
7.1	Fundamentals	75
7.2	Simulation model and technique	78
7.3	Results	79
7.4	Conclusion	83
8	The V-groove structure	85
8.1	Introduction	85
8.2	Optimization for surface sensing	86
8.2.1	Fundamentals	86
8.2.2	Simulation technique	88
8.2.3	Results of optimization	89
8.3	Optimization for nonlinear effects	91
8.3.1	Fundamentals	91
8.3.2	Simulation results	92
8.4	Application to lasing	93
8.4.1	Fundamentals	93
8.4.2	Simulation results	94
8.5	Feasibility	95
8.6	Conclusion	96
9	Summary	97
	Bibliography	101
	Abstract	113
	Publications	115
A	Effective index approximation	117
B	The variational mode matching (VMM) method Of MaxWave	121
B.1	Introduction	121
B.2	General Information	121
B.3	Detailed Description	122
B.3.1	Perfectly Matched Layers (PMLs)	122

B.3.2 CrossSecWG	122
B.4 1D Waveguide Modes	125
B.5 Matrix Secant Method	127
B.6 Numerical Quadrature	128
Curriculum Vitae	129
Acknowledgment	131

1. Introduction

Optical technologies play a key role in telecommunication since the 1980s, where the first long distance fiber networks have been installed. Over the last decades the importance of optical systems evolved constantly and besides the telecommunication, the computer industry became an important driving force in optics R & D. As the last years revealed, photonic systems meet the demands of industry and customer for high data rates at a sufficient amount of robustness not only for long, but also for mid- and short distance communication. Optical LAN and TOSLINK became common abbreviations in our everyday lives.

In future, the distances where photonic systems are beneficial could become even shorter. Optical interconnects showed high potential to mitigate the communication bottleneck of today's computer technology. Data rates which are hardly possible with electronic devices [1] or elements with



'Welcome everyone to this historic transatlantic crossing – this maiden voyage across the sea on a beam of light...'

First call via the TAT-8, the first transatlantic fiber-optic cable placed by Isaac Asimov in 1988.

low dissipated power compared to state-of-the-art technology components are possible with the use of SOI (silicon on insulator) substrates [2]. The ultra high refractive index contrast of this material system (3.48 of silicon to 1.46 of the insulator silica at a light wavelength of 1.55 μm) allows for a very high level of device integration. With standard semiconductor fabrication processes used in the electronic industry very small structures are possible, e.g. ring resonators which are typically used for frequency selective filtering with a radius of only 1.5 μm have been demonstrated recently [3]. An even more important consequence of the compatibility with electronic production techniques is the feasibility of photonic and electronic elements on one single silicon chip. The ultra high refractive index contrast of the SOI material cannot be seen just as a scaling factor for the device size. Approximations and numerical methods developed for low refractive index difference waveguides lose their validity. This is a potential pitfall in the design, but on the other hand enables unique effects and devices. In particular, photonic crystals have to be mentioned in this context [4]. Their unique characteristics such as negative refractive index or slow light would not be possible in a low refractive index contrast material system.

Another effect that exploits the high index contrast in SOI is the so-called photonic slot effect. First demonstrated in 2004 [5] it attracted much attention during recent years. In a slot waveguide a high fraction of the light power is confined between two silicon cores in a material with lower refractive index. This effect has the potential to enable a completely new generation of laser, modulator or sensing devices.

However, typical slot waveguide structures put high demands on the fabrication process. A feature size of tens of nanometers is still only available for an exclusive group of semiconductor fabs in practice. But the possibilities of semiconductor technology are evolving rapidly and it is foreseeable that this obstacle will be overcome within the next years. Hence, design rules will be needed to enable an efficient layout of a specific slot waveguide structure optimized for a certain application while avoiding afore mentioned pitfalls.

This thesis provides a multiplicity of such design rules for different slot waveguide configurations. In this work the most fundamental and at the same time most important characteristics of slot waveguides are traced back to their origin in Maxwells equations. Crucial aspects such as modal behavior or the influence of particular geometry parameters and configurations are addressed which have not been considered until now. One groundbreaking result arises from the in-depth studies of the horizontal slot waveguide structure. The complex and time-consuming analysis with different numerical methods allows optimization of the structure leading to a slot waveguide with a performance increased by one order of magnitude compared to conventional waveguides with respect to nonlinear applications.

Moreover, for the first time the lateral leakage mechanism is investigated in the context of rib-type slot waveguides. From these studies essential design rules for rib-type slot structures are derived, which are prerequisites in order to realize horizontal rib-type slot waveguides with low losses.

With these results, this work contributes to future developments, where the slot waveguide might become as common and important in integrated optics as rib and wire waveguides in these days.

2. Fundamentals

2.1. Introduction

At first the most fundamental characteristics of the photonic slot waveguide structure are studied using the infinite five layer slab system as simplified model. The goal is to find answers to questions like: 'What is the photonic slot effect?' 'Which parameters have impact on the slot effect?' 'How can I maximize the slot effect in principle?' and last but not least: 'What do Maxwell's equations say to the slot effect?'. For this purpose, an analytic/numeric framework is developed combining rarely used and well known approximation methods allowing qualitative statements about the effective index of the confined mode, the electric and magnetic field distribution and the distribution of the confined optical power.

In the year 2005 the photonic slot effect has been demonstrated for the first time. Xu *et.al.* [5] showed, that by placing two silicon wires close together, for the polarization where the electric field is perpendicular to the slot interfaces, a high percentage of the light power ($\approx 30\%$) can be strongly confined in the slot between the two cores (Fig. 2.1) [7]. This enables a very high light concentration in a very small low refractive index volume, which can not be achieved in conventional waveguiding structures such as wires, channel- and rib waveguides. Analytic calculations and simulations revealed that this effect can be attributed to a true eigenmode of the system, in principle.

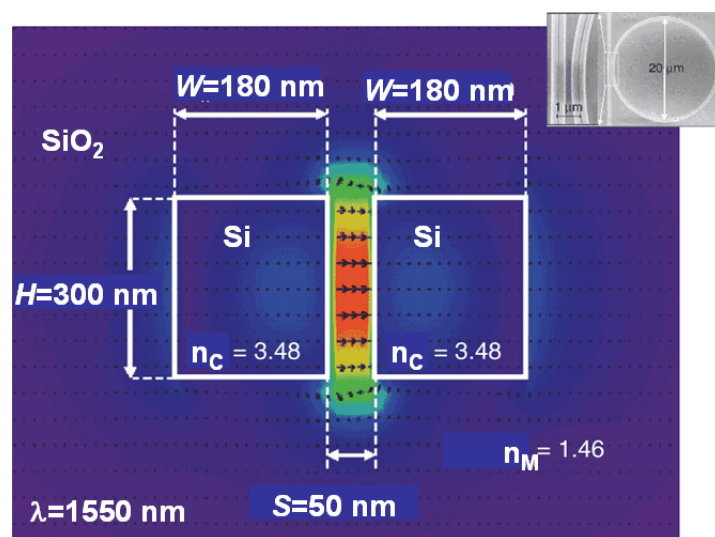


Figure 2.1.: First realized slot structure of [6] using a ring resonator (see inset) to determine the effective index.

In the first experiments a vertical approach was used, where the slot orientation is perpendicular to the substrate surface. Ring resonator- and coupling measurements showed a high difference in the propagation of the TM- (transfers magnetic) to the TE (transfers electric) polarized light propagating within the slotted structure. After comparing these results with simulations it was concluded, that this difference is a clear evidence for the existence of the so called 'slot mode' which corresponds to the mode where the electric field is even with respect to direction perpendicular to the slot interfaces. In the waveguide structure with a vertical orientated slot, the slot mode corresponds to the mode excited by TE polarized light. These first measurements were followed by more detailed investigations of the properties of slot waveguides by several groups [6, 8–85], where their suitability for many different device concepts such as modulators [8–10], emitters [11–14], applications exploiting nonlinear effects [15–27] and sensors [28–35, 86] was studied. In particular, for the exploitation of nonlinear optical effects in low index materials such as polymers, the slot waveguide showed its high potential. But the analysis of the fundamental properties has still not been finished yet. The high refractive index, the three dimensionality and the high degree of freedom of the slot structure degrade - and often lift - the validity of analytical approaches. And even numerical methods commonly used for the analysis of waveguides such as the 3D beampropagation method as well as 2D numerical stringent solutions of Maxwell's equations, namely the finite element (FEM) or the finite difference time domain (FDTD) method reach their limits in terms of applicability or computational effort. The adaptation of existing - as well as the development of new methods for the characterization and the efficient design of slot waveguides for specific applications are still demanded.

2.2. The infinite 2D slab system

Based on the fact, that the slot effect is attributed to a true eigenmode of the waveguide, the investigation of the corresponding infinite slab system is appropriate to study the most fundamental, and at the same time most important characteristics of this structure. Moreover, using approximations for 3D waveguides such as the effective index method [87] rules can be derived allowing a fast waveguide design without the need of time consuming simulations. The theoretical basics of dielectric waveguides have been explained in e.g. [87–92] in all details and are only repeated here as far as it is necessary for comprehension and in particular for the definition of all important parameters. It must be pointed out, that some of the following results are very similar to the work of [7] but in order to enable a continuative analysis and approximations a complete derivation is given here. For a lossless, charge and current free ($\rho = \vec{j} = 0$) isotropic dielectric medium by neglecting the Magnetization M Maxwell's equations reduce to:

$$\vec{\nabla} \times \vec{E} = -\mu_0 \frac{\partial \vec{H}}{\partial t} \quad \vec{\nabla} \times \vec{H} = \epsilon_0 n^2 \frac{\partial \vec{E}}{\partial t} \quad (2.1)$$

where ϵ_0 is the dielectric permittivity, μ_0 the magnetic permeability of free space and n the refractive index of the medium. The assumption that no charge and current are present, are implicitly included in equation (2.1) (see [88]). Supposing plane wave propagation in z -direction with the propagation constant β , the wave equations can be separated in two mutually orthogonal states/modes of polarization:

$$\begin{aligned} 0 &= \frac{\partial^2 E_x}{\partial y^2} + (\omega^2 \mu_0 \epsilon_0 n^2 - \beta^2) E_x & 0 &= \frac{\partial^2 H_x}{\partial y^2} + (\omega^2 \mu_0 \epsilon_0 n^2 - \beta^2) H_x \\ H_y &= \frac{\beta}{\omega \mu_0} E_x & E_y &= -\frac{\beta}{\omega \epsilon_0 n^2} H_x \\ H_z &= \frac{1}{i \omega \mu_0} \frac{\partial E_x}{\partial y} & E_z &= -\frac{1}{i \omega \epsilon_0 n^2} \frac{\partial H_x}{\partial y} \\ H_x &= 0 & E_x &= 0 \\ E_y &= E_z = 0 & H_y &= H_z = 0 \end{aligned} \quad (2.2) \quad (2.3)$$

The left one (2.2) is the so-called transversal electric (TE) mode with the field components E_x , H_y and H_z whereas the set of equation on the right (2.3) describes the transversal magnetic (TM) mode with the field components H_x , E_y and E_z where $\omega = 2\pi c/\lambda$ with c the speed of light in vacuum. The field equations (2.2) and (2.3), respectively, can be solved by using the ansatz:

$$E_x, H_x = a \sin(\gamma y) + b \cos(\gamma y). \quad (2.4)$$

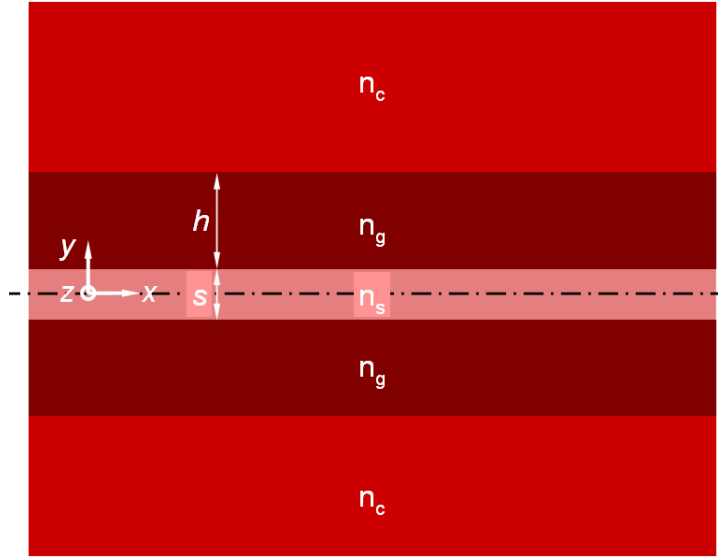


Figure 2.2.: Geometry- and refractive index parameters of a infinite 2D slot waveguide. The propagation direction is in z .

The constants a, b have to be determined from the boundary conditions. By introducing (2.4) to the differential equations in (2.2) and (2.3) one immediately sees that the ansatz (2.4) holds only true if

$$\gamma = k_0 \sqrt{n^2 - n_{\text{eff}}^2}, \quad (2.5)$$

is demanded, where n_{eff} is the so-called effective index which is defined as $n_{\text{eff}} \equiv \beta/k_0$. It has to be noted, that the argument of the square root is not necessarily a positive value, because the refractive index of the involved materials can be larger or smaller than the effective index. The equations (2.2)-(2.5) can now be used to solve a waveguide slab system as sketched in Fig. 2.2. In order to study the fundamental characteristics, it is sufficient to assume a mirror symmetric geometry with the symmetry plane lying in the x - y plane. The symmetry plane is emphasized in Fig. 2.2 as a dash-dotted line. To ensure total internal reflection, $n_g > n_c$ is required. Next, assuming that we are at this point only interested in the TM polarized mode the fields of the three layers can be expressed with equation (2.3), resulting in:

$$H_x(y) = \begin{cases} a_1 \sin(i\gamma_s y) + b_1 \cos(i\gamma_s y) & \text{with } \gamma_s = \sqrt{n_{\text{eff}}^2 - n_s^2} \quad \text{for } y \leq s/2 \\ a_2 \sin(\kappa y) + b_2 \cos(\kappa y) & \text{with } \kappa = \sqrt{n_g^2 - n_{\text{eff}}^2} \quad \text{for } s/2 < y \leq s/2 + h \\ a_3 \sin(i\gamma_c y) + b_3 \cos(i\gamma_c y) & \text{with } \gamma_c = \sqrt{n_{\text{eff}}^2 - n_c^2} \quad \text{for } y > s/2 + h \end{cases} \quad (2.6)$$

where a_i and b_i with $i = 1, 2, 3$ are constants which have to be determined and $y \geq 0$. By assuming that $n_g > n_s$ as well, all square roots are positively defined. Due to the symmetry of the geometry the field is either even ($E_y(-y) = E_y(y)$) or odd ($E_y(-y) = -E_y(y)$). By restricting the analysis to the even mode this leads to $a_1 = 0$. In addition, total internal reflection has to be ensured, which is only in consistency with equation (2.4) for an exponentially decaying field in the surrounding third

layer with $b_3 = a_3 i$. These assumptions simplify equations (2.6) to:

$$H_x(y) = \begin{cases} b_1 \cosh(\gamma_s y) & \text{for } |y| \leq s/2 \\ a_2 \sin(\kappa y) + b_2 \cos(\kappa y) & \text{for } s/2 < |y| \leq s/2 + h \\ a_3 e^{-\gamma_c y} & \text{for } |y| > s/2 + h \end{cases} \quad (2.7)$$

By exploiting the fact, that the fields H_x and E_z are continuous at the interface $y = s/2$ and $y = (s/2 + h)$, this yields the linear equation system:

$$\begin{aligned} b_1 \cosh\left(\frac{\gamma_s s}{2}\right) &= a_2 \sin\left(\frac{\kappa s}{2}\right) + b_2 \cos\left(\frac{\kappa s}{2}\right) \\ \frac{b_1 \gamma_s}{n_s^2} \sinh\left(\frac{\gamma_s s}{2}\right) &= \frac{\kappa}{n_g^2} \left(a_2 \cos\left(\frac{\kappa s}{2}\right) - b_2 \sin\left(\frac{\kappa s}{2}\right) \right) \\ a_2 \sin\left(\kappa \left(\frac{s}{2} + h\right)\right) + b_2 \cos\left(\kappa \left(\frac{s}{2} + h\right)\right) &= b_3 e^{-\gamma_c (s/2 + h)} \\ \frac{a_2 \kappa}{n_g^2} \left(\cos\left(\kappa \left(\frac{s}{2} + h\right)\right) - b_2 \sin\left(\kappa \left(\frac{s}{2} + h\right)\right) \right) &= -\frac{b_3 \gamma_c}{n_c^2} e^{-\gamma_c (s/2 + h)} \end{aligned} \quad (2.8)$$

2.2.1. The effective index of the two dimensional slot waveguide

By eliminating the constants in (2.8), the equation:

$$\tanh\left(\frac{s \gamma_s}{2}\right) = \frac{\kappa n_s^2 (\kappa \sin(h \kappa) n_c^2 + \cos(h \kappa) n_g^2 \gamma_c)}{n_g^2 (\sin(h \kappa) n_g^2 \gamma_c - \kappa \cos(h \kappa) n_c^2) \gamma_s}, \quad (2.9)$$

is obtained. This is a typical transcendent eigenmode equation for layered waveguide systems, allowing the numerical calculation of the effective index. As a first analysis, by setting $s = 0$ one immediately obtains the effective index equation of a symmetric three layer system [87] for a waveguide thickness of $2h/\lambda$ due to the assumption of symmetry in the x - y plane: Figure 2.3 a) shows the effective index according to equation (2.9) compared to the solution of a three layer waveguide system for different relative slot thicknesses s/λ in dependence of the relative waveguide height h/λ . To be consistent with later studies, the eigenmode equation of the asymmetric three layer system was used (see Appendix A). Relative geometry parameters are defined as ratio g/λ with g being an arbitrary length of a waveguide geometry such as height or slot thickness and λ denoting the wavelength. To allow a valid comparison, for the relative thickness of the three layer waveguide $h_3 = 2h/\lambda$ was set, implying at this point that the region of interest is $s \ll \lambda$ and the slot can be seen as perturbation of a standard wire waveguide. Moreover, $n_{gc} = \sqrt{n_g^2 - n_c^2}$ and accordingly $n_{gs} = \sqrt{n_g^2 - n_s^2}$ where n_g is the refractive index of the waveguide, n_s the index of the slot region and n_c the index of the surrounding medium are defined to obtain a normalized expression for the refractive index difference. For all following calculations the refractive index of the waveguide was set to 3.5 and the maximum ultra high effective index difference to $n_{gc,gs} = 3.16$ which corresponds to the index difference between silicon and silicon dioxide. The maximum refractive index difference in practice is given by the difference between silicon and air with $n_{gc,gs} =$

3.35. The calculation of both effective indices was performed using [93]. As Fig. 2.3 a) shows, the presence of the slot has a major impact on the effective index of the structure. Even for very small slot thicknesses such as $s/\lambda = 0.005$ the slot lowers the effective index compared to the three layer system. This difference increases considerably with increasing slot thickness, but converges for large slot thicknesses as the comparison with a three layer system with thickness of $h_3 = h/\lambda$ shows. This can be attributed to the fact, that the coupling between the two waveguiding cores is decreased and for $s \gg \lambda$ no coupling remains. The structure exhibits the same effective index as two independent waveguides. In addition, a strong dependence of the effective index on the waveguide height for $h \approx \lambda$ is apparent.

In Fig. 2.3 b) the impact of the slot refractive index (solid) and the index of the surrounding medium (dashed) on the effective index of the structure is plotted for a fixed slot thickness of 0.03. The influence of the refractive indices is of the same order. For small waveguide heights and lower index difference between the waveguide and the surrounding medium compared to the waveguide and the slot material, the gradient for the surrounding medium is even smaller with respect to the height. Again, this indicates the strong impact of the slot region.

In order to compare the slot waveguide directly with a three layer model, in Fig. 2.4 a) the difference between the effective index of the slot waveguide and the three layer model $\Delta n = n_{\text{slot}} - n_3^{h,2h}$ with a thickness of $h_3 = h/\lambda$ and $h_3 = 2h/\lambda$ is plotted corresponding to the dashed and the full lines, respectively. The effective index is always between the effective indices of the three layer model with the two different thicknesses. An even more important characteristic of slot waveguides is the occurrence of extrema at a certain waveguide height, where the impact of the slot is at a maximum. It has to be pointed out, that the extrema are reached for waveguide heights well below $h/\lambda = 0.2$.

In addition, this property shows only a very weak dependence on the slot thickness. For a slot

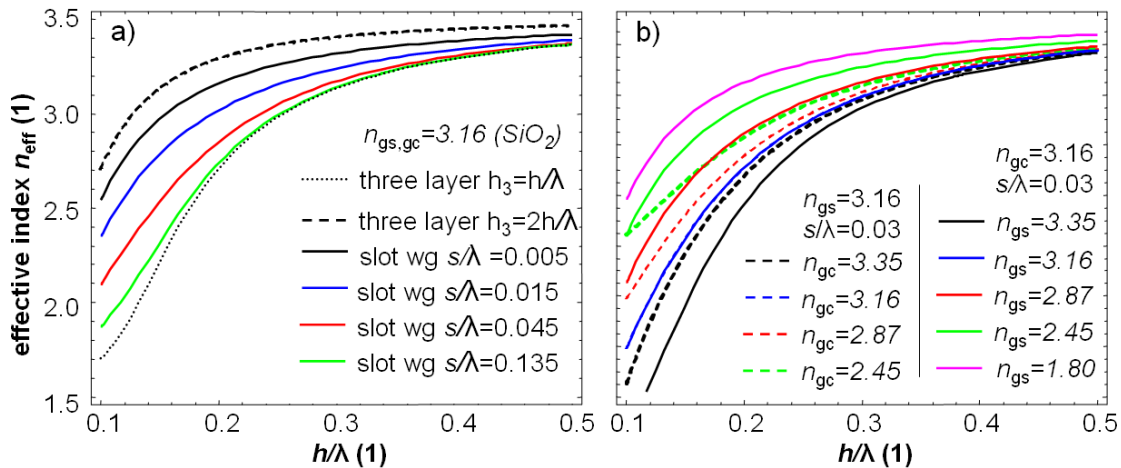


Figure 2.3.: Comparison of the 2D slot waveguide slab effective index (solid lines) with the effective index of a three layer system with thickness h/λ (pointed line) and thickness $2h/\lambda$ (dashed lines) for a) different slot thicknesses and b) different refractive index differences $n_{\text{gs,gc}}$ in dependence of the waveguide height h .

thickness change of more than one order of magnitude, the waveguide heights where this extrema are reached only shift by 4%. To analyze the impact of the refractive index of the slot medium, the same procedure as in Fig. 2.4 a) was used, but for Fig. 2.4 b) the relative slot thickness was set to a constant small value of $s/\lambda = 0.005$. Instead, the refractive index difference of the slot was varied between $n_{gs} = 3.35$ and $n_{gs} = 1.8$. The refractive index ratio of the surrounding medium was kept at $n_{gc} = 3.16$. As depicted in Fig. 2.4 b), the dependence of the effective index on the refractive index of the slot is inverted compared to the dependence on the slot thickness. The maximum impact of the slot is reached for the smallest slot refractive index and decreases with higher values of n_s . Again, the dependence of the effective index difference on the waveguide height undergoes an extremum. Here, the shift of the waveguide height where this minimum is reached is significantly more pronounced. However, the transcendent characteristic of the equation (2.9) inhibits a general, qualitative statement. The numerical evaluation of the effective index provides results for certain structures, but like a *black box* it gives no information about how the slot influences the effective index of the slot waveguide structure. Thus, is it possible to find an approximation where the slot effect directly can be 'seen'? In fact, this is possible with the use of the analytic approximation for the effective index of [94] as described detailed in Appendix A. This approximation can be applied to the symmetric slot waveguide structure and an asymmetric three layer waveguide system with the waveguide thickness $h_3 = h$ where the waveguiding layer was terminated at one side by the slot material with the refractive index n_s and at the others side by the surrounding material of the slot waveguide with the index n_c (see Appendix A). To enable a qualitative analysis only the first term involving s and/or h can be kept, which leads to an approximate solution for the effective indices of the form:

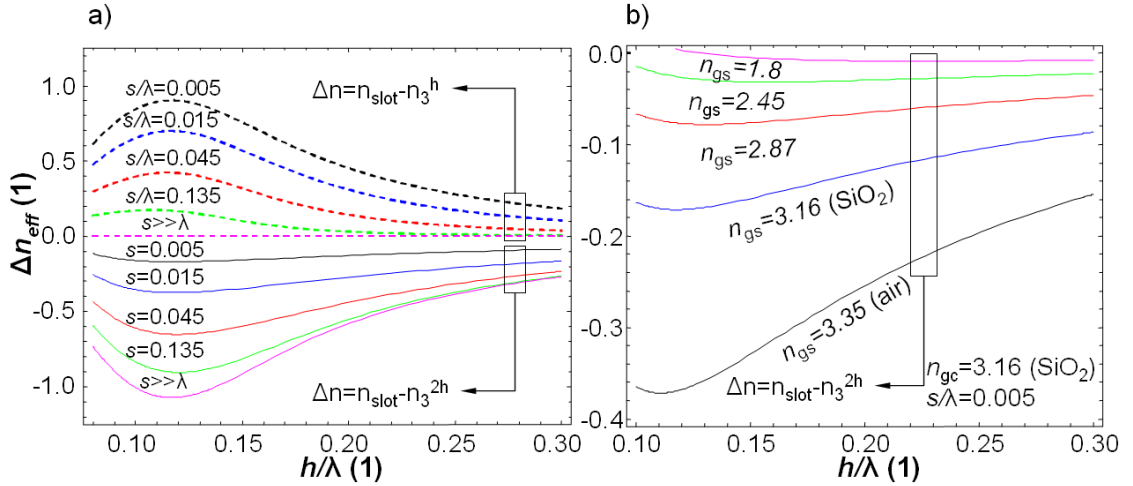


Figure 2.4.: Effective index difference between a slot waveguide and a wire with a) the heights h/λ and $2h/\lambda$ for different slot thicknesses and b) for a wire height of $2h$ for various refractive index differences n_{gs} . Both plots are in dependence on the waveguide height h .

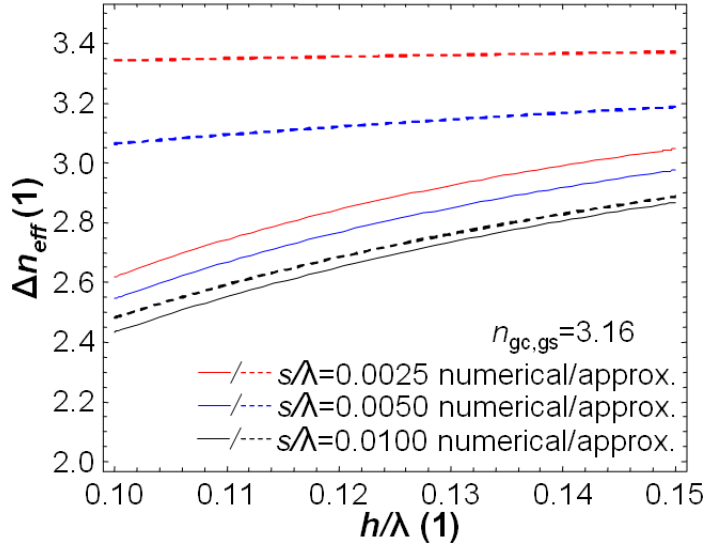


Figure 2.5.: Comparison of the effective index calculated using the numerical correct equation of (2.9) (solid lines) with the approximation of (2.10) (dashed lines) for different slot thicknesses in dependence on the waveguide height h .

$$\text{slot: } n_{\text{eff}} = \sqrt{n_g^2 - \left(\frac{\pi}{hk_0 + \frac{n_c^2}{n_g^2 n_{gc}} + \frac{n_s^2 \coth(k_0 n_{gs} s/2)}{n_g^2 n_{gs}}} \right)^2} \quad (2.10)$$

$$\text{three layer: } n_{\text{eff}} = \sqrt{n_g^2 - \left(\frac{\pi}{hk_0 + \frac{n_c^2}{n_g^2 n_{gc}} + \frac{n_s^2}{n_g^2 n_{gs}}} \right)^2} \quad (2.11)$$

In (2.11) n_s denotes the refractive index of an infinite second layer on the opposite side of the waveguide with respect to the layer with the refractive index n_c (see Fig. A.1 in Appendix A). From the first order approximation in fact only qualitative statements can be deduced, as Fig. 2.5 shows. Here, as comparison the numerical solution of the effective index for the slot waveguide according to equation (2.9) is plotted (full lines) with the approximation given in equation (2.10) (dashed lines) for different relative slot thicknesses. The refractive index difference between silicon and silicon dioxide of $n_{gs,gc} = 3.16$ was used.

The numerical solution the approximation match fairly well only for a relative slot thickness of $s/\lambda = 0.01$ and relative heights $h/\lambda > 0.13$. Nevertheless, the approximation is similar enough to the numeric solution allowing qualitative statements. From Fig. 2.4 a) and b) it now can be concluded, that the interesting regime of the slot waveguide is around $h/\lambda \approx 0.16$ for small slot thicknesses below the waveguide thickness $s < h$ where the impact of the slot on the effective index is maximum. In order to take the properties of the coth function into account it must be demanded that the slot thickness is sufficiently large $s > 0$. Restricting the analysis to this region and assuming an ultra high refractive index material, all three terms in the denominator are of the same order.

By comparing the equations (2.10) and (2.11) one immediately finds that the first two terms in the denominator are identical and only the third term differs. Therefore, the influence on the effective index of the three terms can be identified as follows: In the first term $k_0 h$ the waveguide thickness h appears, which results in an increase of the effective index for increasing waveguide thickness. The second term solely depends on the indices n_g and n_c , where a increase of the difference between the refractive index of the waveguide and the surrounding medium results in a significant decrease of the effective index. This is consistent with standard waveguides such as wires and ribs operated with TM polarized light as the comparison with equation (2.11) shows.

The third term determines the slot effect involving the slot thickness s and the refractive indices n_g and n_s . From the strictly monotonical decrease of the coth function for increasing slot thicknesses follows a decrease of the effective index. Moreover, for values of $s \gg \lambda$ the coth function converges to 1 and equation (2.10) becomes identical to equation (2.11). This reflects the transition of the strongly coupled waveguiding system to the case of two completely separate waveguides. For a high refractive index material and a slot waveguide thickness of around $s \approx 0.01$ the coth function value can exceed 1 and the third term dominates over the second term involving the indices of the waveguide and the surrounding medium. In this case, the index difference between the refractive index of the waveguide and the refractive index of the slot becomes crucial. With increased index difference, for a fixed small slot thickness the effective index strongly decreases due to the cumulative effect of the refractive index difference n_{gc} in- and outside of the coth function.

2.2.2. Fields and Poynting vector of the two dimensional slot waveguide

From the equations (2.8) three of the four constants a_1 , a_2 , a_3 and b_2 can be obtained. One constant remains undetermined allowing normalization. The solution of the equations (2.8) for the transverse magnetic field component H_x of the even slot mode denotes as:

$$H_x(y) = a_1 \begin{cases} \cosh(\gamma_s y) & y \leq s/2 \\ \left(\cosh(\gamma_s a) \cos(\kappa(|y| - s/2)) + \frac{n_g^2 \gamma_s}{n_s^2 \kappa} \sin(\kappa(|y| - s/2)) \sinh(\gamma_s a) \right) & s/2 < y \leq s/2 + h \\ \left(\cosh(\gamma_s a) \cos(\kappa h) + \frac{n_g^2 \gamma_s}{n_s^2 \kappa} \sinh(\gamma_s a) \sin(\kappa h) e^{(-\gamma_c(|y| - h - s/2))} \right) & y > s/2 + h \end{cases} \quad (2.12)$$

For the following studies relative results are sufficient. Therefore, a_1 contains various parameters, which are constant over all layers (slot-, waveguide- and surrounding cladding layer) such as ω , β or ϵ_0 . From (2.12) the relative electric fields can be calculated using $E_y \propto H_x/n_l^2$ where l is the according layer $l = s, g, c$. Furthermore, the Poynting vector for this pure TM mode with real-valued fields can be calculated by:

$$S = E_y H_x. \quad (2.13)$$

With this relation, the relative Poynting vector for the even slot mode reads as:

$$S_z(y) = a_1 \begin{cases} \frac{1}{n_s^2} (\cosh(\gamma_s y))^2 & y \leq s/2 \\ \frac{1}{n_g^2} \left(\cosh(\gamma_s a) \cos(\kappa(|y| - s/2)) + \frac{n_g^2 \gamma_s}{n_s^2 \kappa} \sin(\kappa(|y| - s/2)) \sinh(\gamma_s a) \right)^2 & s/2 < y \leq s/2 + h \\ \frac{1}{n_c^2} \left(\cosh(\gamma_s a) \cos(\kappa h) + \frac{n_g^2 \gamma_s}{n_s^2 \kappa} \sinh(\gamma_s a) \sin(\kappa h) e^{(-\gamma_c(|y| - h - s/2))} \right)^2 & y > s/2 + h \end{cases} \quad (2.14)$$

Apart from the effective index equation (2.9), equations (2.12)-(2.14) are the fundamental relations for the characterization of the symmetric two dimensional slot waveguide. In the following only relative results are necessary and the remaining constant a_1 can be set to 1. On the basis of the results of the preceding section, the slot thickness s and the waveguide height h are chosen around the region, where the effective index showed maximum impact on the effective index compared to a two dimensional three layer waveguide. In Fig. 2.6 a), E_y is plotted for a symmetric slot waveguide with a fixed slot thickness of $s/\lambda = 0.05$ and a refractive index contrast of $n_{gs,gc} = 3.16$ for three different relative waveguide heights of $h/\lambda = 0.05$, $h/\lambda = 0.15$ and $h/\lambda = 0.25$. All plotted fields are normalized to E_y at $y = 0$. In Fig. 2.6 a) at first the strong discontinuity of the field at the interfaces is remarkable. This arises from the fact that $D \propto n^2 E$ component perpendicular to the interfaces must be continuous. This results in a strong discontinuity of the electric field component E_y for an ultra high refractive index contrast waveguide. For waveguides with a very small waveguide height $h/\lambda = 0.05$ (red line) the discontinuity at the interface between the waveguide and the surrounding material is high and E_y decays very slowly in the surrounding medium with respect to y . This behavior is identical to standard waveguides such as wires ribs, etc. operated close to the cutoff where the light is hardly confined in the waveguide structure.

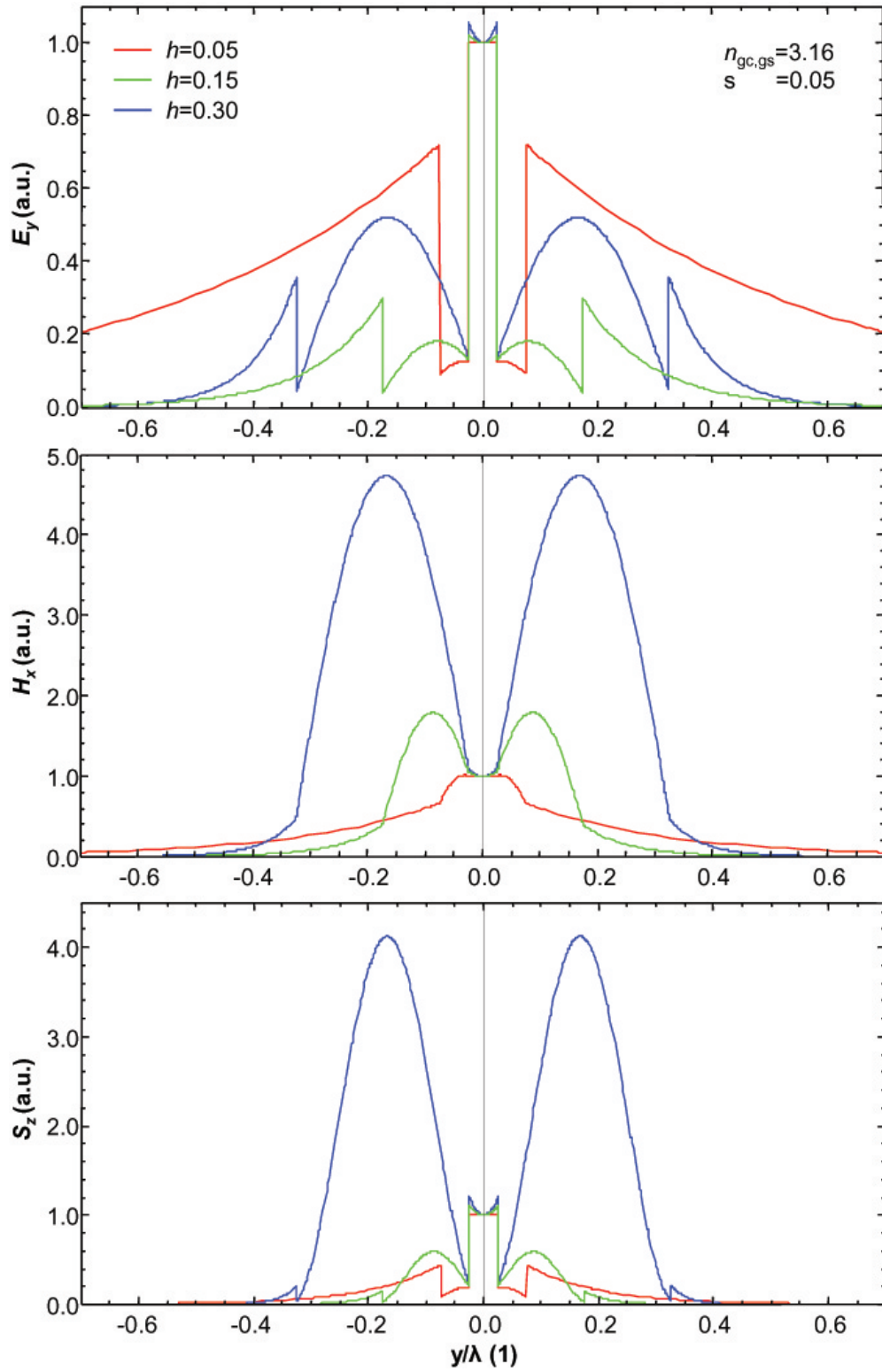


Figure 2.6.: In a) the electric field component E_y in b) the magnetic field component H_x and c) the Poynting vector in the propagation direction z of a slot waveguide for three different heights for a fixed slot thickness and refractive index differences in dependence on the y -coordinate (normalized to λ) perpendicular to the slot interfaces are plotted.

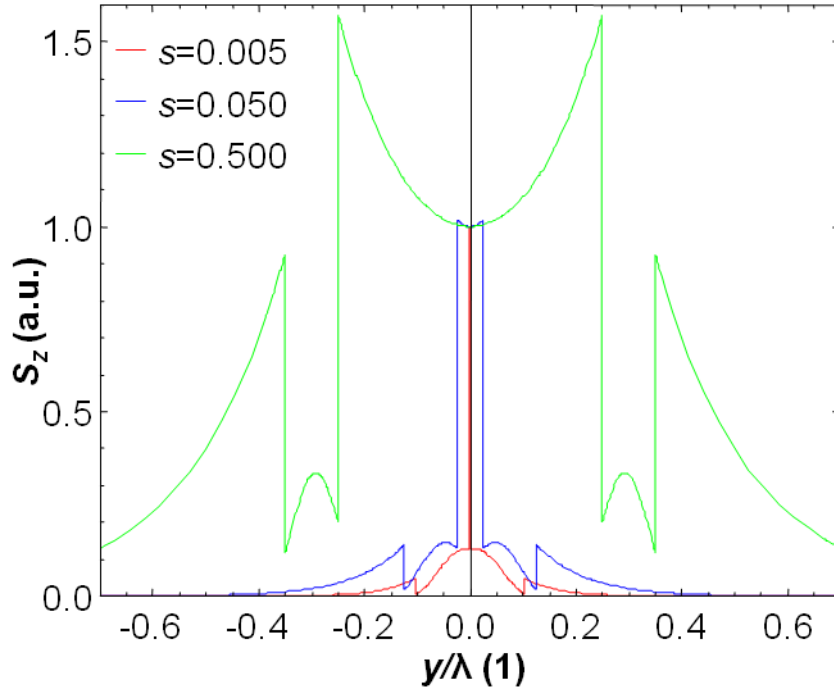


Figure 2.7.: Poynting vector component S_z for a slot thickness of three orders of magnitude in dependence on the y -coordinate (normalized to λ) perpendicular to the slot interfaces.

On the other hand, for waveguides with $h/\lambda \gg 0.05$ as represented by the blue line for $h/\lambda = 0.3$ the discontinuity of the E_y at the outward interface is small. Instead, the field shows a more distinct local maximum in the waveguide indicating that the light is better confined for this set of parameters. Finally, for the green line the height $h/\lambda = 0.15$ is in the region, where the influence of the slot region on the effective index is maximum as the comparison with the three layer system revealed (see Fig. 2.4). Here, the maximum in the waveguide is still small compared to the field of $h/\lambda = 0.3$ and the field in the surrounding material decays much faster than for $h/\lambda = 0.05$.

In contrast to the electric field component E_y the magnetic field H_x must be continuous at the interfaces, as shown in Fig. 2.6 b) plotting again the profile for three heights $h/\lambda = 0.05$, $h/\lambda = 0.15$ and 0.3 . Only for very small slot thicknesses of $h/\lambda = 0.05$, the magnetic field shows a maximum in the slot region. Similar to the electric field, the magnetic field decays very slow in the surrounding material. For higher waveguide heights $h/\lambda = 0.15$ and $h/\lambda = 0.3$ the maxima in the waveguide material are much more pronounced compared to the electric field. Recalling that in this two dimensional case the Poynting vector is proportional to the multiplication of the two transverse fields, (2.13) the enhanced maxima of the magnetic field in the waveguide lead to an increase of this characteristic in the Poynting vector profile as well. Figure 2.6 c) shows that the maximum of the Poynting vector in the waveguide significantly exceeds the local maximum in the slot region for a waveguide height of $h/\lambda = 0.3$.

Nevertheless, for a waveguide height of $h/\lambda = 0.15$ still the absolute maximum is located in the slot region with the low index material. This distribution stays constant over a wide range of slot thicknesses. In Fig. 2.7, the z -component of the Poynting vector for three different slot thicknesses

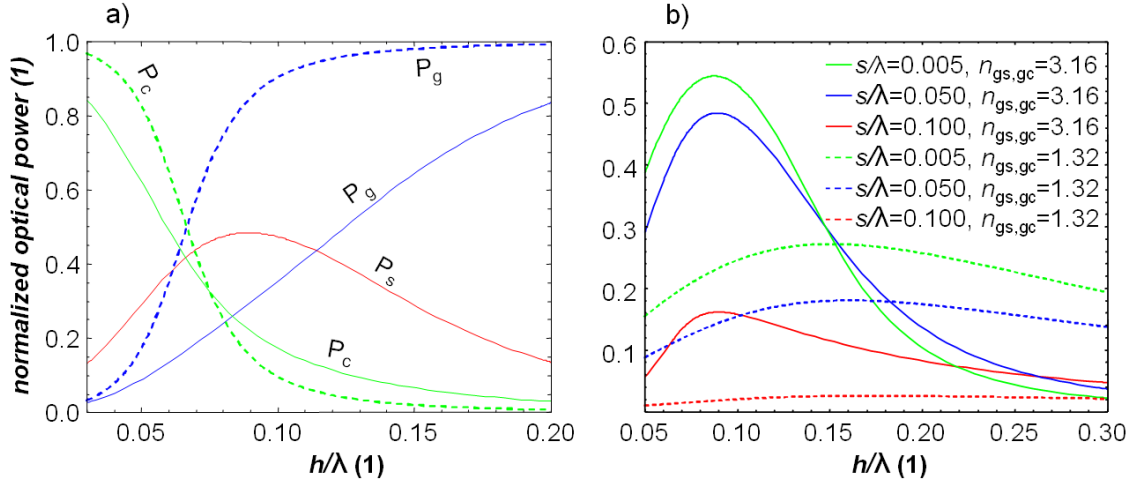


Figure 2.8.: a) Optical power in the different layers of the slot waveguide structure with $s/\lambda = 0.05$ (solid lines) in dependence on the height h . For comparison, the optical power of a slab waveguide corresponding to a slot thickness of $s = 0$ is plotted (dashed lines). The refractive index differences $n_{gs,gc} = 3.16$ is constant. b) Optical power in dependence of the height h for different slot thicknesses s and refractive index differences $n_{gs,gc}$.

over two orders of magnitude $s/\lambda = 0.005$, $s/\lambda = 0.05$ and $s/\lambda = 0.5$ is depicted. Only for the slot thickness $s \gg h$ a noticeable change of the Poynting vector in- and outside of the slot region can be observed. It has to be noted, that the waveguide height was fixed at $h/\lambda = 0.015$ and no interdependence between the slot thickness and the height has been considered. In fact, such interdependences cannot be neglected in the analysis of the slot waveguide structure, increasing the necessary effort as will be pointed out later in this work. In order to overcome this problem the optical power distribution between the different regions is studied by integrating the Poynting vector over the corresponding layers:

$$P_l = \int_{y_1}^{y_2} S_z(y) dy \quad (2.15)$$

where the integration must be restricted to the layer l , where the according equation of 2.14 is valid. The integration can be carried out analytically resulting in:

$$\begin{aligned} P_s &= \frac{s\gamma_s + \sinh(s\gamma_s)}{4\gamma_s n_s^2} \\ P_g &= \frac{1}{4\kappa^3 n_g^2 n_s^4} (-\kappa^2 n_s^4 \cosh(a\gamma_s)^2 (-2h\kappa - \sin(2h\kappa)) + \\ &\quad + \gamma_s n_g^2 (\gamma_s n_g^2 (2h\kappa - \sin(2h\kappa)) \sinh((s/2)\gamma_s)^2 - 2\kappa n_s^2 \sin(h\kappa)^2 \sinh(s\gamma_s))) \\ P_c &= \frac{1}{2\gamma_c n_c^2} (\cos(h\kappa) \cosh((s/2)\gamma_s) + (\gamma_s n_h^2 \sin(h\kappa) \sinh((s/2)\gamma_s)) / (\kappa n_s^2))^2 \end{aligned}$$

The relative power in any layer can now be written as:

$$P_{s,g,c}^{norm} = P_{s,g,c} / P_{sum}, \quad (2.16)$$

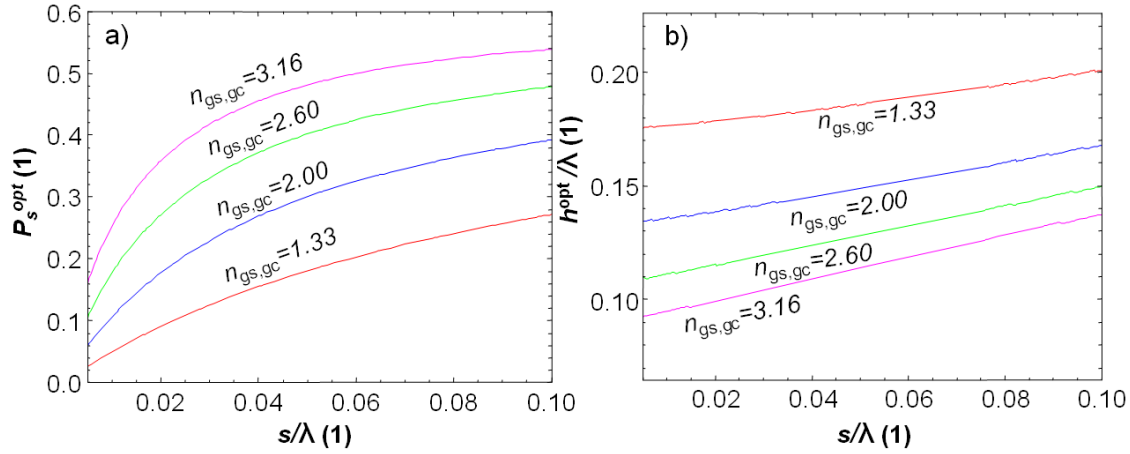


Figure 2.9.: a) Fraction of the optical power P_s^{opt} confined in the slot region for an optimized slot waveguide structure for maximum confinement with respect to the waveguide height h . b) corresponding optimized height h^{opt} . Both plots are in dependence of the slot thickness s .

with $P_{s,g,c}$ being the optical power of the according layer normalized to P_{sum} the sum of all optical powers $P_{sum} = P_s + P_g + P_c$. Figure 2.8 a) shows the normalized power distribution of the different layers evaluated using (2.16) with (2.16) for a slot thickness of $s/\lambda = 0.05$ (full lines). In addition, the power distribution of a three layer waveguide model corresponding to a slot thickness of $s = 0$ (dashed lines) is shown. For both calculations a constant index ratio of $n_{gs,gc} = 3.16$ was assumed. From this direct comparison one sees, that for small waveguide heights, the light power in the slot mainly arises from a shift of the light power from the surrounding material to the slot region, whereas for increased waveguide heights compared to the three layer waveguide, the power becomes more diverted from the waveguide cores.

The most important characteristic in Fig. 2.8 a) is the occurrence of a distinct maximum optical power in the slot for a certain waveguide height. This is a typical characteristic of slot waveguides and holds true over a wide range of parameters as Fig. 2.8 b) shows. Here, the optical power in dependence of the relative height is shown for different slot thicknesses s/λ and index differences $n_{gs,gc}$. Only for structures, with a low refractive index difference and a high slot thickness corresponding to an only weakly coupled system, no distinct maximum is observed (see red dashed line in Fig. 2.8 b) with a refractive index difference of $n_{gs,gc} = 1.32$ and a slot thickness of $s/\lambda = 0.1$). For strongly coupled slot waveguides, which are typically the waveguides of interest, this enables an optimization with respect to the height, in order to find an optimized structure, where maximum optical power is confined in the slot region. Figure 2.9 a) depicts the optimized light power P_s^{opt} of such an optimized structure for four different refractive index differences of $n_{gs,gc} = 1.33$, $n_{gs,gc} = 2$, $n_{gs,gc} = 2.6$ and $n_{gs,gc} = 3.16$ in dependence of the slot thickness s . With increasing slot thickness, the confined light power increases in the slot region. In contrast, with increasing refractive index in the slot region the light power decreases. The difference of the confined slot light power between a waveguide filled with a low refractive index material and a high refractive index material in the slot region can exceed a factor of 5. The optimized height h^{opt} , where the maximum of the light power is reached, is shown in Fig. 2.9 b). The dependence on the slot thickness is relatively weak. A

change of approximately one order of magnitude results only in a change of 0.05 in the optimized thickness. Contrary, with increasing refractive index, the optimized height decreases, whereas the optimized height for a refractive index difference of 3.16 is almost one half of h^{opt} compared to a refractive index difference of 1.33.

Apart from the refractive index of the slot, the refractive index of the surrounding medium has a significant impact on the confined light power in the slot region. In Fig. 2.10 a) the refractive index between waveguide and slot was fixed to 3.16. For a high refractive index contrast to the surrounding medium of 3.35 more than 70% of the optical power can be confined in the slot region. Furthermore, a strong dependence on the slot thickness for small s is prominent. With increasing slot thickness the power in the slot converges. This is in accordance with the fact that for increasing slot thickness the two waveguiding cores are increasingly decoupled. For a refractive index of the surrounding medium which is lower than the refractive index of the slot region, the light power undergoes a distinct maximum and converges to a lower value.

The Fig. 2.10 b) depicts the corresponding optimized heights. An almost linear dependence of the optimized height on the slot thickness becomes apparent. Remarkable is, that the influence on the slot thickness depends on the refractive index difference between the waveguide and the surrounding medium n_{gc} . For higher index differences, the optimized height h^{opt} decreases, whereas for a relatively low index difference of 2.87 h^{opt} increases with the slot thickness s . For refractive index differences between these two values, an n_{gc} can be found, for which h^{opt} is almost independent of the slot thickness (e.g. for $n_{gc} = 3.16$). The high optical power in the slot region is one of the most important characteristics of slot waveguides, which can be maximized by increasing the slot thickness. In fact forcing light into a low refractive index medium is also possible for standard waveguides such as wires and ribs by operating them close to the cutoff. The disadvantage is that the light is distributed over a large cross-sectional area with a low light density in the low refractive index medium.

However, for many applications such as amplifiers or for the efficient exploitation of nonlinear

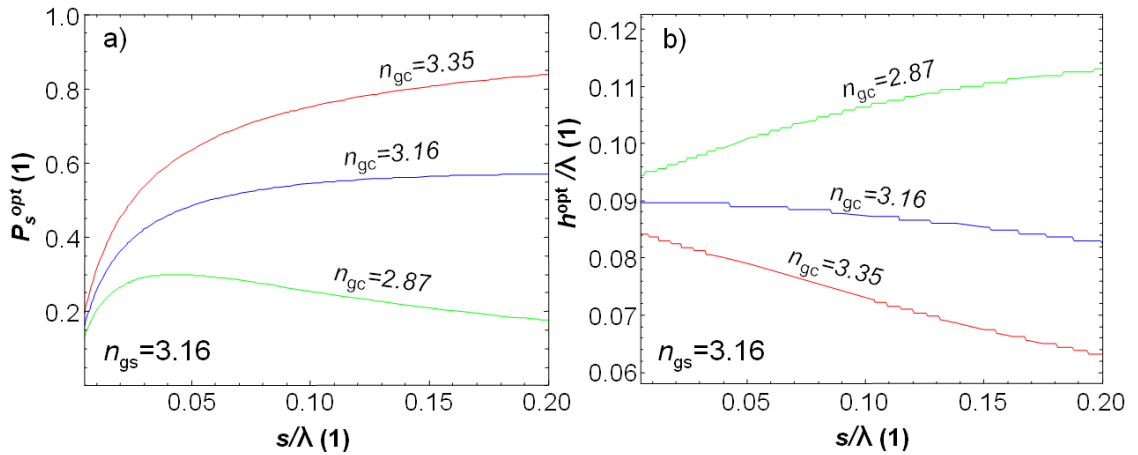


Figure 2.10.: Optimized slot waveguide structure for different values of n_{gc} : a) optimized power P_s^{opt} and b) corresponding optimized height h^{opt} at which the power maximum is reached.

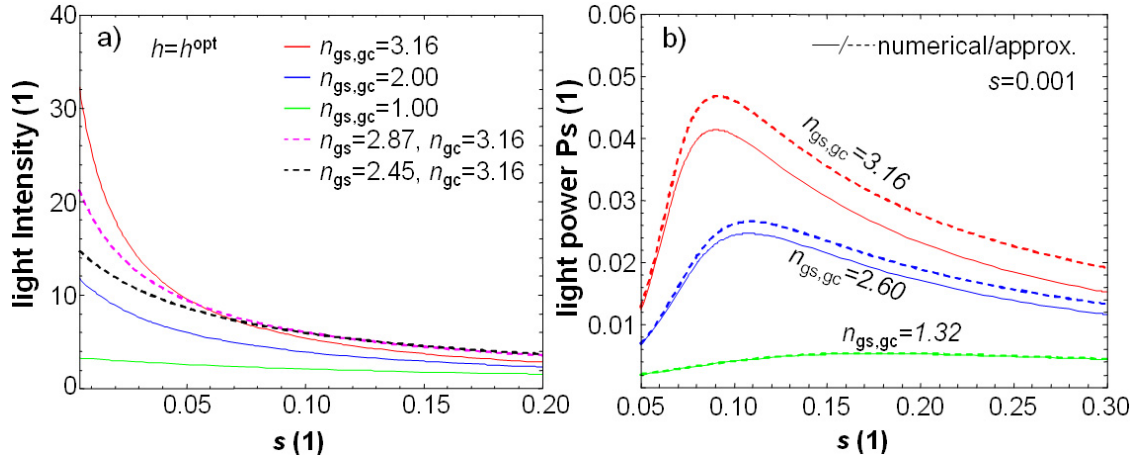


Figure 2.11.: a) light intensity in the slot region I_s for different refractive index differences n_{gs} and n_{gc} in dependence on the slot thickness s . The height of the slot waveguide structure corresponds to the optimized height h_{opt} , where the maximum of the intensity is reached as well. b) comparison of the numerical correct solution of the power in the slot according to (2.16) (solid lines) with the approximation of equation (2.18) (dashed lines).

effects a high power density is crucial, and here the slot waveguide structure shows its high potential. By defining the light intensity in the slot region as:

$$I_s = P_s^{norm}/s. \quad (2.17)$$

The light density can easily be calculated from equation (2.16). Evaluation of this relation shows, that the intensity is strongly dependent on the refractive index difference (see Fig. 2.11 a)). A slot waveguide with a waveguide refractive index difference of $n_{gs,gc} = 3.16$ to the slot- and the surrounding medium, shows an approximately one order of magnitude higher light intensity compared to a waveguide with a refractive index difference of 1. For a fixed index difference between the waveguide and the surrounding medium of $n_{gc} = 3.16$ with decreased slot refractive index difference, of $n_{gs} = 2.87$ and $n_{gs} = 2.45$ (dashed lines in Fig. 2.11 a)), the intensity is considerably lower, but still a slot effect is present for small slot thicknesses. For large s , the higher refractive index results in an increased confinement of the light, which explains the higher intensity compared to a slot waveguide with lower slot refractive index. The light intensity in the high refractive index difference case is much higher than in conventional waveguides as ribs and wires, and even higher than in so-called ARROW waveguides (as described in [7]). Finally, to allow for qualitative statements, where the slot effect has its origin, a first order Taylor series expansion around $s = 0$ is performed for the first equation of (2.16). This results in:

$$P_{s,Taylor}^{rel} = \frac{2\gamma_c \kappa n_c^2 n_g^2 s}{n_s^2 (2\kappa n_g^2 \cos((s/2 + h)\kappa)^2 + \gamma_c n_c^2 (2(s/2 + h)\kappa + \sin(2(s/2 + h)\kappa)))}. \quad (2.18)$$

Figure 2.11 b) shows a comparison of the analytically correct formulation of the light power in the slot P_s^{rel} according to equation (2.16) and its approximation (2.18) for a relative slot thickness

of $s = 0.001$. A very high accordance is achieved for low refractive index differences between the waveguide and the surrounding/slot medium. With increase of the refractive index difference, the deviations increase, but still a similar qualitative behavior can be observed. The two trigonometric functions involving the waveguide height in their argument result in the observed maximum at a certain value of h . Moreover, the refractive index in the slot region appears in the denominator as well, leading to an increase of the power in the slot with decreasing its refractive index.

2.3. Types of slot waveguides

From the preceding sections it can be concluded, that in the 2D case, in order to obtain a high slot effect, materials allowing for an high index contrast along with optimized waveguide height has to be ensured. In addition, in order to obtain a maximized intensity, a small slot thickness $s \ll \lambda$ is important. This limits the choice of a high refractive index material in practice because a high refractive index and good process ability to enable a feature size much smaller than the wavelength at a low degree of absorption is demanded.

SOI (silicon on insulator) fulfills these demands to a high degree. The refractive index of $n_{Si} = 3.48$ in the near infrared wavelength region is exceptional and in fact, almost any other material compared to silicon has a low refractive index allowing for an ultra high refractive index difference. In particular polymeric materials with refractive indices between 1.45 – 1.6 have to be mentioned in this context. Moreover, silicon is the foundation of electronics. This means that all technology processes developed for the micro- and nanometer range of electronic devices can be used directly for the realization of silicon photonic components. This advantage is striking because, for the realization of devices based on this ultra high index contrast material technologies such as e-beam or deep UV lithography are a prerequisite.

Therefore, almost all further studies in this work will assume SOI as material system. This entails firstly, that the waveguiding material is silicon, which is in consistence with an overwhelming majority of studies up to now. Secondly, the substrate material is silica SiO_2 with $n_{SiO_2} = 1.46$ typically used as insulator layer below the silicon waveguide layer for all available SOI substrates. Thirdly, due to the material characteristic of monocrystalline silicon, the interesting wavelength region is located in the near infrared where the refractive index of silicon is $n_{Si} = 3.48$. Below $\lambda = 1100$ nm silicon is strongly absorbing. Moreover, for the standard telecommunication wavelength of $\lambda = 1550$ nm high quality laser diodes are readily available. Thus, a wavelength around $\lambda = 1550$ nm was assumed for the following in-depth studies.

However, the step from the two dimensional to the three dimensional slot waveguide necessitates a limitation of the waveguide structure (as e.g. for a wire) or at least a modulation of the waveguide height (leading to a rib waveguide) in the third dimension x .

From this, slot waveguide structures as summarized in Fig. 2.12 are possible, in principle. All these structures are studied with respect to several important characteristics within this thesis, and as will be pointed out, some of them are subject to restrictions in terms of practical use.

I. Vertical slot waveguides

The first practical implemented slot waveguide [5] slot waveguide is referred to as vertical slot waveguide with a slot perpendicular to the substrate interface. The major advantage of this type is that only one monocrystalline silicon layer is necessary for the fabrication. In addition, for the slot material a depositable material is not demanded. Any material that ensures an entire filling of the slot region can be used to fill the gap between the two high index cores. On the other hand, in practice it is not possible to incorporate a different material for the upper surrounding area of the slot waveguide. The material of the slot always will

surround the waveguide. Moreover, for the fabrication of a vertical slot waveguide, typically e-beam, or at least with significant effort deep-UV lithography has to be used [17].

a) Wire based

For the wire based slot waveguide (see Fig. 2.12 I. a)) the restriction to e-beam lithography leads to an increase of fabrication cost and to a limitation of the slot thickness to approx. 50 nm due to the necessary lithography process. In addition, the etch step leaves rough side walls at the slot interfaces. Since the light intensity is at maximum at the slot interfaces. Therefore, vertical slot waveguides are prone to high scattering losses.

b) The V-groove waveguide

Another kind of vertical slot waveguide is the so called V-groove waveguide proposed in [85] shown in Fig. 2.12 I. b). The acute angle in the center of the structure leads to a strong confinement at the bottom of the waveguide. An additional advantage arises from increased width on top of the slot compared to a vertical slot structure of Fig. 2.12 I. a). This could ease the problems of filling a narrow slot of the order of tens of nanometer. The realization of such a structure is a challenging task, but V-grooves of similar size have been realized successfully in the past in the context of electronics [95–97]. The other advantages and disadvantages are the same as for 2.12 I. a).

II. Horizontal slot waveguides

In contrast to the vertical slot waveguide for the horizontal slot waveguide a second high index layer is indispensable. This makes bonding techniques [42, 98] or the deposition of a second high refractive index layer e.g. amorphous silicon [41, 99] necessary. This holds true for the slot material. Here, only a depositable material where the thickness can be sufficiently controlled can be used. On the other hand, from this disadvantage follows one important advantage of the horizontal slot waveguide, studied in-depth for the first time in [57]: All slot interfaces border to deposited layers, which typically have smooth surfaces. In addition, the thickness of the slot is only limited by the controllability of its deposition. Even layer thicknesses in the nanometer range are conceivable.

Due to the layered configuration it is possible to cover the slot waveguide with a different material with respect to the slot. By using air as cladding, one can achieve an ultimately high index contrast. Furthermore, the requirements in terms of realization are significantly relaxed, because the smallest feature size for the lithography is given by the width of the slot waveguide and not by the one order of magnitude smaller slot. This enables the use of faster and cheaper fabrication methods than e-beam such as deep-UV lithography. Finally, the high achievable width-to-height ratio has to be mentioned which can be seen as unlimited from the practical point of view.

a) Wire based

The simplest possible horizontal slot waveguide is a type consisting of two wires as shown in Fig. 2.12 II. a). For a high width of the waveguide, modal behavior becomes an issue for this type of slot waveguide. For most applications single mode waveguides are demanded, but for large width of the slot waveguide this can not be ensured.

b) Symmetric horizontal slot waveguide based on ribs

For the rib type slot waveguides, the advantages and disadvantages of the horizontal approach depicted above are still valid. Furthermore, the two slab waveguides outside of the rib region enable firstly a good electrical wiring of the structure, which is advantageous for application such as amplifiers, modulators or laser and secondly the realization of a suspended slot waveguides. This could also enable the realization of new types of sensors. However, a structure as shown in Fig. 2.12 II. b) is a very challenging task in realization. Nevertheless, due to the high degree of symmetry this structure is considered in this work for the sake of comparison with other slot structures, and to demonstrate the origin of some important characteristics of slot waveguides.

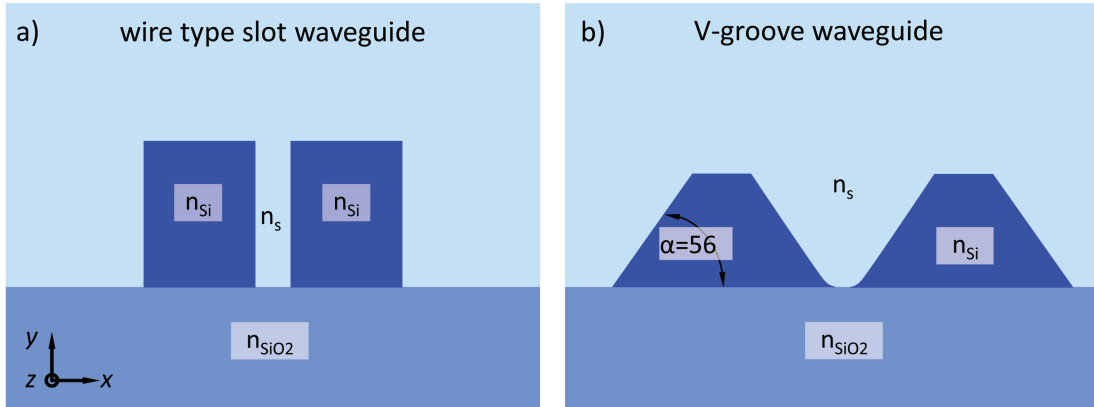
c) Asymmetric horizontal slot waveguide based on rib/slab

Much more appealing from the practical point of view compared to Fig. 2.12 II. b) is a structure consisting of a slab and a rib waveguide on top (see Fig. 2.12 II. c)) studied for the first time intensively in [36]. This would combine all advantages of the horizontal rib- and wire type structures at a minimum of effort in terms of realization. From the practical point of view, this structure is very interesting, because it enables electric wiring. Besides this structure only the slot waveguide type of Fig. 2.12 II. c) can offer this feature, but with the handicap of an increased fabrication effort. Furthermore, with the very shallow etch depth typically used for rib waveguides this type has the lowest etched surface resulting in a minimum of scattering losses.

d) Asymmetric horizontal slot waveguide based on wire/slab.

A special case of Fig. 2.12 II. c) is illustrated in Fig. 2.12 II. d), where the rib on top gives way to a wire. This structure has an increased lateral confinement compared to Fig. 2.12 II. c) This would combine all advantages of the horizontal rib- and wire type structures at a minimum of effort in terms of realization. Beyond that, due to the slab waveguide as basis, this configuration would be interesting for active devices based on Fig. 2.12 II. c) in sections where no electric wiring is necessary due to the higher lateral confinement.

I. Vertical slot waveguides



II. Horizontal slot waveguides

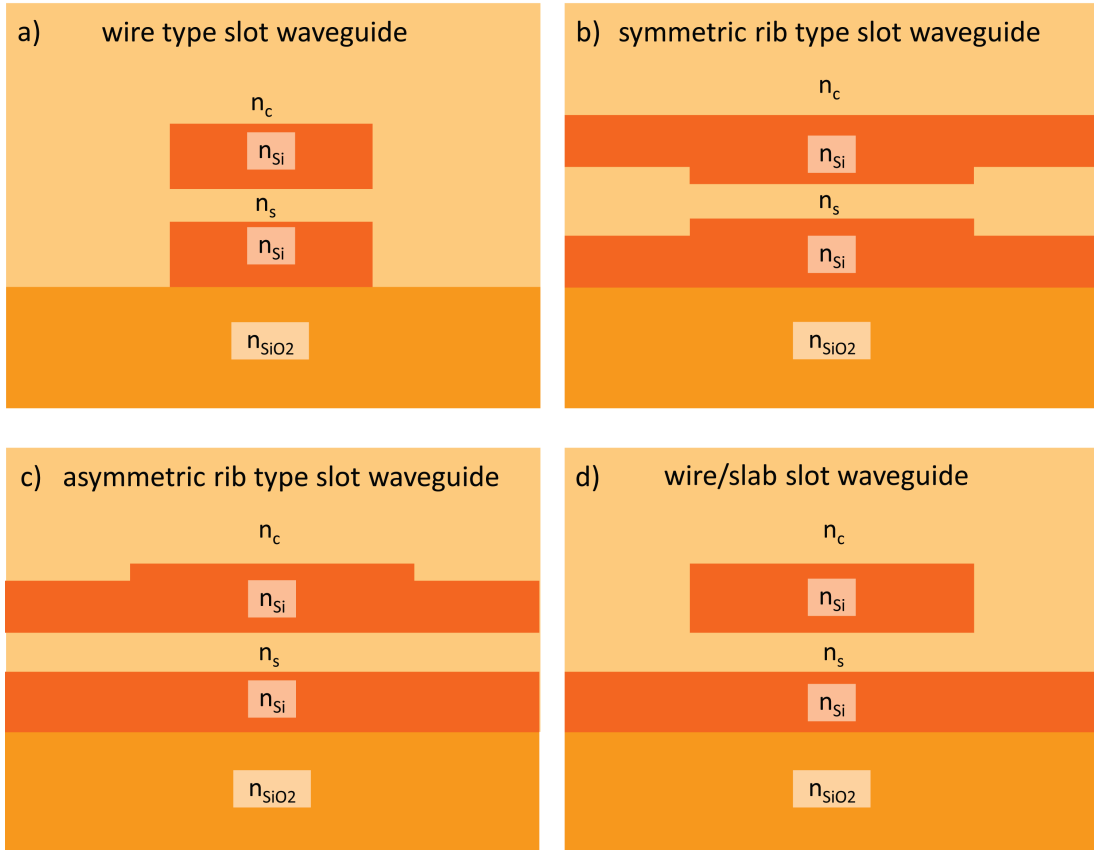


Figure 2.12.: Types of slot waveguides investigated in context of this thesis. The illustrations schematically show the cross section of the waveguides with z being the propagation direction of the light.

2.4. Conclusion

From equation 2.9 and its approximation 2.10 all major characteristics of the slot waveguide effective index were deduced in the two dimensional case. It was shown that the slot has a major impact on the effective index and that this influence is at maximum for a certain waveguide height compared to a three layer waveguide of the same overall thickness. In the vicinity of this maximum the confined optical power in the slot is at maximum as well. According equations for the fields and power distribution were derived and the dependence on the relevant waveguide parameters e.g. refractive indices, waveguide height and slot thickness were studied. Optimized structures with respect to the height were analyzed and it was illustrated, that the light intensity for a high refractive index difference slot waveguide outbalances all other waveguiding structures used so far. Next, by approximating the light power in the slot region with a Taylor series, it was possible to fathom the origins of this so-called 'slot effect'. Finally, the different types of slot waveguides which will be discussed in this thesis were introduced. Their advantages and disadvantages in terms of practical realization were addressed.

3. Simulation methods

Throughout the entire work for this thesis, two simulation methods have been used. Both methods solve the time independent Eigenmode equation resulting from assuming a plane wave propagation where homogeneous materials in z -direction have to be assumed.

3.1. The Finite Element Method

For the calculation with the Finite Element Method (FEM) [100] the commercially available Multiphysics package from Comsol was used [101] with the electromagnetic module. The latter is capable to calculate hybrid mode waves, e.g. modes which feature all six field components for the E- and H-field. Therefore, three dimensional waveguiding structures with sizes below the wavelength and ultra high index contrast are treated correctly. This makes the calculation of the so-called minor field besides the strong major field components of the orthogonal polarization necessary. Those minor fields must not be neglected in order to observe physical effects originating from the minor field such as lateral leakage (see chapter 6).

This results in a change of the nomenclature compared to the 2D case discussed in the previous sections. In dependence on the dominant field components we denote the modes accordingly as quasi-TE modes with a major field containing the transversal field components (E_x and H_y), the quasi-TM modes consist of the transversal field components (E_y and H_x). Comsol's FEM solver allows anisotropic materials of the form:

$$\epsilon_{rc} = \begin{bmatrix} \epsilon_{xx} & \epsilon_{xy} & 0 \\ \epsilon_{yx} & \epsilon_{yy} & 0 \\ 0 & 0 & \epsilon_{zz} \end{bmatrix} \quad (3.1)$$

$$\mu_r = \begin{bmatrix} \mu_{xx} & \mu_{xy} & 0 \\ \mu_{yx} & \mu_{yy} & 0 \\ 0 & 0 & \mu_{zz} \end{bmatrix}, \quad (3.2)$$

enabling the implementation of perfectly matched layers as boundary condition. In order to obtain a more compact formulation, the zz -element can be separated from 3.1 and 3.2. The transverse part reduces then to:

$$\epsilon_t = \begin{bmatrix} \epsilon_{xx} & \epsilon_{xy} \\ \epsilon_{yx} & \epsilon_{yy} \end{bmatrix} \quad (3.3)$$

$$\mu_t = \begin{bmatrix} \mu_{xx} & \mu_{xy} \\ \mu_{yx} & \mu_{yy} \end{bmatrix}. \quad (3.4)$$

With the equation:

$$\vec{\nabla} \times (\epsilon_{rc}^{-1} \times \vec{H}) - k_0^2 \mu_r \vec{H} = \vec{0}, \quad (3.5)$$

by assuming a plane wave propagation in z -direction with $\vec{H}(x, y, z) = H(\vec{x}, y) e^{-i\beta z}$ and $\vec{\nabla} \cdot \vec{B} = 0$, an eigenmode equation is obtained:

$$\vec{\nabla}_t \times (\epsilon_{zz}^{-1} \vec{\nabla}_t \times \vec{H}_t) - \tilde{\epsilon}_t \vec{\nabla}_t (\mu_{zz}^{-1} \vec{\nabla}_t \cdot \mu_t \vec{H}_t) - (k_0^2 \mu_t - \beta^2 \tilde{\epsilon}_t) \vec{H}_t = \vec{0}, \quad (3.6)$$

where the subscript t denotes the x and y component of $\vec{\nabla}_t = \vec{e}_x \frac{\partial}{\partial x} + \vec{e}_y \frac{\partial}{\partial y}$ of the field. Moreover,

$$\tilde{\epsilon}_t = \frac{\epsilon_t^T}{\det(\epsilon_t)} \quad (3.7)$$

has to be defined. The equation for the electric field can be obtained by simple replacement of \vec{H} by \vec{E} an interchanging ϵ with μ . If not mentioned otherwise, the equation for the electric field has been solved. For the generation of the mesh linear vectorial Nedelec elements are provided by the software [102]. the field is defined on the three edges of triangular elements. The vectorial elements fulfill the divergence condition $\vec{\nabla} \cdot \vec{H} = 0$ and $\vec{\nabla} \cdot \vec{E} = 0$ avoiding both - spurious modes and problems with dielectric corners [100].

Apart from perfectly matched layers, conductive boundary conditions $\vec{n} \times \vec{E} = 0$ (perfect electric conductor - PEC) or $\vec{n} \times \vec{H} = 0$ (perfect magnetic conductor - PEM) were used for simulations where no radiation was expected. Here, \vec{n} is a normalized vector perpendicular to the boundary. These boundary conditions ensure that the tangential field components vanish at the boundary of the simulation domain. The used boundary condition was chosen in dependence on the polarization of the desired eigenmode. By setting the minor components of the field to zero on the simulation domain edges, the influence of the boundary condition on the simulation results is minimized.

In addition, these boundary conditions are used to save computational time. All simulated waveguide geometries of this thesis feature a symmetry plane parallel to the $x - z$ or $y - z$ direction. By applying the boundary condition, where the minor components have to vanish at the symmetry-plane, of a mirror symmetric waveguiding structure (with respect to the symmetry plane) the slot mode can be calculated correctly.

The accuracy of the simulation results is controlled by the amount of elements in the simulation domain. The size of the elements is adjusted to the size of the geometry and to the intensity of the field for a specific waveguiding structure. For the simulation of the slot waveguide this results in a very fine mesh in the slot region with element sizes of a few nanometers, whereas the element size outside of the waveguide increases with the decreasing evanescent field to about 10 – 100 nm. Moreover, adaptive mesh refinement was used to further increase the accuracy for some purposes, in particular for the V-groove waveguide, where the region of interest is bordered by an acute-angled corner [100]. This, and other application specific details of the simulations are described in the particular chapter.

In order to perform parameter scans the Matlab [103] interface of Comsol's Multiphysics was used. The implemented programming language enabled to start and stop simulations with different geometry parameters and to read out the results. In addition, at a later stage programs were written allowing for automatic structural optimization of waveguide geometries with respect to a specific physical effect. Therefore, based on the results of a simulation the parameters for the next simulation were determined. This procedure allowed for an automatic iterative optimization at a minimum of computational effort.

As an example, Fig 3.1 shows a typical simulation of a horizontal slot waveguide. The left side shows the adaptively refined, superfine mesh, whereas the right part depicts the calculated optical power profile. The waveguide domain is entirely surrounded by a PML layer (see section 3.5).

3.2. The Variational Mode Matching method of MaxWave

The Variational Mode-Matching (VMM) method used in the computation of the optical modes in the waveguide cross-section belongs to the family of full-vectorial film mode-matching methods [104–108] where the optical field is expanded in terms of local TE- and TM-polarized film modes. One of the most critical steps in mode-matching techniques is the determination of a proper set of

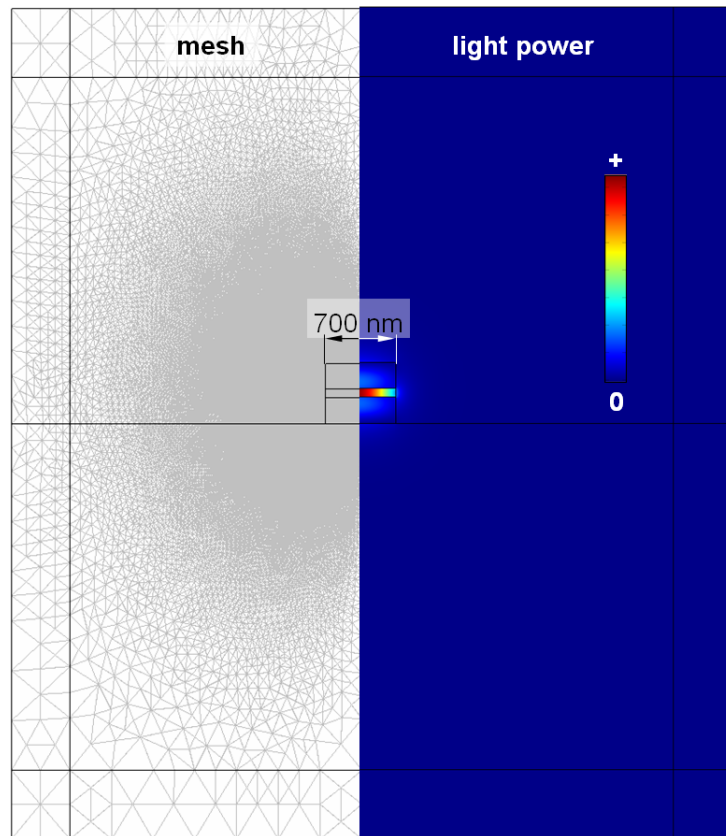


Figure 3.1.: Left: The adaptively refined mesh of a typical FEM simulation. Right: Light power as a result of the calculation. The entire waveguide domain is surrounded by a PML.

local eigenmodes since an improper truncation of the spectrum of local waveguide modes causes numerical instabilities. In the VMM method, these difficulties are overcome by employing a Galerkin scheme to the local 1D waveguide problem which reduces the computation of the relevant local waveguide modes to the solution of a well-understood linear eigenvalue problem [100]. As the FE method, the VMM method solves for quasi-TE/TM eigenmodes with all six field components. Perfectly matched layers act in the direction where no leakage was expected — see section 3.5. Figure 3.2 depicts the result of a simulation with MaxWave for a horizontal slot waveguide, consisting of a silicon slab and a silicon wire on top. Details about the method have been provided by the developers [108] and are supplemented in Appendix B.

3.3. Comparison of the two methods

The use of two different methods for the same purpose can be mainly justified by the different boundary conditions which are available. In general, the finite element method (FEM) was used, because of the higher flexibility and the possibility of adaptive mesh refinement, which enables a higher accuracy at the dielectric corners and edges. Moreover there are two advantages, which are less based on the underlying method, then on its realization in the available software. Namely this are the possibility to solve for more than one mode per simulation run - and in addition - without the need of a certain starting value of the effective index near to the value of the desired mode. This is not possible for the Variational Mode-Matching (VMM) tool MaxWave. Here only one mode at a time can be calculated and a starting value for the effective index close to the final result is needed. On the other hand, compared to finite elements, the advantage provided by the VMM method arises

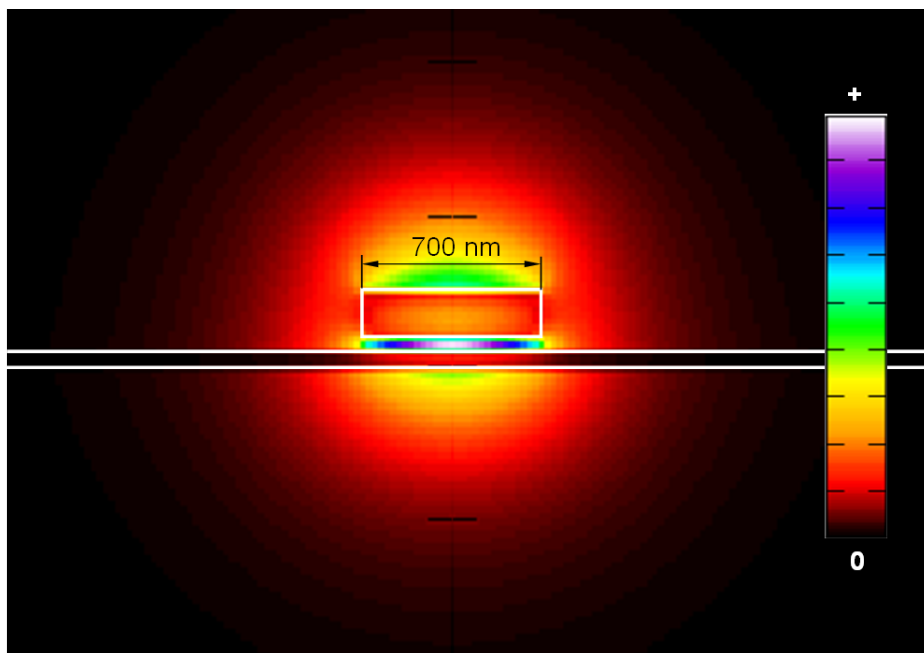


Figure 3.2.: *Light power of a horizontal slot waveguide consisting of a silicon slab below and a silicon wire on top as a result of a simulation using MaxWave.*

from the fact that the simulation of lateral radiating modes can be performed without PML layers acting in the lateral direction. Due to the nature of the modal expansion, the physically correct radiation boundary conditions are inherent to the VMM model. Thus, no effect of an artificial boundary condition has to be considered. This results in a significant reduction of the necessary simulation size.

3.4. General notes on the performed simulations

Simulations carry always the potential risk to deliver unphysical results. Main causes are typically insufficient domain resolution or domain size. In the present work, for all performed simulations convergence studies were carried out. The domain size and the resolution were increased until no significant change of the investigated physical effect was observed. Moreover, to reveal wrong results all simulation procedures were verified with similar work of other groups e.g. with [7, 20, 109]. The comparison of the two different methods delivers an additional validation.

3.5. Perfectly matched layers (PML's)

However, for most simulation methods such as FEM it is necessary to find a possibility to deal with radiation arising from leaky waveguides for two reasons: Firstly, at least to identify leaky modes, at the best to quantify the losses which occur. Secondly, to avoid back reflections from boundaries that can harm the simulation results due to the discretization of the simulation domain. Perfectly matched layers [110] can meet all these requirements to a high degree. In principle, the idea behind perfectly matched layers (PML's) is to transform the boundary condition into a one degree higher problem by introducing layers between the region of interest and the simulation exteriors. This leads to a higher degree of freedom in which the domain closure can act. Nevertheless, to construct a reflection less layer in order to emulate an infinite expanded waveguiding system in a desired direction needs some exploitation of Maxwell's equations. By presuming, that the additional layer match the permittivity and the permeability in such a way that there are no reflections, this leads to an anisotropic material with:

$$\begin{aligned}\mu &= \mu_0 \mu_r L \\ \varepsilon &= \varepsilon_0 \varepsilon_r L,\end{aligned}$$

where ε_r and μ_r are the values of the adjacent physical domain. In Cartesian coordinates L is:

$$L = \begin{bmatrix} L_{xx} & 0 & 0 \\ 0 & L_{yy} & 0 \\ 0 & 0 & L_{zz} \end{bmatrix} \quad (3.8)$$

The matrix elements are connected by:

$$L_{xx} = \frac{s_y s_z}{s_x}, \quad L_{yy} = \frac{s_z s_x}{s_y}, \quad L_{zz} = \frac{s_x s_y}{s_z}, \quad (3.9)$$

For an PML acting in x -direction, $s_{x,y,z}$ are:

$$\begin{aligned} s_x &= a - ib \\ s_y &= 1 \\ s_z &= 1. \end{aligned} \quad (3.10)$$

Here, a and b are arbitrary real constants determining the attenuation of the fields in the PML [111]. Obviously, if an PML layer should act in any other direction or in corners even in two directions, the according $s_{coordinate}$ has to be replaced by the first equation of (3.10). The imaginary part in (3.10) changes every oscillating solution in the PML region into an exponentially decaying one. Therefore, the attenuation of a propagating wave over a distance Δx is given by the x component of the wave vector k_x , and the imaginary part of s_x :

$$|\vec{E}| = |\vec{E}_0| e^{-bk_x \Delta x} \quad (3.11)$$

Hence, a PML can be simply seen as an artificial absorbing material layer which is optimized for high absorption with no reflections regardless of the incident angle or wavelength. It should be noted, that this is only true for the solution of the exact wave equation. Any discretization lifts the analytically perfect PML characteristics and some minor reflections occur. However, by approximating the wave equation closely with a very fine resolution, the reflections are still negligible for incident angles close to 90° between PML surface and the incident k vector. Acute, or in the worst case, glancing angles have to be avoided, which is no problem for the discussed waveguiding systems. For the implementation of the PML's the above formulation can be directly used, due to the fact, that Comsol Multiphysics supports anisotropic media as described in 3.1. To ensure sufficient accuracy, a thickness of approximately λ was implemented and at least $10 \cdot \lambda$ resolve the PML.

4. Modal behavior

In this chapter, the modal characteristic of the photonic slot waveguide will be discussed and differences to standard waveguide structures such as ribs and wires will be pointed out. At first, the slab waveguide system will again be used. Later, for the investigation of the full modal spectrum of the three dimensional slot waveguide structure FEM simulations will be carried out. A single mode criterion for a typical slot waveguide structure will be one major result.

Modal behavior is a crucial characteristic of any dielectric waveguiding structure. Assuming standard methods for the coupling of the light into the integrated waveguide such as endface coupling with the use of fibers all supported modes of the slot waveguide are typically excited. For most applications this is undesirable because each mode has a different field profile and therefore different propagation constant. There is only one possibility to avoid this problem — by simply use only single mode structures, thus waveguides supporting only one first order mode for each polarization. All other modes are below the cutoff and experience high radiation losses.

For standard waveguiding structures such as wires, ribs and channels the restriction to one first order mode is not necessary because these structures are designed in order to support only one so-called *fundamental* mode per polarization. But because of the specific structure of slot waveguide the mode classification of conventional waveguides cannot be directly applied.

In chapter 2.2.1 the studies were restricted to the even mode, which was identified as the so-called slot mode. The slot waveguide structure represents a highly coupled system where coupling theory demands the existence of an odd mode in principle [88]. Nevertheless, the slot waveguide structure differs to standard coupling problems. The even and odd modes become time independent true eigenmodes of the system.

4.1. Effective index of the first order odd mode in the 2D case

For the calculation of the effective index of the odd mode it is sufficient to change the symmetry condition. By assuming that the field is now odd ($E_y(-y) = -E_y(y)$), in 2.6 this leads to $b_1 = 0$ instead of $a_1 = 0$. By repeating the procedure described in 2.2.1 the effective index equation of the odd mode is obtained:

$$-\coth\left(\frac{s\gamma_s}{2}\right) = \frac{\kappa n_s^2 (\kappa \sin(h\kappa) n_c^2 + \cos(h\kappa) n_g^2 \gamma_c)}{n_g^2 (\sin(h\kappa) n_g^2 \gamma_c - \kappa \cos(h\kappa) n_c^2) \gamma_s}, \quad (4.1)$$

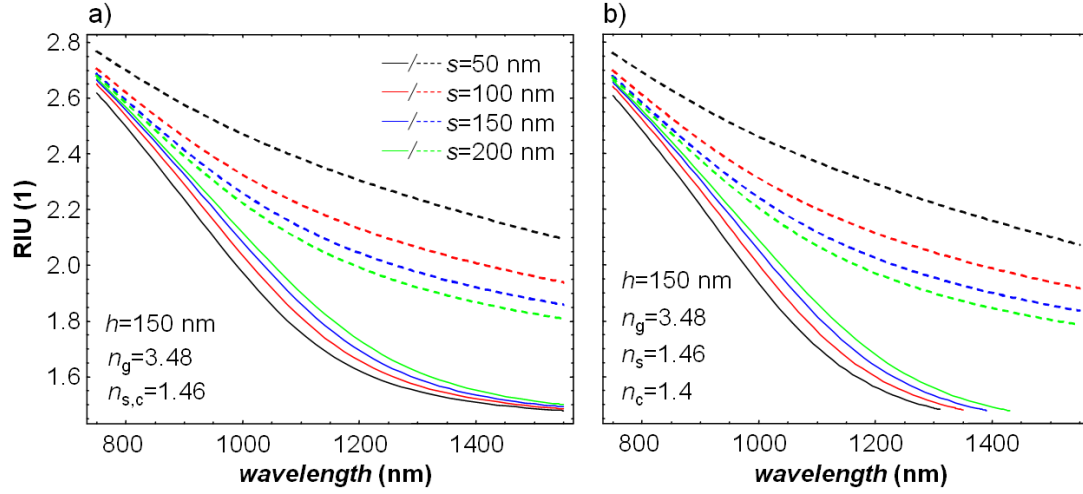


Figure 4.1.: a) Effective index comparison of the even mode (dashed lines) and the odd mode (solid lines) in a 2D slot waveguide with height $h = 150$ nm for a) indices $n_g = 3.48$, $n_{s,c} = 1.46$ and b) $n_s = 1.46$ and $n_c = 1.4$ in dependence on the wavelength.

Figure 4.1 a) shows a comparison between the even and odd slot waveguide mode for a fixed waveguide height of $h = 150$ nm in the vicinity of the optimized waveguide geometry found in 2.2.2. In addition constant refractive indices of $n_{s,c} = 1.46$, and $n_g = 3.48$ were assumed according to standard SOI parameters for silicon and silica [112] at a wavelength in the near infrared of $\lambda = 1550$ nm. The plot shows the effective indices of the even and odd mode using the equations (2.9) (dashed lines) and (4.1) (solid lines) respectively, in dependence on the wavelength λ for different slot thicknesses s .

This dispersion characteristic reveals that the effective index of the odd mode is always below the effective index of the even one. Interestingly, the dependence on the slot thickness is inverted for the odd mode compared to the even mode. With decreasing slot thickness, the effective index decreases as well. An explanation of this behavior is given in the next section, where the field and the Poynting vector are discussed in more detail. Moreover, the odd mode converges to the effective index of the surrounding medium which is equal to the effective index of the slot. This is a typical behavior of symmetric systems. As Fig. 4.1 b) shows a cutoff exist for a refractive index $n_s > n_c$. Therefore, in this region the lossless waveguiding condition is not fulfilled anymore for the odd mode, and the field radiates away from the two cores. This means, it is possible to operate the slot waveguide in the desired single mode regime, where no additional mode propagates over a noteworthy waveguide length.

4.2. Mode characteristic of 3D slot waveguides

4.2.1. Fundamental characteristics

The mode spectrum of the slot waveguide structures becomes even more complicated due to the fact that the symmetry condition must hold true for higher modes as well. At this point it is important

to note that all further studies are restricted to modes where the electric field shows more than one maximum in the waveguide with respect to the coordinate parallel to the slot. For the horizontal slot waveguide this is the x -direction. Higher order modes perpendicular to this direction are left unconsidered. This can be justified by again assuming that the region of interest with respect to the waveguide height h is in the vicinity of the optimized geometry found in section 2.2.2. Then, in the two dimensional case the height is much too small to support more than the first order mode. This also holds true for the three dimensional case.

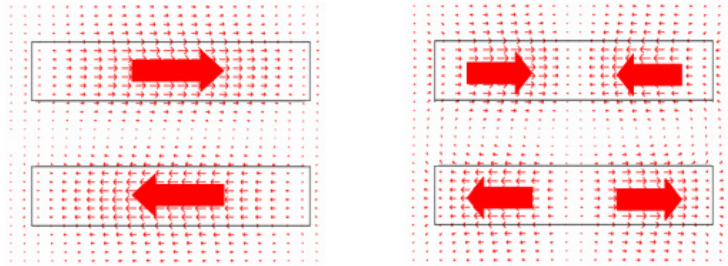
In order to study the higher order modes with respect to the coordinate parallel to the slot *i.e.* in lateral direction (assuming the horizontal slot waveguide concept), three dimensionality of the structure has to be assumed. This problem cannot be solved analytically and requires a numerical method. In this case, Comsol's FEM based 2D eigenmode solver was employed.

As published in [52] Fig. 4.2 shows the transverse electric field of all first and one order higher modes for both polarizations. To obtain well confined modes, waveguide parameters of $h = 165$ nm, $w = 1400$ nm and $s = 200$ nm were assumed. Moreover, refractive indices of $n_g = 3.48$ for the waveguide and $n_{s,c} = 1.46$ for the slot- and surrounding region of were chosen. The electric field of the fundamental even quasi-TM mode, which is the mode of interest, is strongly confined in the slot region. Strong confinement of the electric field in the slot also occurs for all higher even quasi-TM modes, while the electric field of the odd quasi-TM modes has to be zero in the center of the slot due to symmetry purposes. Even and odd modes occur as well for quasi-TE polarization. For these modes the electric field remains concentrated in the two silicon wires which is in consistency with standard waveguiding structures.

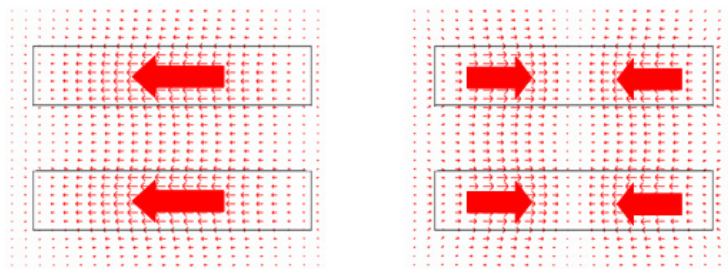
The difference between the even and odd mode for the polarization corresponding to the slot mode is more emphasized in Fig. 4.3. In contrast to the even slot mode, where the light power is concentrated in the slot region, for the odd mode the light power of the odd quasi-TM modes is pushed into the outer low index regions.

Fundamental modes 1st higher modes

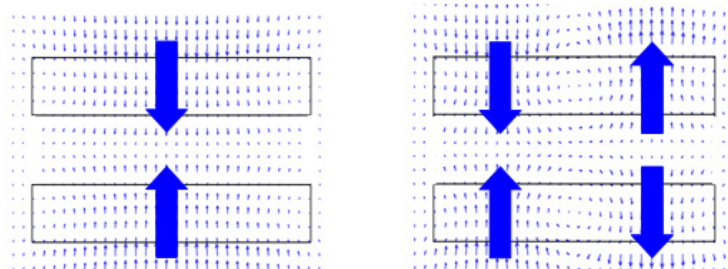
Quasi-TE antisymm.



Quasi-TE symmetric



Quasi-TM antisymm.



Quasi-TM symmetric

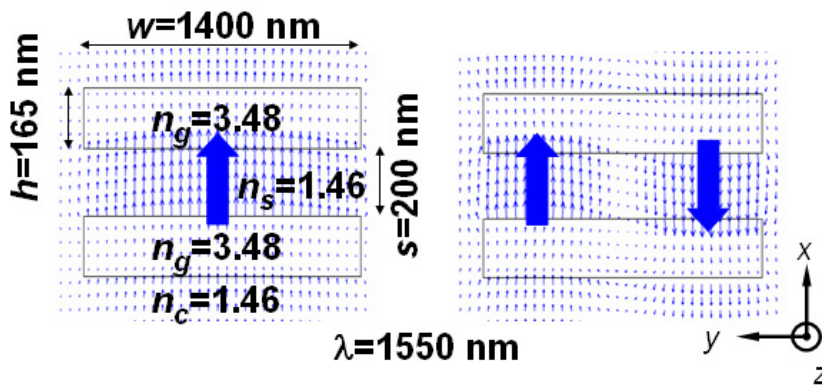
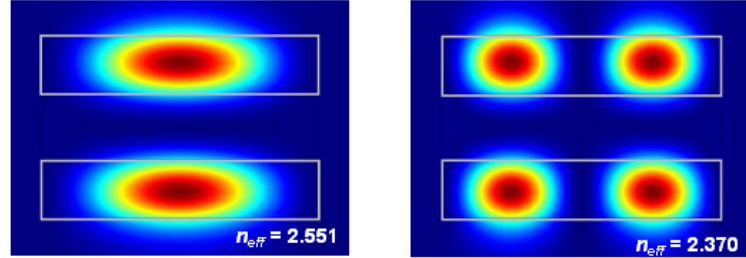


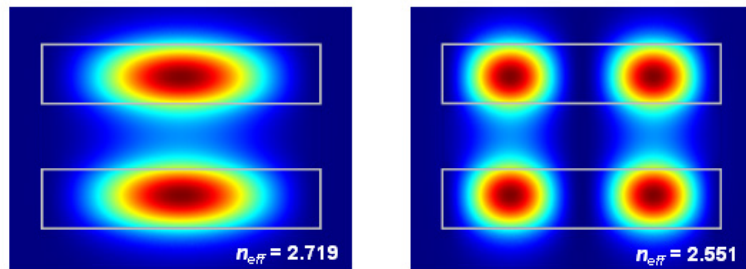
Figure 4.2.: Transverse electric field of all first and second order modes for both polarizations for a wavelength of $\lambda = 1550$ nm calculated by FEM simulations; waveguide parameters $h = 165$ nm, $w = 1400$ nm, $s = 200$ nm indices of $n_g = 3.48$, $n_{s,c} = 1.46$.

Fundamental modes 1st higher modes

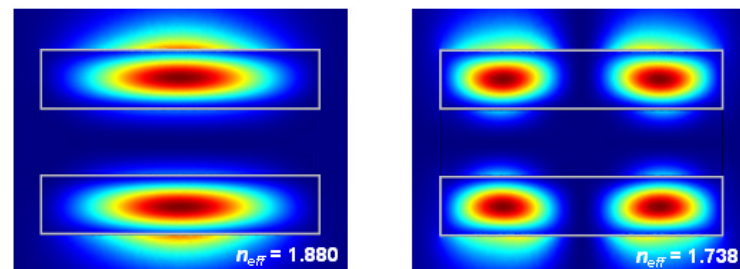
Quasi-TE antisymm.



Quasi-TE symmetric



Quasi-TM antisymm.



Quasi-TM symmetric

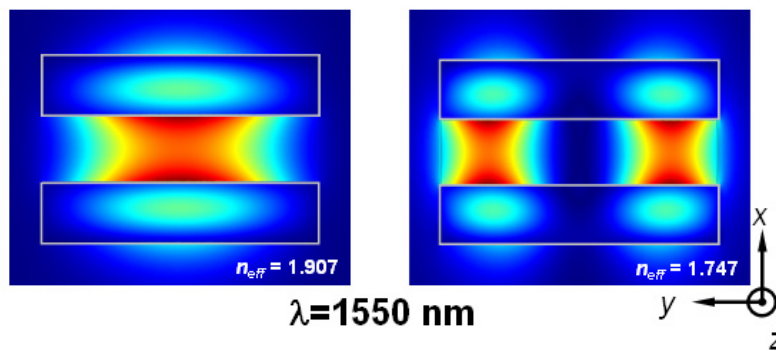


Figure 4.3.: Poynting vector component S_z in propagation direction for the same structure as in Fig. 4.2.

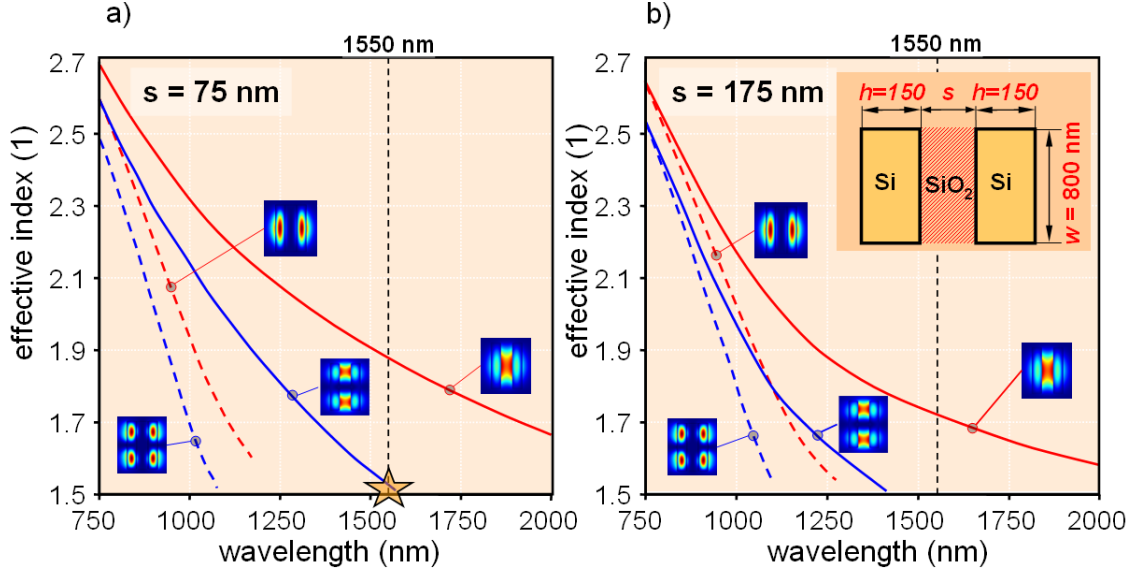


Figure 4.4.: Dispersion characteristic of first and second order quasi-TM even (solid) and odd (dashed) modes for a three dimensional slot waveguide with $h = 150$ nm, $w = 800$ nm, $n_g = 3.48$, $n_{s,c} = 1.46$. The slot thickness was fixed to a) $s = 75$ nm and b) 175 nm. The red lines correspond to first order, blue lines to second order modes.)

In order to discuss the modal characteristics in more detail for the three dimensional case, FEM simulations were carried out for different wavelengths in the interesting range. Figure 4.4 shows the resulting dispersion characteristics for two different slot thicknesses of $s = 75$ nm and $s = 175$ nm at a fixed waveguide height of $h = 150$ nm and a width of $w = 800$ nm. Although silicon is highly absorptive below a wavelength of about $1 \mu\text{m}$ this wavelength region was included to demonstrate the principle modal behavior. The dispersion characteristics are directly related to the electric field distributions. The effective index of the odd modes is always lower than that of the even modes of the same order because the electric field of the odd modes is strongly pushed into the outer low index region. In contrast, the electric field of the even modes is pushed into the low index slot region, which covers only a limited area. The larger the slot width the faster the even and odd modes approach each other (and gradually merge) at short wavelengths due to the decreasing coupling strength between the two wires. It is also possible that an even higher order mode has a larger effective index than the odd fundamental mode (see Fig. 4 for $s = 75$ nm). For modes with effective indices close to the refractive index of $n_{s,c} = 1.46$ no confined mode was found. This indicates, that in the three dimensional case an even slot waveguide with $n_s = n_c$ has a cutoff, where this particular mode radiates.

With increasing s the cut-off wavelength of the fundamental odd quasi-TM mode shifts to larger values as already observed in the two dimensional case, whereas the cut-off wavelength of the first higher even quasi-TM mode shifts to lower values. Within a certain interval of the slot thickness s only the fundamental even quasi-TM mode exists at the wavelength of 1550 nm and thus single-mode behavior is obtained.

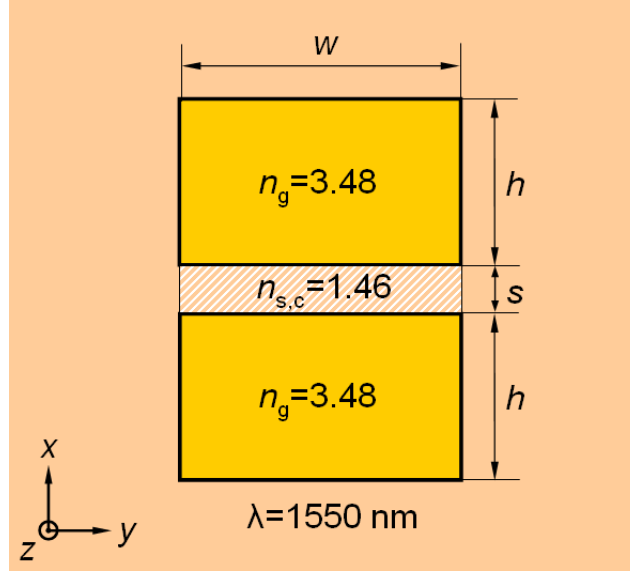


Figure 4.5.: Horizontal slot structure used as model for the calculation of the second order odd modes.

4.2.2. Second order mode characteristic

With respect to single mode operation, the odd mode represents no problem in the vicinity of 1550 nm wavelength (emphasized by a black line in Fig. 4.4) for the interesting slot thickness $s < h$.

Nevertheless, there is a mode which restricts geometry parameters of slot waveguides that can be used - the second order even mode. The star in Fig. 4.4 indicates that for a slot thickness of $s = 75$ nm the second order even mode is still guided and the slot waveguide structure is multimode for the wavelength of interest.

In the first studies on the slot waveguide structure [5, 7, 12, 57], the modal behavior in particular the issue of higher order modes, had not been addressed because in the vertical concept the waveguide width to height ratio is restricted to low values of the order of 400 nm due to the processability. The width w and height h of the slot waveguide structure are defined as depicted in the inset of Fig. 4.4.

But for the horizontal concept (see Fig. 4.5), the restriction to low width-to-height ratios is alleviated and the second order even mode becomes an issue as described in [50, 113]. In order to study the characteristic of the second order mode, we employed FEMLAB (see section 3.1) for the 2D eigenmode analysis at a wavelength of 1550 nm. Triangular vector-elements were used. In order to determine the adequate mesh density required to achieve a sufficient precision, we first compared the calculated effective index of a one dimensional slot waveguide with the analytic solution given in [7]. The mesh density was chosen such that the deviation between FEM results and analytic results was on the order of 10^{-4} . Next, the mesh was refined for the two dimensional slot waveguide structure as depicted in the inset of Fig. 4.4 such that a comparable accuracy for the effective index was obtained. The simulation domain was set to $4 \mu\text{m} \times 4 \mu\text{m}$. Changing the boundary condition from a perfect electric conductor to a perfect magnetic conductor had negligible influence on the simulation results, thus indicating that the evanescent field has sufficiently decayed at the border of

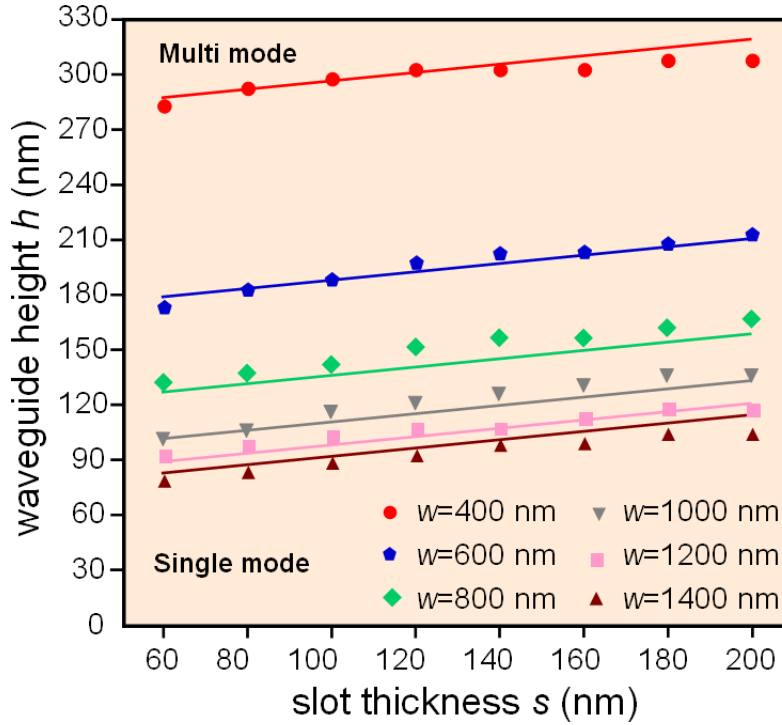


Figure 4.6.: Single mode criteria for a slot waveguide structure as sketched in Fig. 4.5 for different waveguide width w in dependence on the slot thickness s ($\lambda=1550$ nm). The lines are based on the analytic approximation of equation (4.2) with the intercept according to equation (4.3).

the simulation domain. For all simulations no adaptive mesh refinement was used.

With the use of this simulation model as shown in Fig. 4.5, the modal behavior of the quasi-TM mode was investigated. An algorithm was developed that identifies slot waveguide geometries with single-mode behavior for the quasi-TM mode. All supported modes solved by the FEM software were automatically investigated with respect to the amount of field maxima in one single silicon core of the slot waveguide structure. If a mode was found with two maxima and an effective index above the cutoff, the structure was identified as multimode. The geometry parameters are restricted to the range where only fundamental- and the even second order modes are supported.

Figure 4.6 shows the results of the simulations for different width w in dependence on the slot thicknesses s at a constant wavelength of $\lambda = 1550$ nm. The points indicate waveguide heights above which the slot waveguide becomes multimode for a given slot thickness. The simulation points therefore can be seen as a single mode criterion. In the area below the simulation points only the fundamental quasi-TM mode exists. Overall a fairly linear dependence of the single mode criterion on the slot thickness s becomes apparent. With decreasing slot thickness, the waveguide height where the slot structure becomes single mode decreases. This is consistent with the fundamental characteristic of the effective index for even slot waveguide modes, which increases with decreasing slot thickness (see Fig. 4.1 for the two dimensional and Fig. 4.4 for the three dimensional case).

The dependence of the single mode criterion on the waveguide width w on the other hand is definitely not linear. For large width w , the single-mode condition of the quasi-TM mode in general

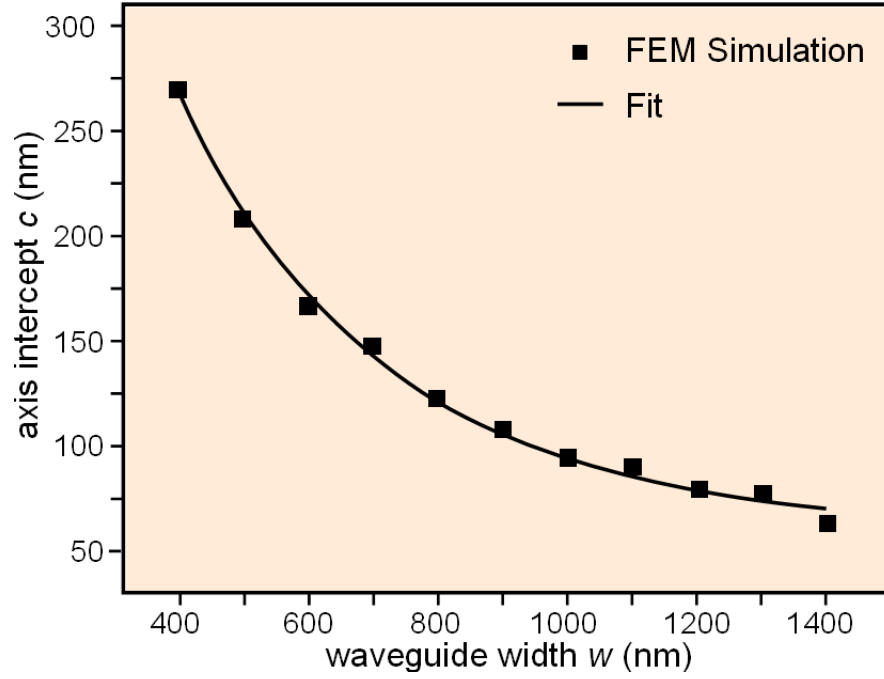


Figure 4.7.: Intercept of the single mode criteria based on the simulation results shown in Fig. 4.6 approximated by the linear equation (4.3).

shifts to smaller values of waveguide heights h . Again, this behavior can be explained by the increased effective index with increasing waveguide width. The shift to smaller waveguide heights is strong for waveguide widths of $w = 400 - 600$ nm but converges for waveguide heights around the wavelength $w = 1400$ nm. This is due to the fast convergence of the effective index to the two dimensional slab system with infinite width. The slope of the nearly linear relationship between slot thickness s and waveguide height h is independent of the waveguide width w . This enables an simple approximate expression of the single-mode conditions for several values of w assuming an linear fit of the form

$$h = 0.23s + c(w), \quad (4.2)$$

where h , s , c and w are given in nanometers. The axis intercept $c(w)$ depends on the width of the of slot waveguide w corresponding to the shift of the single mode criteria in (4.6). The intercept exhibits an exponential decay (see Fig. 4.7). Therefore the width dependent intercept was then fitted by the equation

$$c(w) = 694e^{(-0.003w)} + 60, \quad (4.3)$$

with c and w given in nanometers. The approximation according to the equation (4.2) with the width dependent intercept derived in equation (4.3) is plotted in Fig. 4.6. The lines depict this linear fit of the single-mode condition for the quasi-TM mode. From the practical point of view this fit is absolutely sufficient. The discrepancy between the numerical results and the fit for 600 nm and 1400 nm can be explained by the limit of the simulation accuracy.

5. Power optimization

5.1. Structural optimization

Here, for the slot waveguide structure of the preceding section the geometry parameters are optimized in order to maximize the optical power in the slot region. The results will be discussed with respect to the already obtained single mode criterion and the most important statement of this chapter will be: 'It is possible to increase the power which is confined in the slot region by increasing the width of the waveguide while at the same time maintaining single mode behaviour.'

In the first publications on the slot waveguide structure [5, 7] the high power confinement of the slot waveguide structure was pointed out as one of the major advantages of the slotted structure. However, detailed results were presented only for the two dimensional slot waveguide and the finally fabricated vertical structure. In-depth studies with respect to interdependencies between all geometry parameters including the width w of the waveguide structure, which significantly increases the necessary computational effort had not been performed. Restricting the slot waveguide to the vertical concept this can easily be reasoned.

A high width-to-height ratio cannot be obtained using standard SOI substrates due to the practical limitations in the fabrication. For the horizontal slot waveguide concept (as demonstrated e.g. in [41]), there is no limitation with respect to the width-to-height ratios. The influence of the waveguide width w on the performance of the slot waveguide becomes relevant and has to be studied, which was done for the first time in [50]. From the practical point of view, as already pointed out in section 2.4 it would be advantageous to increase the width to $w > 600$ nm because this would significantly relax the requirements to the necessary lithography process. Structures with such feature size could be realized with deep UV instead of the time consuming and therefore expensive e-beam lithography.

The investigated slot geometry is identical to the structure depicted in Fig. 4.5. In order to investigate the dependence on the relative power in the slot region, FEM simulations for different slot waveguide geometries were performed according to the previous chapter. The power in the slot region is defined as integral of the Poynting vector component S_z in propagation direction divided by the overall power as described for the two dimensional case (see equation (2.16)). The results of the performed simulations for a two dimensional parameter sweep of different heights h and slot thicknesses s for three different widths 400, 600 and 800 nm are shown in Fig. (5.1) a) - c) where the relative power is specified in percent.

In accordance to the two dimensional case, a distinct optimum of the power can be observed with

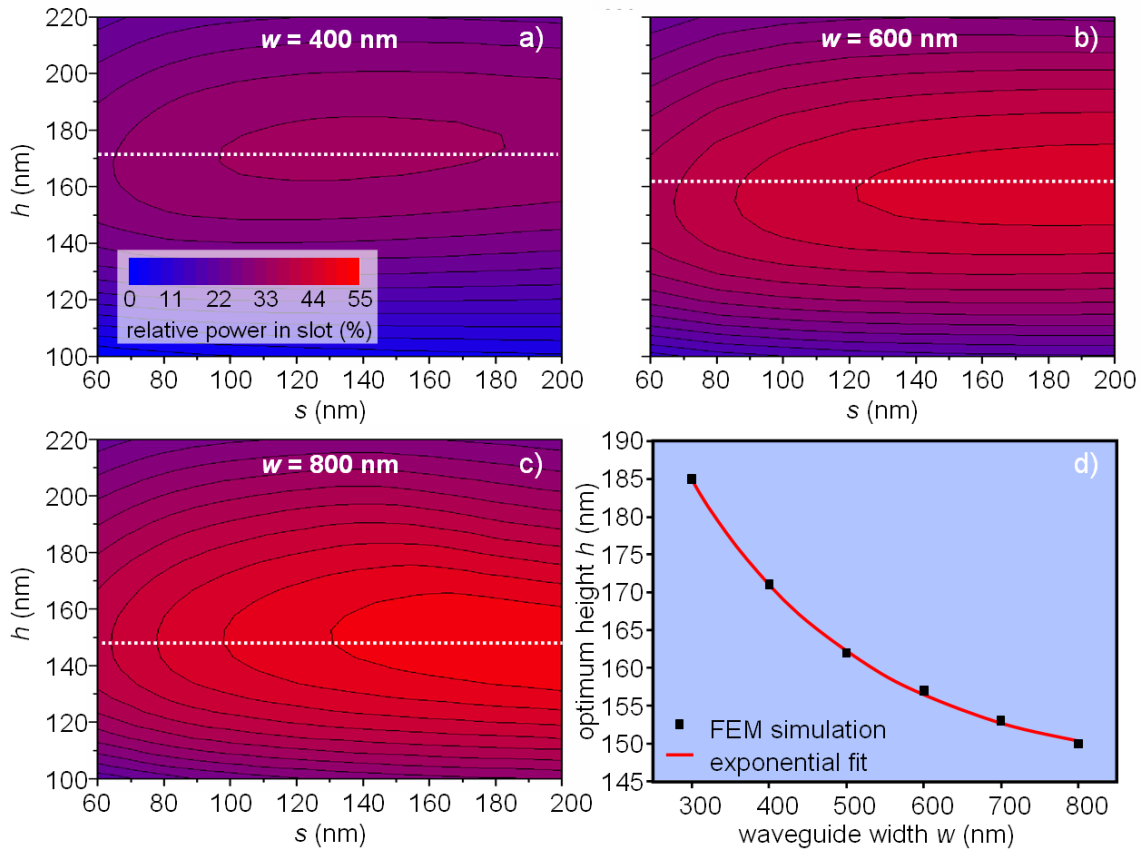


Figure 5.1.: Relative optical power in the slot region for a two dimensional parameter scan of different heights h and different slot thicknesses s . The refractive indices can be extracted from Fig. 4.5. a) shows the light power for a waveguide width of 400 nm b) for 600 nm and c) for 800 nm. In d) the optimum height for six different width (black square) is plotted with an exponential fit (red line) according to the equation (5.1). For all plots the wavelength was fixed to $\lambda = 1550$ nm.

respect to the waveguide height. As the white horizontal dashed lines make apparent, this optimum thickness decreases with increasing waveguide width w . The dependence of the relative slot power on the slot thickness is less pronounced than the dependence on the height. For a waveguide width of 400 nm a power maximum with respect to the slot thickness can be found. Nevertheless, the plot of Fig. (5.1) a) - c) demonstrate, that the dependence on the slot thickness s is weak compared to the dependence on the height h .

The change of the optimum height with respect to the waveguide width w is displayed detailed in Fig. (5.1) d). For each point, a two dimensional parameter sweep as for Fig. (5.1) a)- c) was performed. The optimum height decreases from 185 nm for a waveguide width of 300 nm to about 150 nm for $w = 800$ nm. The optimum height $h = 185$ nm obtained for a width of 300 nm goes conform with the value published in [7]. On the other hand, for the comparably large width of $w = 800$ nm the optimized height of $h = 150$ nm is already very close to the value found in section 2.2.2 for slot waveguide with infinite width w . This further increases the reliability of the simulation results.

By omitting the influence of the slot thickness s the waveguide height h at which the maximum

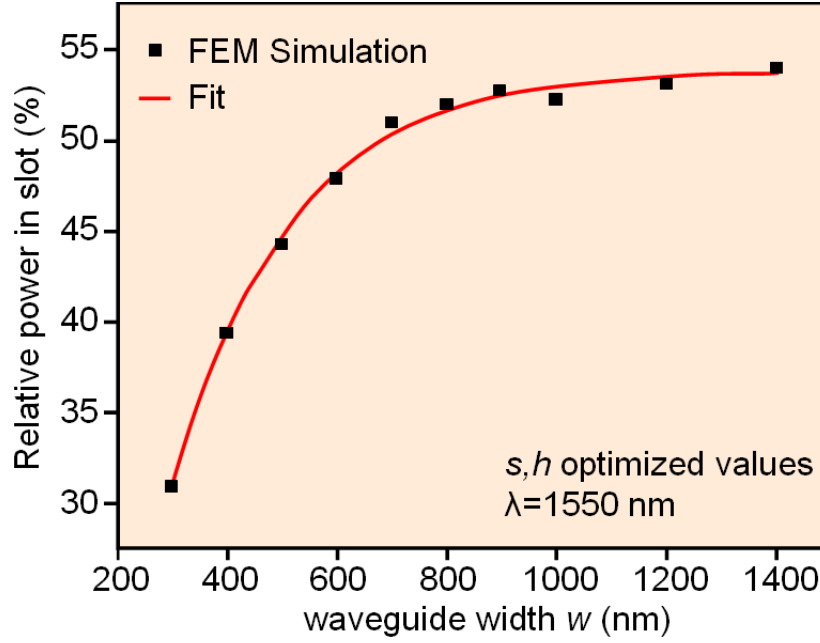


Figure 5.2.: Maximum confined relative optical power in the slot region for a slot waveguide structure with optimized height and optimized slot thickness.

optical power confinement in the slot is achieved for a given width w at a wavelength of 1550 nm can be expressed by the following equation:

$$h = 125e^{(-0.0039w)+144}, \quad (5.1)$$

where h and w are given in nanometers. The result of equation 5.1 is shown as red line in Fig. 5.1.

Finally, by comparing the maxima between all three plots of Fig. (5.1) a)- c) and pointing out that the power scale was fixed for all width, it turns out, that the confined relative light power in the slot region increases with increasing width w . This increase is significant, as shown in Fig. 5.2. For typical vertical slot waveguides with width of $w = 300$ nm such as realized in [5] the relative optical power in the slot is 30%. Again, these findings are in accordance with [7]. For wider slot waveguides the relative optical power increases to more than 50%. At each point in Fig. 5.2 the slot waveguide structure was optimized with respect to the waveguide height h and its slot thickness s . As mentioned before, the influence of the slot thickness on the optical power confined in the slot is much less than the influence of the width. Therefore, almost no change of the light power is observed for slot thicknesses in the range of 100 – 200 nm.

5.2. Optimization with respect to single mode behavior

As the results of the previous section showed, the relative optical power confinement can be enhanced by increasing the width of the waveguide. On the other hand, the geometry parameters for which the slot waveguide structure shows single mode behavior is decreased for increasing width. Therefore, it is essential to study the power optimized slot waveguide structure with respect to the single mode conditions found in section 4.2.

As an example, Figure 5.3 shows the geometry region comprising the power optimized structure together with the single mode criterion for two different waveguide widths of $w = 600$ nm and $w = 800$ nm. In Fig. 5.3 a) the single mode condition is well above the power optimized slot waveguide structure indicated by the white dashed line. Thus, for the power optimized structure with an optimized height h , the slot waveguide exhibits single mode behavior for all slot thicknesses within the calculation region.

However, for increased width such as $w = 800$ nm this does not hold true any more as Fig. 5.3 b) reveals. The single mode criterion is shifted to much lower values of the height h in comparison to the optimized height for maximized power confinement which is only decreased by about 10 nm. This results in a region of slot thicknesses, where the power optimized slot waveguide is in the multimode regime. In the example of Fig. 5.3 b) this can be observed for slot thicknesses below approximately $s = 120$ nm.

In order to enable a more general analysis of this characteristic, the equations defining single mode behavior of slot waveguide structure (4.2) and the equation allowing the identification of power optimized slot waveguides (5.1) can be used. Figure 5.4 plots the results of the two equations for four different slot waveguide width of $w = 600$ 700 800 and 900 nm. Here, it can be seen in further detail that in contrast to the optical power confinement in the slot region, the single-mode condition shows a high interdependence between the slot thickness s and the waveguide height h

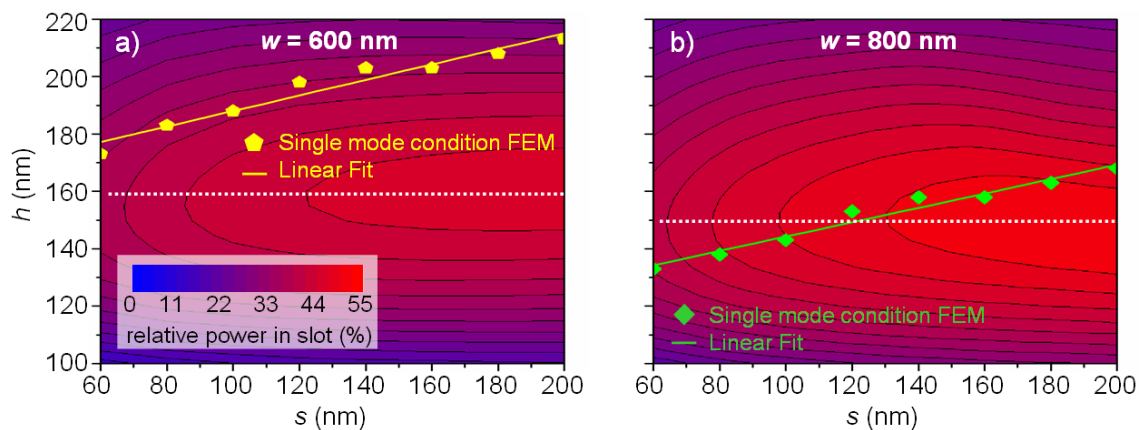


Figure 5.3.: Relative optical power in the slot region as a function of h and s for a waveguide widths of a) 600 nm and b) 800 nm. The refractive indices can be extracted from Fig. 4.5. The yellow and green points are the single mode criteria calculated with FEM. The green and yellow lines are least square fits to the simulation results. The white dashed line indicates the power optimized slot waveguide structure neglecting the influence of the slot thickness s .

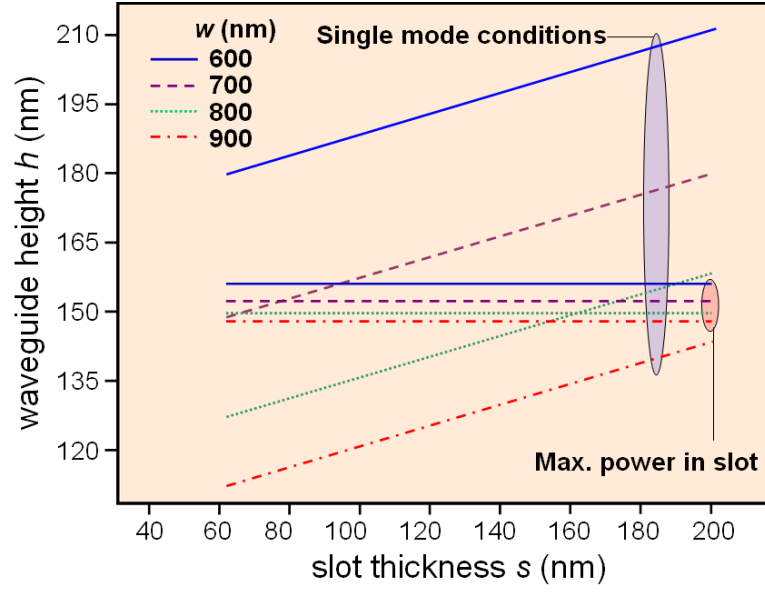


Figure 5.4.: Single mode criterion calculated with equation (4.2) and power optimized slot waveguide structure as a result of (5.1) for four different slot waveguide widths of $w = 600, 700, 800$ and $w = 900$ nm.

compared to the power optimized structure, for which it was even possible to neglect the influence of the slot thickness s . This makes the slot thickness a suitable parameter for design of power optimized slot waveguides. Thus equation (5.1) and (4.2) provide a design rule for SOI slot waveguides with optimized geometries. Let us consider for example a waveguide with a width w of 800 nm. According to Fig. 5.2 this structure confines about 52% optical power in the slot at the optimized waveguide thickness of $h = 150$ nm as can be extracted from Fig. 5.4. Moreover, the slot thickness s is determined with the help of Fig. 5.4 to ensure both maximum optical power confinement in the slot region and single-mode behavior. For the given width of 800 nm, the slot thickness therefore must be larger than approximately 160 nm. It must be noted that the linear fit of Fig. 5.3 b) gives a slightly different result due to the fact that the fit function differs from the numerical results.

6. Leakage behavior of slot waveguides

This chapter is dedicated to two important types of leakage losses. The substrate leakage loss and the lateral leakage loss. While the first mentioned leakage mechanism is widely known, the second type of leakage can hardly be found in any textbook dealing with integrated optics. Therefore, the mechanism is described here in all details and it will be shown, that the modal characteristic of the rib-type slot waveguide causes again a significant difference to conventional rib waveguide structures. The quintessence of the chapter will be: 'Rib-type slot waveguides would be nice because they are easy to fabricate, but care must be taken in designing them — otherwise they might not work!'

Losses are a major issue in silicon photonics. Compared to silica optical fibers where the losses are measured in decibel per kilometer propagation length, the losses of silicon based waveguides are of the range of dB per centimeter, which is five orders of magnitude higher. Typical propagation loss mechanisms are absorption in the waveguide material itself, scattering at the waveguide sidewalls due to surface roughness from etching and other processing steps [92] and bending losses which arise from an abrupt change of the waveguide direction. Summed up, this leads to typical values for the propagation loss of 3 dB/cm [114].

Moreover, the insertion losses for such waveguides are massive compared to other types of waveguides due to the small cross section of the waveguide. One must reckon with approximately 20 dB for coupling light in-, and out of a silicon waveguide structure due to the massive size mismatch

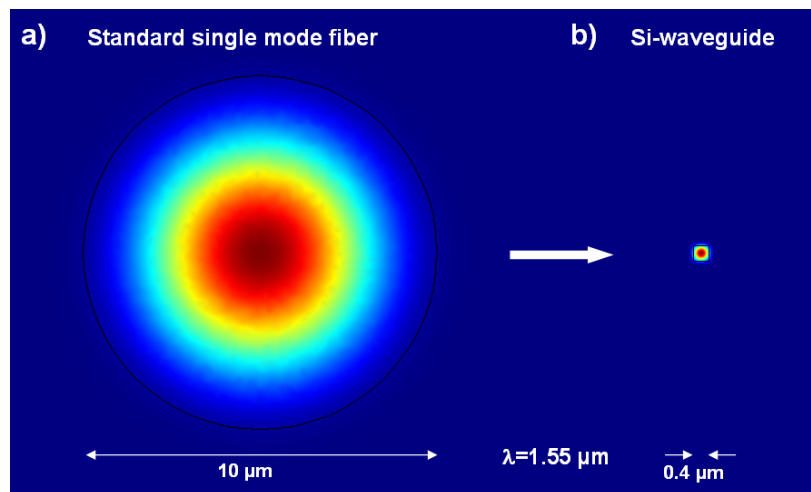


Figure 6.1.: Poynting vector as a result of a FEM simulation for an a) single mode fiber (to the left) and b) a typical silicon waveguide.

between the waveguides and fibers used in the setup environment in order to embed e.g. laser sources and detectors. For example, very often fibers are used for this purpose. Figure 6.1 shows as a comparison the mode profile of a single mode fiber at a wavelength of $\lambda = 1.55 \mu\text{m}$ with the mode profile of a typical silicon waveguide. This comparison illustrates the origin of the high coupling losses. In order to reduce these losses, taper for vertical slot structures and grating structures for horizontal slot waveguides can be used. Nevertheless, the coupling losses remain considerably high. In the following, two loss mechanisms namely the substrate leakage and the lateral leakage are studied for different slot waveguide concepts and strategies will be proposed how these two sources of losses can be avoided.

6.1. Substrate leakage

The substrate of SOI wafers used for silicon waveguides is silicon. The next layer consists of silica, the insulating low refractive index material which is referred as the so-called BOX — buried oxide. The top layer is again silicon, in which the waveguides are realized. However, surrounded by low refractive index materials, the substrate can be seen as waveguiding system itself. Now, if the waveguide is too close to this substrate, coupling can occur resulting in a decrease of the light power in the actual waveguide. This leakage is a critical issue.

In order to suppress this coupling, and to avoid substrate leakage, a sufficiently high isolation of the waveguiding structures from the substrate has to be ensured. Since the optical field distribution

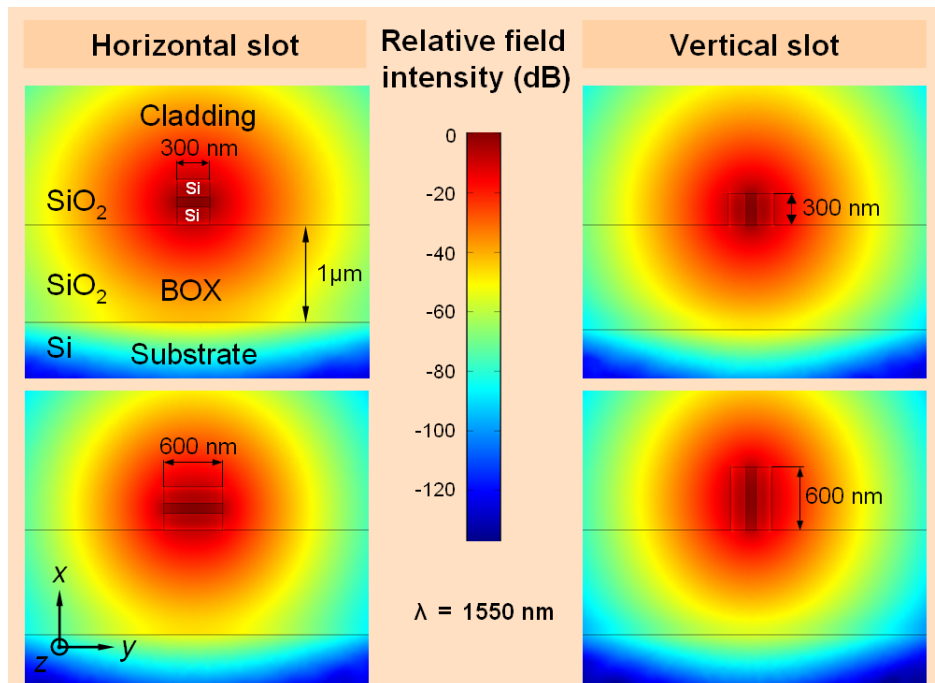


Figure 6.2.: Relative optical power of the vertical and horizontal slot waveguide configuration in decibel for two different waveguide widths of $w = 300 \text{ nm}$ and $w = 600 \text{ nm}$. A BOX thickness of $1 \mu\text{m}$ were assumed and refractive indices of $n_{\text{SiO}_2} = 1.46$ and $n_{\text{Si}} = 3.48$ at a wavelength of $\lambda = 1550 \text{ nm}$.

of slot waveguides deviates from that of conventional SOI waveguides such as wires and ribs a different leakage behavior can be expected [37].

Moreover, the influence of the configuration, *i.e.*, horizontal versus vertical, is a major question. In the following the study is restricted to the wire-type slot waveguides to enable a direct comparison between the configurations. Figure 6.2 provides a qualitative comparison of the two configurations and illustrates the interaction of the waveguide and substrate. It is important to note, that the scale of the relative optical power profile is logarithmic. As a first qualitative result, by comparing the two configurations one finds that for the horizontal slot waveguide the discontinuity of the electric field is apparent at the BOX-substrate interface as well indicating a difference of the two types of slot waveguides. In addition, for the vertical type on the right the field more concentrated in the upper cladding compared to the horizontal concept. The waveguide width has a noticeable influence on the substrate as the relative optical power profiles for the two different widths of $w = 300$ nm and $w = 600$ nm demonstrate. The impact on the substrate leakage is similar for both configurations as Fig. 6.3 shows.

In order to obtain quantitative results, a full-vectorial FEM analysis employing perfectly matched

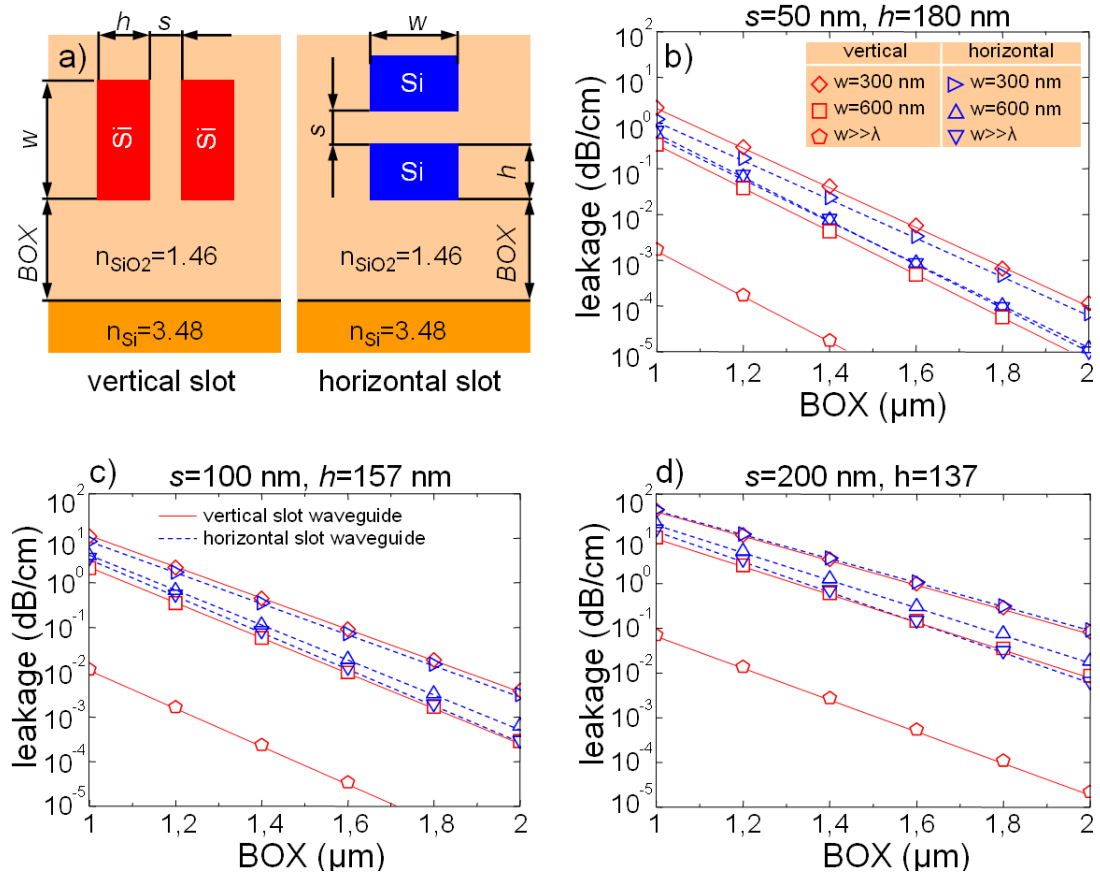


Figure 6.3.: a) Geometry and material parameters for the FEM simulations carried out for b)-c). Substrate leakage in dependence on the BOX thickness for three slot thicknesses b) $s = 0$ nm, c) $s = 50$ nm, and d) $s = 100$ nm, for the three widths $w = 300$ nm, $w = 600$ nm, and $w \gg \lambda$ with the corresponding waveguide thicknesses $h = 180$ nm, $h = 157$ nm and $h = 137$ nm, where the optical power confinement in the slot is at maximum.

layers was carried out. The influence of the parameters w and s on the substrate leakage behavior is studied. The waveguide thicknesses were set to the optimum value for given w at which maximum optical power confinement in the slot is achieved. Both configurations show a strong dependence on the slot thickness. By increasing s from 50 nm to 200 nm the leakage loss shifts by about two orders of magnitude to higher values. An interesting feature is the negligible dependence of this shift on the configuration, as well as on the width w . Comparing the vertical with the horizontal configuration for small widths w no significant difference can be observed. With increasing w the difference between the two configurations becomes increasingly pronounced. For the width $w \gg \lambda$ the leakage loss of the vertical configuration is more than one order of magnitude below the equivalent horizontal structure, but in practice, the realization of vertical slot waveguides is limited to low height-to-width ratios of 2 – 3. Taken together, these results show that a buried oxide thickness of $\text{BOX} > 2 \mu\text{m}$ is necessary to ensure substrate leakage losses $< 0.1 \text{ dB/cm}$ for the horizontal as well as for the vertical configuration.

6.2. Lateral Leakage

6.2.1. Fundamentals

As explained in section 3.1 in contrast to the two dimensional slab waveguides the modes of the three dimensional waveguide structures are not purely TM- or TE- polarized. The boundary conditions can only be fulfilled if minor field components exist in addition to the so-called major field

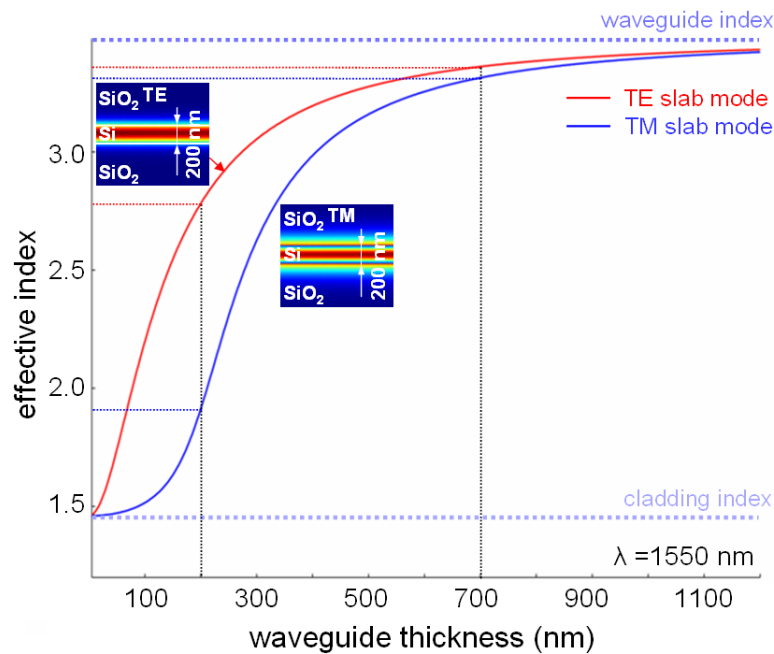


Figure 6.4.: Effective index of the TE- and TM-mode for an SOI slab waveguide in dependence on the waveguide thickness. The insets show the Poynting vector component S_z as a result of FEM simulations for the two polarizations at a fixed waveguide thickness of 200 nm.

components. Moreover, the high discontinuity of the electric field at the waveguide interfaces can lead to a noticeable difference of the effective index between the TE- and TM mode as shown in Fig. 6.4. The insets show the Poynting vector component in propagation direction S_z as a results of FEM simulations for the two polarizations at a fixed waveguide thickness of 200 nm. For this waveguide thickness, the effective index of the TE mode is approximately 0.8 higher than the effective index of the TM mode.

Furthermore, the TE mode of a waveguide with a thickness down to 80 nm is still higher compared to the TM mode of the waveguide with a fixed thickness of 200 nm. Thus, for a rib waveguide structure it is possible, that the effective index of a TM polarized rib mode is below the effective index of a TE polarized slab mode outside of the rib structure. This enables coupling between these two modes via the minor field components of the quasi-TM polarized rib mode, which are identical to the major components of the TE polarized slab mode. These slab modes are not confined in lateral direction and propagate away from the rib waveguide - and leakage occurs. In contrast to the substrate leakage this lateral leakage effect caused by TM-TE coupling is not commonly known. It was demonstrated experimentally for SOI rib-waveguides in [41] for the first time, which based on the numerical work of [115, 116].

For rib-type slot waveguides the coupling mechanism is more complicated, because coupling to two different first order modes — as introduced in chapter 4 can occur: the even mode with the major electric field components in the upper and lower waveguide layer being parallel, and the odd mode with the major electric field components in the upper and lower waveguide layer being anti-parallel. Depending on the geometry parameters and the wavelength only the even mode exists. For the TM polarization the even mode corresponds to the highly confined slot mode. Figure 6.5 a) shows exemplarily the major electric field components and the anti-parallel minor electric field components of the TM-like slot mode (Fig. 6.5 b)). Here depicted for a typical fully symmetric rib-

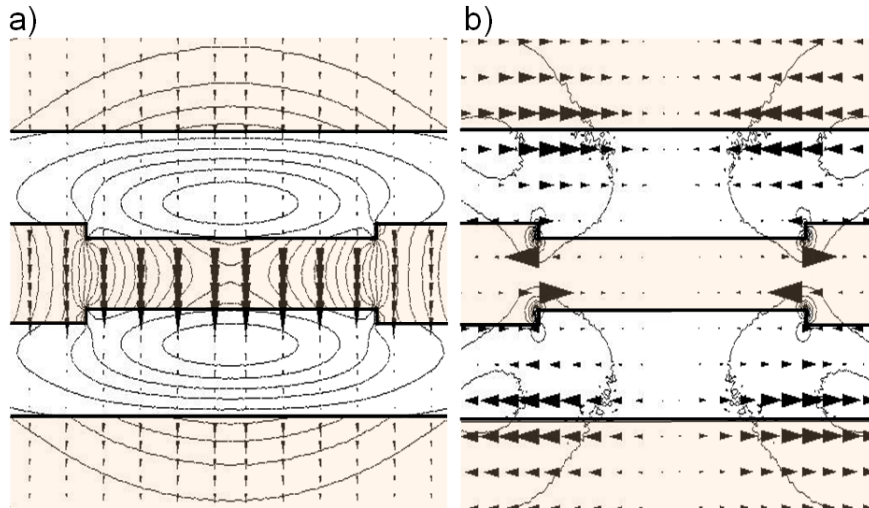


Figure 6.5.: a) Overall optical power (contour) and major electric field (arrows) distribution of the TM-like slot mode of a typical fully symmetric rib-type slot waveguide structure; b) the minor (TE) components are shown with arrows for the electric field and a contour plot for the optical power.

type slot waveguide structure. The role of the two TE-slab modes in the TM-TE leakage mechanism has to be studied against this background [36, 37, 39, 40].

In principle, by comparing the effective indices of the three involved modes, the effective index of the TM polarized slot mode $N_{\text{eff,TM}}$, the effective index of the even TE slab mode $n_{\text{eff,TE,even}}^{(\text{slab})}$ and of the odd TE slab mode $n_{\text{eff,TE,odd}}^{(\text{slab})}$ three different regions must be distinguished:

- I. $n_{\text{eff,TE,even}}^{(\text{slab})} > n_{\text{eff,TE,odd}}^{(\text{slab})} > N_{\text{eff,TM}}$
- II. $n_{\text{eff,TE,even}}^{(\text{slab})} > N_{\text{eff,TM}} > n_{\text{eff,TE,odd}}^{(\text{slab})}$
- III. $N_{\text{eff,TM}} > n_{\text{eff,TE,even}}^{(\text{slab})} > n_{\text{eff,TE,odd}}^{(\text{slab})}$

Figure 6.6 and 6.7 illustrate the physical behavior of waveguides with effective indices in these three regions. For 6.6 and 6.7 the rib height H was fixed to $H = 185$ nm and the slab height h outside of the rib was changed from $0.7H$ to $0.28h$. The effective indices of the quasi-TM polarized slot mode in dependence on the ratio h/H were calculated using FEM whereas the effective indices of the even and odd TE slab modes were determined semi-analytically by solving the transcendent eigenmode equation of a five layer slab system.

As Fig. 6.6 a) shows, for a symmetric slot waveguide with effective indices corresponding to region I, where the effective index of the quasi-TM polarized slot mode is below both TE polarized slab modes outside of the rib, leakage occurs. Light radiates away from the waveguiding core as emphasized with the dotted boxes.

With decreasing h the waveguide system enters the region where the effective index of the quasi-TM polarized slot mode is between the two TE slab modes. Due to the perfect symmetry of the waveguide structure no even minor field exists which could couple the even TE slab mode which has higher effective index than the quasi-TM polarized slot mode. As a consequence, no coupling and therefore no leakage can occur (see Fig. 6.6 b)).

By breaking the symmetry of the slot structure as demonstrated in Fig. 6.7 a) where the upper slab is only 5 nm thicker than the lower slab outside of the rib, the minor field of the quasi-TM polarized slot mode gets even components. Now, coupling can occur and the structure is leaky as shown in Fig. 6.7 a).

By further reducing the slab thickness the system enters region III, where the effective index of the quasi-TM polarized slot mode is higher than both TE slab modes and no coupling can occur. Such a leak proof structure can only be obtained by drastically reducing the outer slab height (see Fig. 6.7 b)).

This page has been intentionally left blank

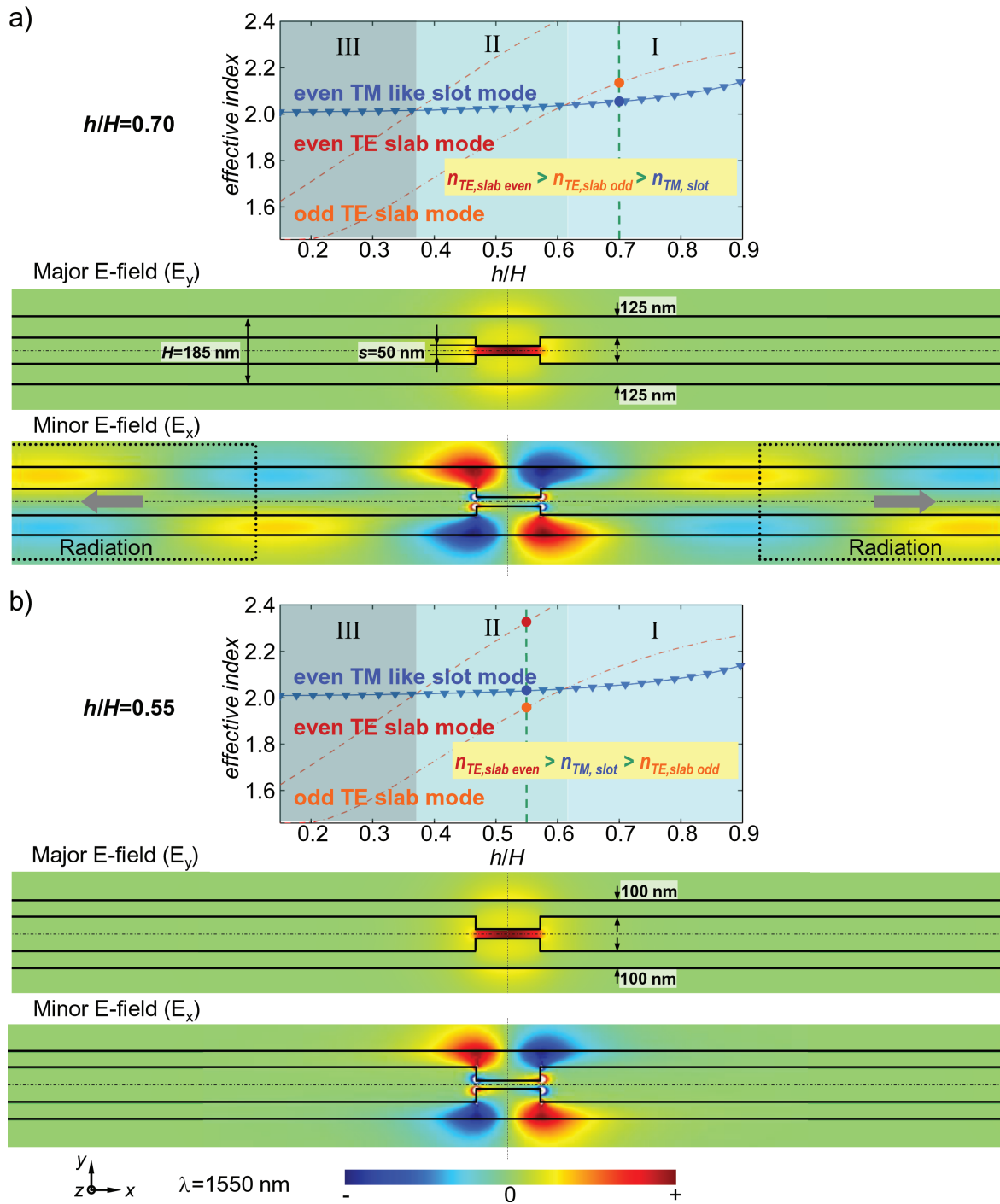


Figure 6.6.: Rib type slot waveguide with a fixed $H = 185$ nm and $s = 50$ nm. a) Electric field of the symmetric rib-type slot waveguide in the region where the effective index of the TM polarized slot mode is below both TE polarized slab modes (even and odd), b) electric field of a symmetric rib-type slot waveguide where the effective index of the TM polarized slot mode is higher than the odd but lower than the even TE slab mode. The effective index of the TM slot mode was calculated using FEM. The index of the two slab modes was calculated from the 2D infinite slab system.

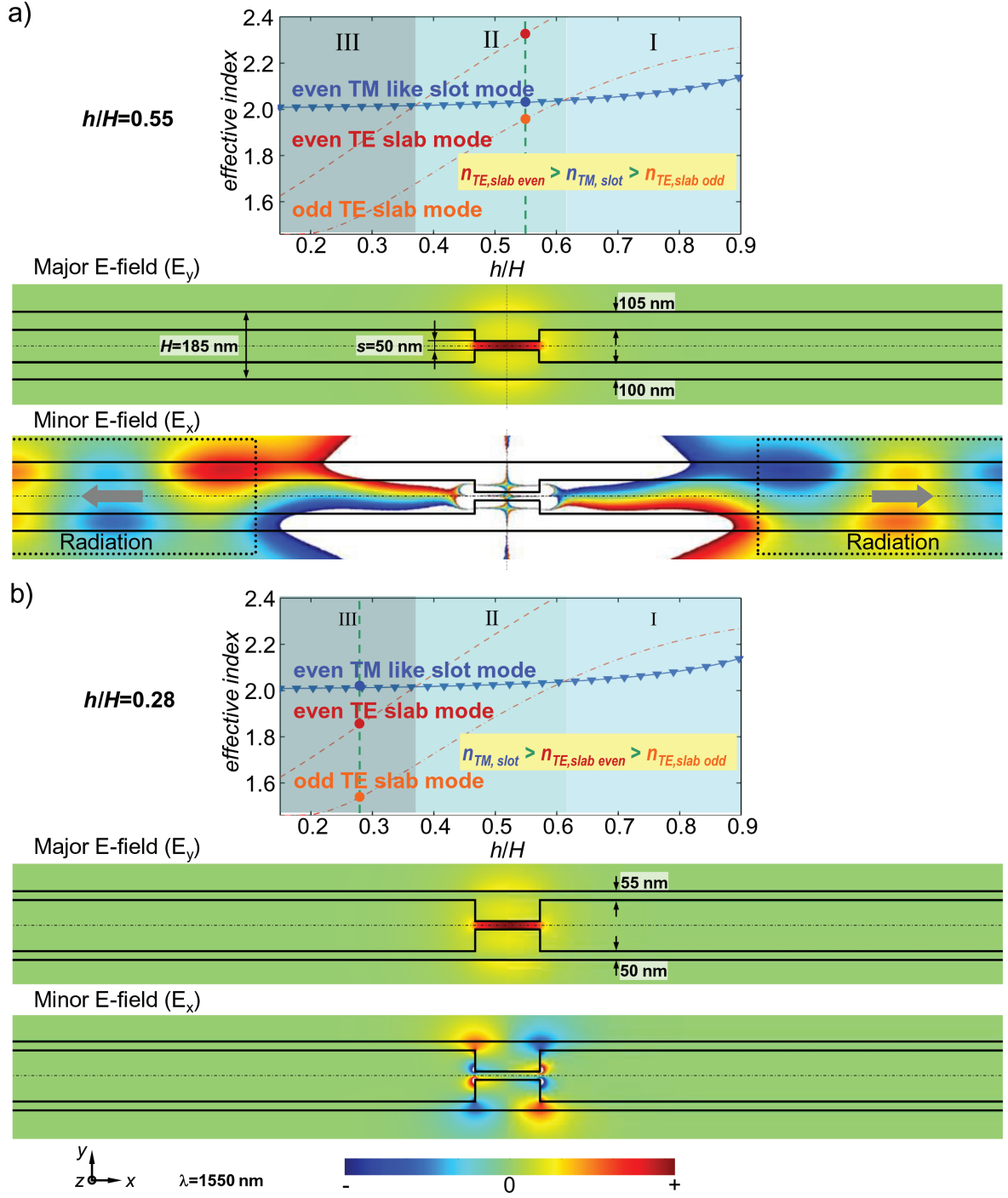


Figure 6.7.: Rib type slot waveguide with a fixed $H = 185 \text{ nm}$ and $s = 50 \text{ nm}$. a) Electric field of a symmetric rib-type slot waveguide with imperfections where the effective index of the TM polarized slot mode is higher than the odd- but lower than the even TE slab mode, b) electric field of a symmetric rib-type slot waveguide with imperfections for a structure, where the effective index of the TM polarized slot mode is higher compared to both TE polarized slab modes. The indices were calculated with the same methods as described for 6.6. h/H is defined as the ratio of the slab height h to the rib height H .

6.2.2. Fully symmetric slot waveguide structure

In order to study the principle behavior of this effect and to quantify the losses which can arise, a fully symmetric slot waveguide structure such as used for Fig. 6.6 was studied in-depth. Figure 6.8 a) and b) again show the effective indices of the TM-like slot mode and the even TE-slab mode as a function of h/H for structures with $H=137$ nm, $w=400$ nm, and slot thicknesses $s = 150$ nm and $s = 50$ nm, respectively. The thickness H corresponds to the value at which the fraction of optical power confined in the slot of a slot waveguide slab system is maximum. The effective index $N_{\text{eff,TM}}$ of the TM-like slot mode was calculated numerically using the variational mode-matching (VMM) method (see section 3.2 and appendix B), the effective indices $n_{\text{eff,TE,even}}^{(\text{slab})}$, $n_{\text{eff,TE,odd}}^{(\text{slab})}$ of the even and odd TE slab modes were determined again semi-analytically by solving the transcendent eigenmode equation of a five layer slab system. Figure 6.8 c) and d) plot the leakage values derived from the imaginary part of the effective index of the TM-like slot mode calculated by the VMM simulations. The vertical dashed lines indicate the thickness used for the

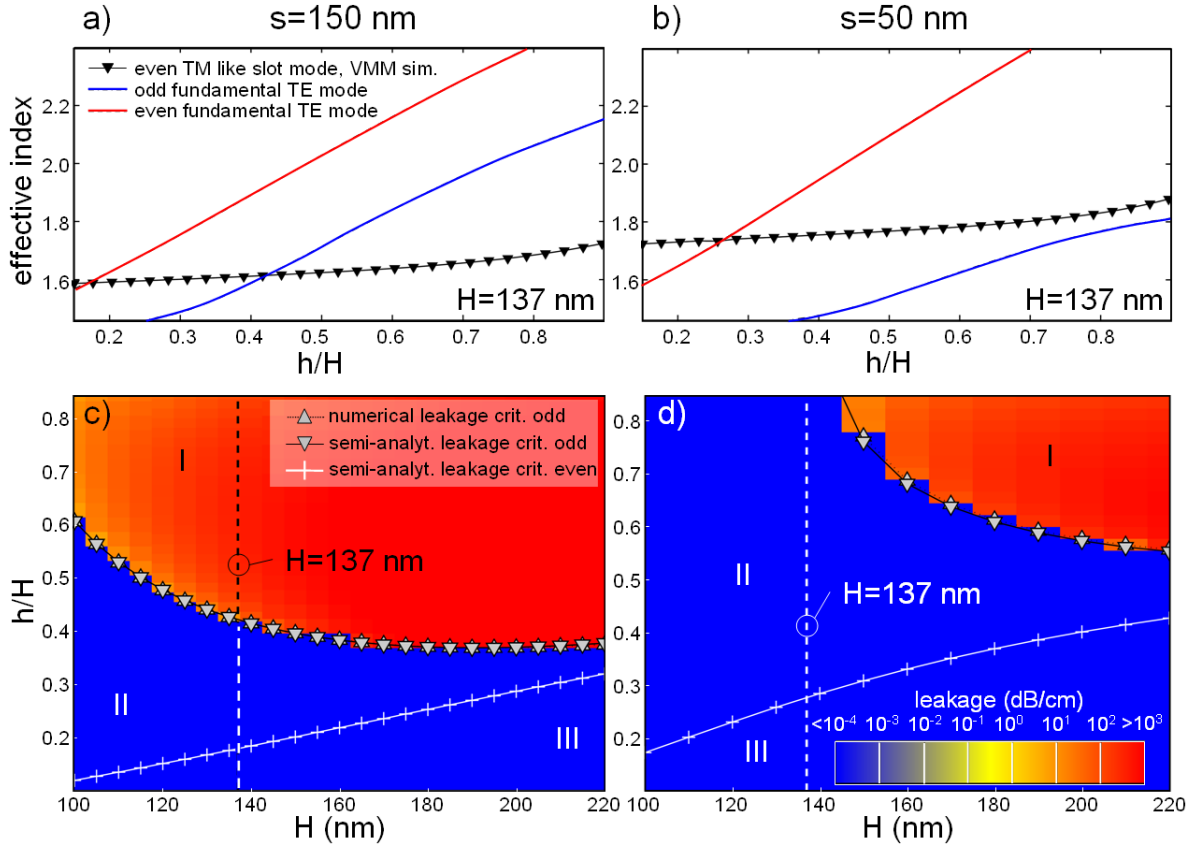


Figure 6.8.: Effective indices of the TM-like slot mode and the even and odd TE slab modes as a function of the relative slab thickness h/H for $H=137$ nm, $w=400$ nm and for two slot thicknesses, (a) $s=150$ nm and (b) $s=50$ nm at $\lambda=1.55$ μm ; (c) and (d) show the lateral leakage losses of geometries with corresponding w and s , and the leakage criteria obtained numerically from the real part of the effective indices of the VMM simulation (upward-pointing triangles) and using the effective index method (downward-pointing triangles). The vertical dashed lines indicate the thickness used for the computation of the effective indices in (a) and (b).

computation of the effective indices in Fig. 6.8 a) and b). A comparison of the leakage values along the line in Fig. 6.8 c) with the refractive index values shown in Fig. 6.8 a) reveals that the abrupt change of the leakage loss matches with the boundary between region I and II at $h/H = 0.42$, where

$$N_{\text{eff,TM}} = n_{\text{eff,TE,odd}}^{(\text{slab})}. \quad (6.1)$$

For structures with smaller values of h/H the lateral leakage loss becomes zero, although the effective index of the even TE slab mode still exceeds that of the TM-like slot mode. The boundary between region II and III is defined by

$$N_{\text{eff,TM}} = n_{\text{eff,TE,even}}^{(\text{slab})}. \quad (6.2)$$

Due to the perfect symmetry of the slot waveguide structure in vertical direction, the minor field of the even fundamental TM mode has no even components which could couple to the even TE-slab mode. As shown in Fig. 6.8 b), for a slot thickness of $s = 50$ nm the effective index of the odd TE-slab mode lies below the effective index of the TM-like slot mode over the whole range of h/H and consequently no leakage occurs (see Fig. 6.8 d) region II). Calculating the relative thickness h/H where the relationship (6.1) is fulfilled at other waveguide thicknesses H provides a leakage criterion for perfectly symmetric rib-type slot waveguides, which agrees well with the abrupt changes of the leakage losses in Fig. 6.8 c) and d).

6.2.3. Semi-analytic leakage criterion

Lateral leakage in a perfect symmetric rib-type slot waveguide only occurs above a critical relative slab thickness h/H for which equation (6.1) is fulfilled. Latter can be calculated semi-analytically by solving the transcendent eigenmode equation of a five layer slot waveguide slab, whereas the effective index of the TM-like slot mode has to be determined by fully vectorial 2D mode solvers. In order to avoid a time-consuming analysis we approximate the effective index of the TM-like slot mode by solving the transcendent eigenmode equation of a slot waveguide slab system for the inner and outer region of the rib-type slot waveguide structure and applying the well-known effective index method [117]. In Fig. 6.8 c) and d) the leakage criterion using the real part of the effective index of the VMM simulation (upward-pointing triangles) is compared with the leakage loss values obtained from the same simulations. This numerical criterion agrees well with the abrupt change in leakage loss values, demonstrating the validity of the stated criterion. Moreover, the semi-analytic criterion (downward-pointing triangles) is almost identical with the numerical findings obtained by the VMM method even for the rather small waveguide width of $w=400$ nm. Therefore, a computationally inexpensive and, nevertheless, sufficiently accurate elaboration of design rules for leak-proof rib-type slot waveguides is facilitated by semi-analytical methods.

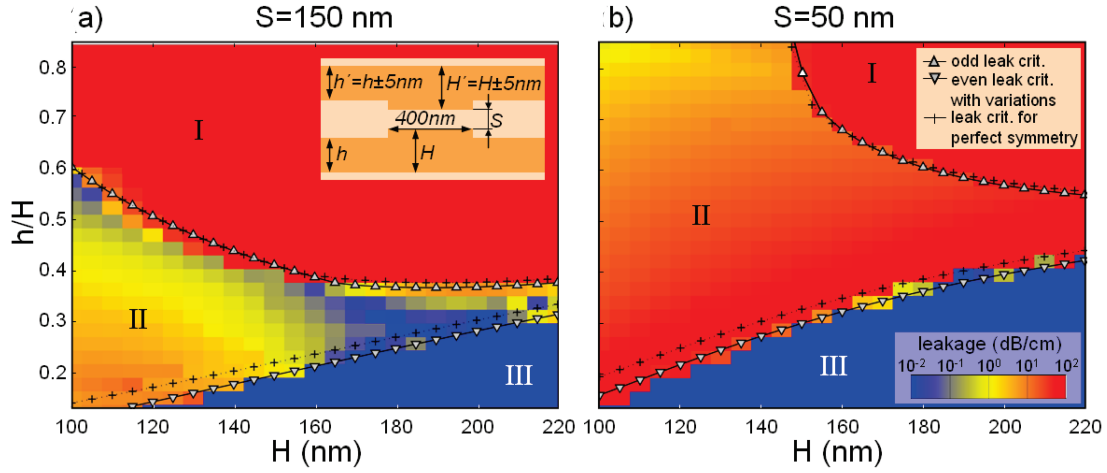


Figure 6.9.: Leakage loss of rib-type slot waveguides with thickness variations of ± 5 nm in the upper rib structure for a) $S=150$ nm and b) $S=50$ nm at $\lambda=1.55$ μ m. The semi-analytical leakage criteria for odd (upward-pointing triangles) and even (downward-pointing triangles) TE slab modes are calculated for the most critical structure $H' = H - 5$ nm and $h' = h + 5$ nm. The crosses represent the leakage criteria of a perfectly symmetric system.

6.2.4. Influence of asymmetries

In practice, perfectly symmetric structures are not achievable and variations of the geometry parameters caused by fabrication processes have to be taken into account. These variations lead to an even contribution in the minor field of the TM-like slot mode, thus enabling the coupling of the TM-like slot mode with the even TE slab mode. In order to study the influence of the deviations on the leakage loss the thicknesses h' and H' of the upper rib waveguide are varied by ± 5 nm (see inset of Fig. 6.9 a)) resulting in four different geometries. For each geometry the leakage loss is calculated with the VMM solver and the maximum value is plotted for each point of H and h/H in Fig. 6.9. Due to the asymmetry induced by the deviations, waveguide geometries in region II become lossy. Although much lower than in region I these leakage losses can limit the practical usability of waveguides in region II. Taking into account the slight asymmetry of the structure, the semi-analytic solutions of the leakage criteria (6.1) for the odd (upward-pointing triangles) and (6.2) for the even (downward-pointing triangles) TE modes agree well with the abrupt change of the leakage values calculated by VMM. Both criteria are calculated for the most critical geometry, which is $H' = H - 5$ nm and $h' = h + 5$ nm. With respect to the leakage criteria of the perfectly symmetric system (crosses) only the leakage criterion for the even TE slab mode shows a significant shift to lower values of h/H .

6.2.5. Influence of geometry

The leakage criteria for coupling to the even and odd TE slab modes depend strongly on the geometry parameters, as shown in Fig. 6.10. With decreasing slot thickness s the criteria shift to higher values of h/H (see Fig. 6.10 a)). Moreover, region II expands and region I vanishes over an increasingly large range of H , thus enabling leak-proof perfectly symmetric geometries for arbitrary h/H .

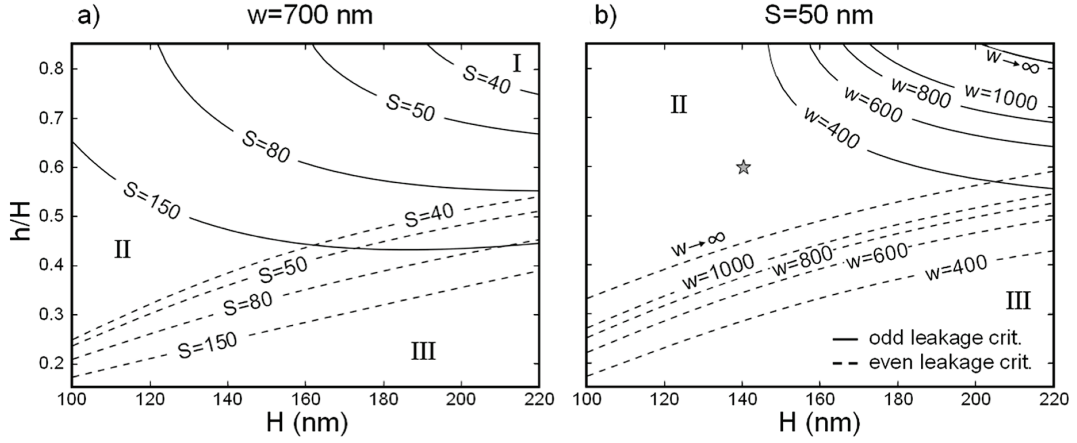


Figure 6.10.: a) Influence of the slot thickness s at $w = 700$ nm, and b) of the rib width w at $s = 50$ nm on the leakage criteria for coupling to the even (dashed lines) and odd (solid lines) TE slab modes.

The dependence on the waveguide width w is less pronounced because the width has only a minor impact on the effective index of the slot mode. The influence of w on the leakage criteria is inverse to that of the slot thickness. For wider waveguides the leakage criteria shift to higher values of h/H .

6.2.6. Resonance effects for slot waveguides with asymmetries

It has been demonstrated that resonance effects can reduce the horizontal leakage losses due to TM-TE coupling for certain waveguide widths in otherwise leaky rib waveguide geometries [116, 118]. These resonance effects originate from a destructive interference of TE waves generated by TM-TE mode conversion at the rib walls. While one part of these TE waves propagates into the slab region the other part is reflected at the side wall and traverses inside the rib to the other side wall, where it interferes with newly generated TE waves. For certain rib widths this results in a cancellation of TE waves leaking into the slab region thus suppressing the leakage loss. The resonant widths can be calculated using the effective indices $N_{\text{eff,TM}}$ of the TM-like rib mode and $n_{\text{eff,TE}}^{(\text{Core})}$ of the TE slab mode of the layer system in the core region. In the case of rib-type slot waveguides these resonance effects can also be exploited to suppress lateral leakage due to TM-TE coupling. However, resonances related to the even and odd slab modes occur at different widths:

$$w_{\text{even}} = \frac{m \cdot \lambda}{[(n_{\text{eff,TE,even}}^{(\text{Core})})^2 - (N_{\text{eff,TM}})^2]^{1/2}} \quad (6.3)$$

$$w_{\text{odd}} = \frac{m \cdot \lambda}{[(n_{\text{eff,TE,odd}}^{(\text{Core})})^2 - (N_{\text{eff,TM}})^2]^{1/2}}, \quad (6.4)$$

where m is an integer with $m > 0$.

For a perfectly symmetric waveguide geometry in region I the cancellation of the coupling to the odd TE slab mode at widths given by (6.4) results in an efficient suppression of lateral leakage. Slight variations of the waveguide geometry give rise to even TE field components and, thus,

coupling to the outer slab occurs again, which prevents a complete leakage cancellation. The exploitation of the resonance effect is of particular interest for waveguide geometries with large slot widths having a large region I. As an example, Fig. 6.11 a) shows the leakage loss of a waveguide geometry with $s=100$ nm, $H=140$ nm, and $h=105$ nm, *i.e.*, $h/H=0.75$, as a function of the waveguide width. Structural deviations of ± 5 nm lead to small shifts of the resonance widths, which are caused by a change of the effective indices. Due to the narrow shaped resonances these shifts translate into a sharp increase of leakage losses.

From a practical point of view, resonance effects are more interesting for waveguide geometries in region II, where leakage losses occur only in the presence of slight asymmetries via coupling to the even TE slab mode. Since these leakage losses are much smaller than in region I (see Fig. 6.9) shifts of the resonances caused by deviations of the geometry have less impact on the propagation performance. Therefore, waveguide designs with widths fulfilling the resonance condition offer an improved fabrication tolerance because waveguides with deviations from the perfectly symmetric design operate in the vicinity of the resonant minimum, where losses are still small. Figure 6.11 b) plots the leakage loss of a waveguide geometry with $s=50$ nm, $H=140$ nm, and $h=84$ nm, *i.e.*, $h/H=0.6$ (indicated by a star in Fig. 6.10 b)). The period of the widths at which cancellation occurs according to (6.3) is reduced because of the higher index difference between the even TE slab mode of the core region and the TM-like slot mode compared to the structure in Fig. 6.11 a).

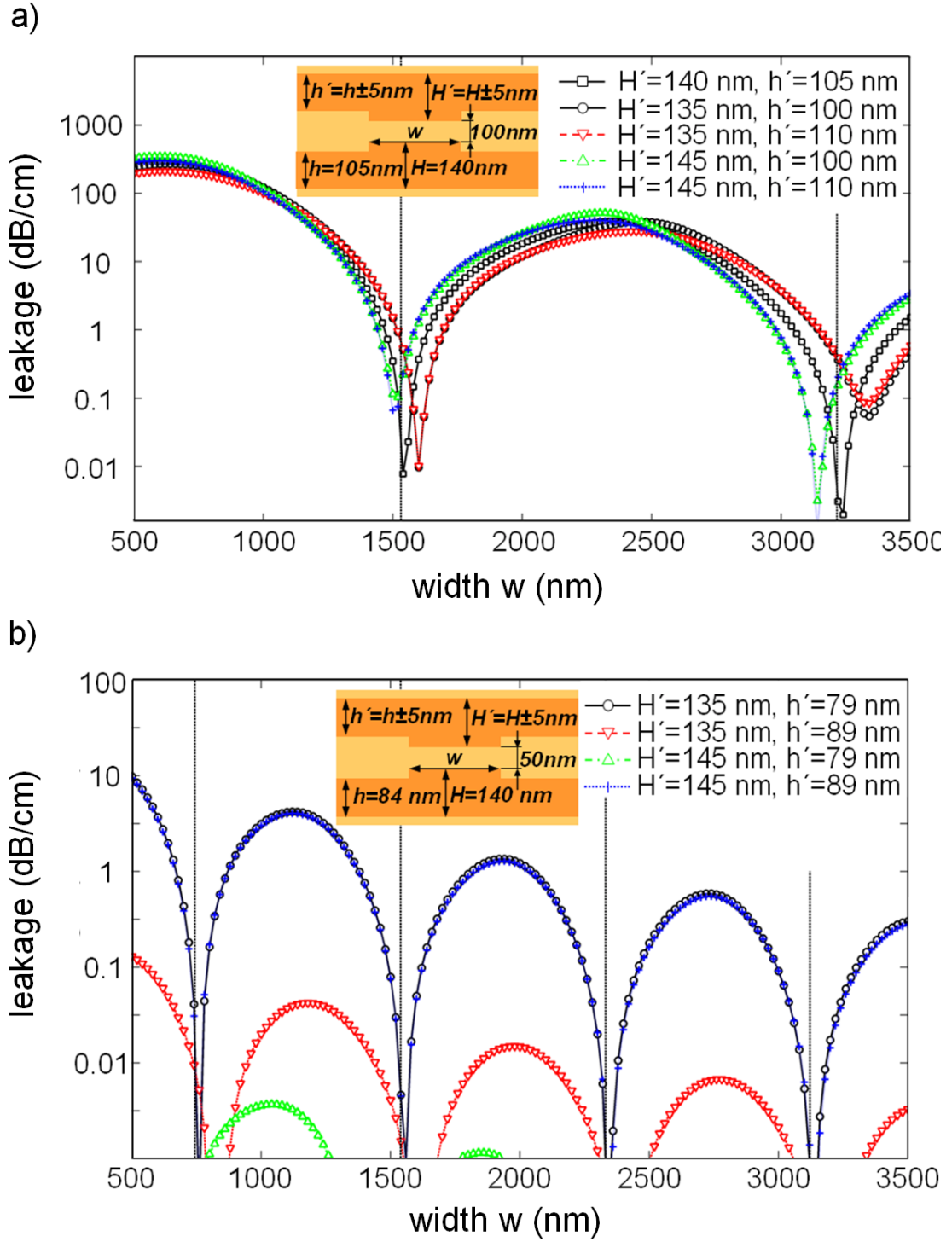


Figure 6.11.: Resonant cancellation of the leakage to a) the odd TE slab mode in region I and b) the even TE mode in region II. The dashed lines indicate the waveguide widths calculated semi-analytically for the perfectly symmetric structures, i.e., $H' = H$ and $h' = h$, at which resonances occur for odd and even TE modes, respectively.

6.2.7. Asymmetric slot waveguide structures

From the practical point of view, an asymmetric structure such as depicted in 6.12 a) would be of interest because it offers the advantage of electric wiring, which is a prerequisite for many active photonic components. Compared to a fully symmetric slot waveguide as studied in the preceding sections and as proposed for active photonic devices in [38], the structure consisting of one slab and a rib structure on top has the advantage of significantly eased fabrication because only one etch step is necessary. This avoids the necessity of exact alignment to micrometer sized structures.

The wire/slab-type slot waveguide shown in Fig. 6.12 b) is another interesting slot waveguide. It could offer better lateral confinement compared to the rib type and therefore would be particularly attractive for waveguide sections in active photonic devices where no direct electrical wiring is necessary. Moreover, for both structures the amount of etched interfaces are significantly reduced. This would minimize scattering losses at these comparably rough surfaces. One result of the preceding section was, that for the symmetric structures an optimum of symmetry is advantageous. Contrary for the asymmetric system it is not necessary to restrict the thickness of the upper and lower silicon layer to the same value to ensure symmetry, due to the intrinsic asymmetry of the structures Fig. 6.12 a) and b). Therefore, an additional parameter H_{Slab} is introduced, defining the thickness of the lower waveguiding layer. In addition it is important to note, that the etch depth e is defined relative to the overall thickness of the structure H_{Str} . This approach was chosen to be consistent with definitions typically used for standard rib waveguides.

For both structures lateral leakage occurs because their intrinsic asymmetry allows coupling to both TE slab modes outside of the waveguide core. The leakage losses are of the order of 10^2 dB/cm over a wide range as Fig. 6.12 c) exemplarily shows. A possibility to overcome this disadvantage would be to reduce the thickness of the slab H_{Slab} or to reduce the thickness h of the upper slab outside of the core while both layers remain thick enough to allow electrical wiring for the rib type structure as shown in Fig. 6.12 a).

However, as Fig. 6.13 demonstrates, both strategies are not effective for structures which should operate in the vicinity of the power optimized slot waveguides found in chapter 5. In Fig. 6.13 a) the

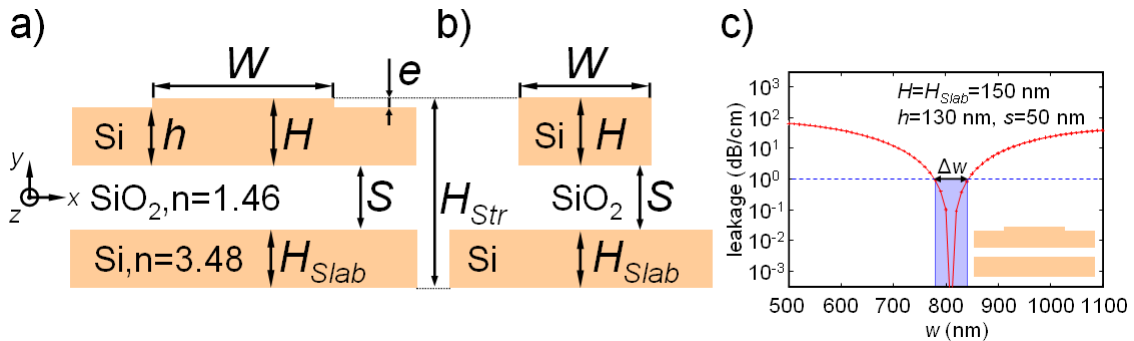


Figure 6.12.: Cross sections of a) rib-type and b) wire/slab-type slot waveguide structures. c) Typical width dependent resonance behavior of a rib-type slot waveguide; Δw defines the range of width within which lateral leakage losses are below 1 dB/cm. The calculations are based on a rib type slot waveguide with the parameters $H = H_{\text{Slab}} = 150$ nm $h = 130$ nm $s = 50$ nm.

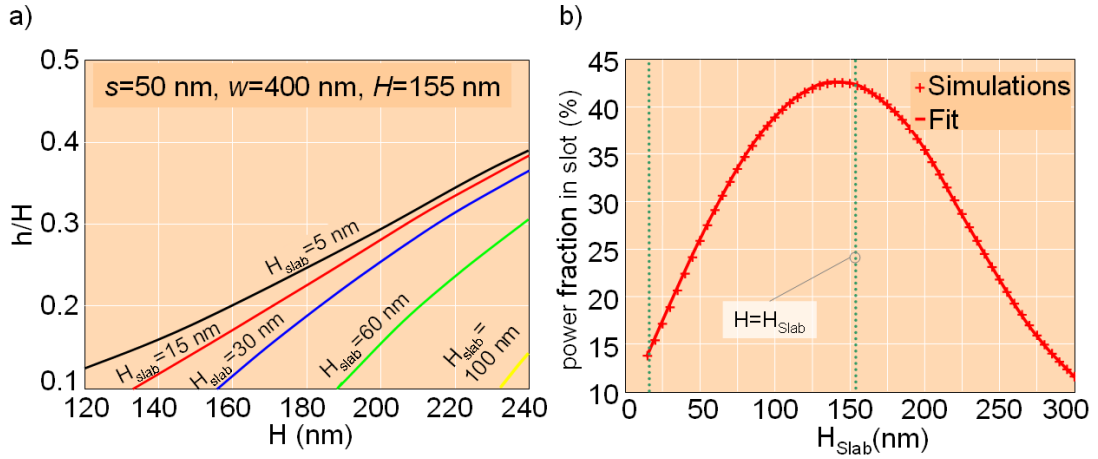


Figure 6.13.: a) Leakage criterion given by equation (6.2) for five different thicknesses of the lower slab H_{slab} in dependence on the thickness of the upper layer H . The parameter region below the corresponding line is leakproof. b) Light power percentage in the slot in dependence on the thicknesses of the lower slab H_{slab} for a constant layer thickness of $H = 155$ nm. The other waveguide geometry parameters are identical to a). The refractive indices of the layers, slot- and surrounding region can be seen in 6.12 a).

transition from region II to region III, where the effective index of the quasi-TM polarized slot mode becomes higher than the effective index of both TE slab modes (defined by equation (6.2)) is plotted for different thicknesses of the lower slab H_{slab} in dependence on the upper layer thickness H . The plot reveals that a leakproof structure (the area below the corresponding line) can only be achieved either by increasing the thickness of the upper waveguide H to well above 250 nm or by reducing the slab thickness H_{slab} to only a couple of nanometers. The lines are the results of calculations using the effective index approximation. For a structure with a large upper slab thickness H it is obvious that the optical power is confined in the upper slab and almost no slot effect is apparent. On the other hand, for a structure with a fixed $H = 155$ nm and a reduced slab thickness H_{slab} Fig. 6.13 b) shows the influence of the increased asymmetry of the structure on the light power confinement (calculated in the same manner as describe in chapter 5). With increased asymmetry, the light power confined in the slot region is decreased. For a slab thickness of $H_{\text{slab}} = 15$ nm the power fraction is reduced to 14%. It is important to point out, that the optimized structure is slightly off the completely symmetric system with respect to the layer thicknesses. This can be explained by the introduced asymmetry between the two layers. The upper layer has an etch step, whereas the lower layer has not.

In summary, it can be stated that a strong thickness asymmetry between the two layers H and H_{slab} , which would be necessary to obtain a leak proof slot waveguide structure leads to a sacrifice of the slot effect. Nevertheless, also this completely asymmetric structure features resonances, where the leakage loss drops below 10^{-3} dB/cm as Fig. 6.12 c) illustrates. By exploiting these resonance effects for otherwise leaky geometries, low loss operation becomes possible without sacrificing optical power confinement in the slot. Major issues that have to be taken into account in this context are variations of the realized waveguide structure from the design values. An exploitation of the

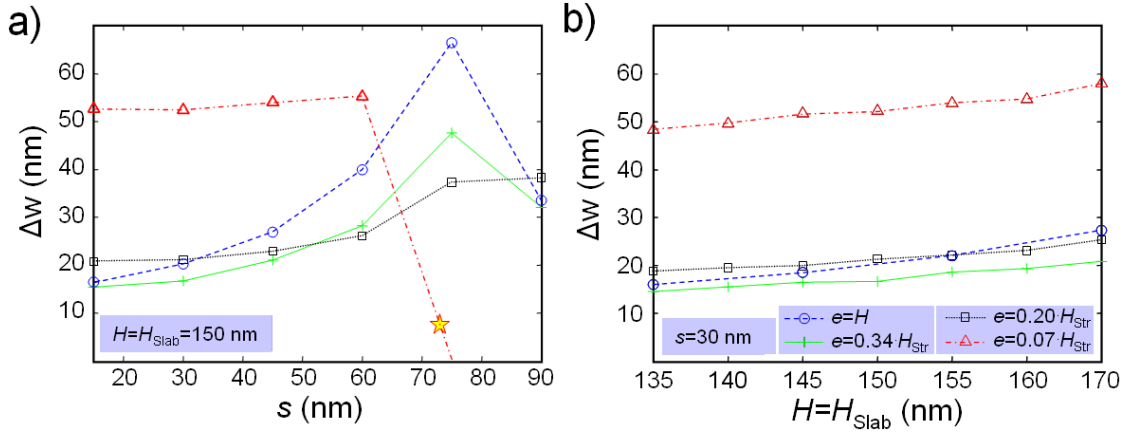


Figure 6.14.: Dependence of Δw on a) the slot thickness s and on b) the waveguide thicknesses $H = H_{\text{Slab}}$ for different etch depths e . The star indicates the slot thickness where coupling to the odd TE slab mode occurs, and no width range Δw for low loss operation can be obtained any more.

resonance effect is only possible, if the losses in the vicinity of the resonant minimum are still sufficiently low.

6.2.8. Influence of imperfections

With respect to deviations of the geometry caused by fabrication processes the rib width, which is influenced by the lithography and the etching process is the most critical parameter. Thus, the width range for which leakage losses are small has to be maximized to ensure low loss operation for waveguides with slightly fluctuating width. For this purpose, we define Δw as the width range for which losses are below 1 dB/cm (see Fig. 6.12 (c)) and study this parameter in dependence of the geometry parameters. For the in-depth study, the full vectorial VMM eigenmode solver was used to treat the lateral infinite large waveguide physically as correct as possible.

The etch depth e has a major impact on Δw as Fig. 6.14 a) reveals. It turns out, that for shallow etch depth e a sufficient large Δw can be found. The influence of the slot thickness is comparatively small. However, for rib-type slot waveguides the applicable range of s is limited by the effective index of the odd TE slab mode outside of the rib [36]. If the effective index of the odd TE slab mode becomes higher than that of the TM-like slot mode leakage occurs again because the resonance condition can only be fulfilled for one of the two TE slab modes at the same time. In the example shown in Fig. 6.14 a) this situation occurs for $e = 0.07 H_{\text{Str}}$ at $s \approx 70$ nm. With increasing etch depth this effect diminishes and for the slab/wire-type, i.e., for $e = H$ the effective index of the even and odd TE slab mode outside the rib become identical.

The dependence of Δw on the thicknesses H and H_{Slab} is almost negligible (see Fig. 6.14 b)) while the etch depth has a strong influence. Asymmetries in the amount of $H_{\text{Slab}} = H \pm 15$ nm do not affect the Δw as well. As a consequence of Fig. 6.14, the etch depth e is a suitable parameter to increase the resonance width Δw , where losses are low. Apart from the width range Δw also the shift of the rib width w_{Res} at which the resonance occurs under variation of certain geometry parameters is of high importance. It would be advantageous to find waveguide geometries, where the shift of

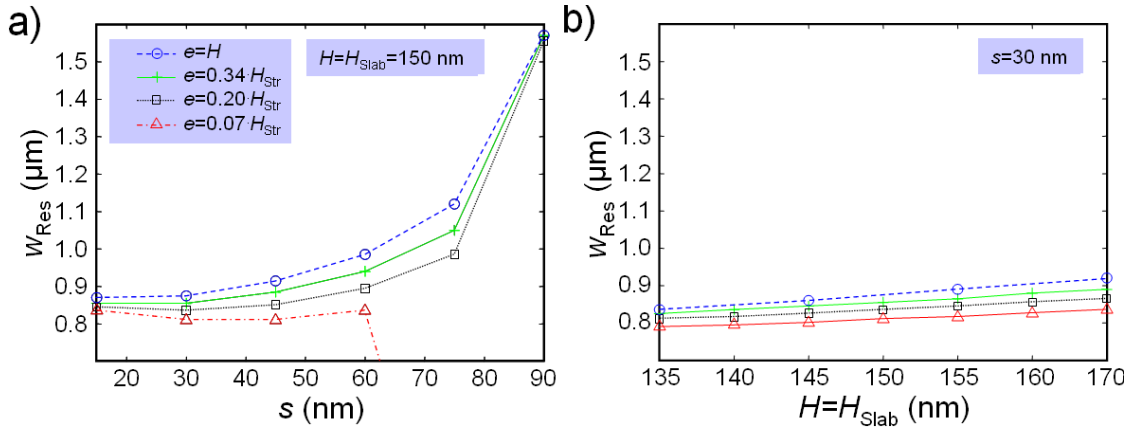


Figure 6.15.: Width w_{Res} for which the resonance occurs as a function of a) the slot thickness s and b) the waveguide thickness $H = H_{\text{Slab}}$ for different etch depths e . In b) a fixed slot thickness of $s = 30$ nm was assumed.

the resonance width is at minimum under their variation.

Figure 6.15 a) reveals that the slot thickness has a major impact on w_{Res} for $s > 70$ nm, whereas the slope of w_{Res} for small slot thicknesses of the range $s = 30$ nm is at minimum in dependence on the slot thickness. From the same plot one can learn that the impact of the etch depth e on the shift of the resonance width is small compared to that of the slot thickness. Again, the coupling to the odd mode occurs for very shallow etch depth in combination with a slot thickness of $s \geq 60$ nm. The influence of the waveguide thickness $H = H_{\text{Slab}}$ on the shift of the resonant width w_{Res} is small as shown in Fig. 6.15 b). Here, intentionally a fixed slot thickness of 30 nm was assumed, due to the fact that there the shift of the resonance width under variation of the slot thickness was at minimum. Moreover, in Fig. 6.15 b) the weak dependence of the resonance width on the etch depth becomes evident.

From the plots Fig. 6.14 and Fig. 6.15 it can be summarized that the etch depth can be used to maximize the width range where the losses are low in order to minimize the impact of the waveguide width variation on the leakage, while a small slot thickness of $s < 60$ nm ensures a minimized shift of the resonance under variation of the slot thickness. Not only the deviating width also the variations of the other geometry parameters and in particular their interdependence due to deviations caused by fabrication processes have to be taken into account. In order to study this influence we varied all geometry parameters, i.e., H , H_{Slab} , e and s by ± 5 nm resulting in sixteen different geometries. The variation of ± 5 nm is a realistic value considering today's possibilities of thinfilm technology. The leakage losses of all geometries in dependence on the width w were calculated, again using the VMM mode solver. As an example, Fig. 6.16 a) shows the leakage losses of all these geometries for a structure centered at $H = H_{\text{Slab}} = 135$ nm, $e = 0.081 H_{\text{Str}}$ and $s = 50$ nm. The envelope of these curves (solid red line) represents the maximum losses that can occur considering all possible variations. This envelope is a result of the shift of the resonant minimum w_{Res} for each geometry which leads to a reduction of the width range Δw compared to 50 nm for a perfect system.

Next, we studied the envelope characteristic for rib-type slot waveguides with different $H =$

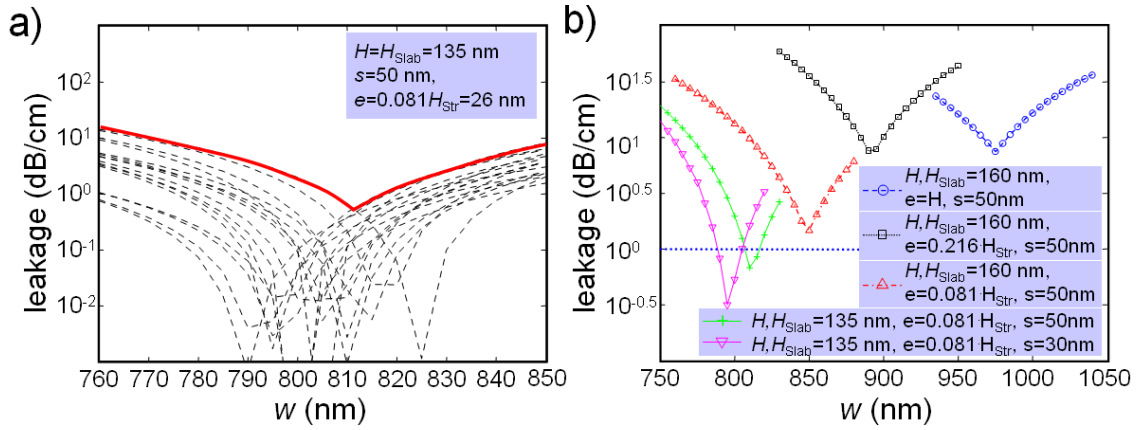


Figure 6.16.: a) Lateral leakage losses of a typical rib-type slot waveguide structure taking into account the variations of all geometry parameters by ± 5 nm. The envelope of these loss curves (solid red line) indicates the maximum losses that can occur; b) dependence of the maximum losses on the etch depth, waveguide thicknesses and slot thickness in order to find an optimized geometry which shows minimum losses under variation of all geometry parameters.

H_{Slab} , e and s (Fig. 6.16 b). As for the perfect system, also for the rib-type slot waveguides with variations the etch depth e and the slot thickness s have a major impact on the lateral leakage losses. Interestingly, smaller waveguide thicknesses H and H_{Slab} result in lower losses. This does not entail a sacrifice of the power confinement. The layer thicknesses are still close enough to the approximate optimum of 155 nm ensuring a very high power confinement in the slot region. For a rib-type slot waveguide with $H = H_{\text{Slab}} = 135$ nm, $e = 0.081 H_{\text{Str}}$ and $s = 30$ nm the width range of operation is larger than 20 nm.

Taken together, the results of this section show that small slot thicknesses of $s < 50$ nm, shallow etch depths and thin waveguides are beneficial for maximizing Δw . A slot waveguide structure fulfilling these demands allows a variation of the width of ± 10 nm while the lateral leakage losses are still below 1 dB/cm assuming that the other geometry parameters — the layer thicknesses H_{Slab} and H the slot thickness s and the etch depth e — do not vary more than ± 5 nm. From the practical point of view, these demands can be fulfilled and therefore, such a structure operating in the vicinity of a resonance is realistic. In fact, in [41, 42] this was demonstrated experimentally with a similar rib kind slot waveguide structure. As illustrated in Fig. 6.12 for a wire/slab system these optimizations are not sufficient because from the preceding discussion it can be concluded that a shallow etch depth is crucial to ensure a fabrication tolerant structure, and accordingly no low loss width range for geometries with variations of ± 5 nm can be obtained.

6.3. Conclusion

At the beginning of this chapter the substrate leakage of the wire type vertical and horizontal slot waveguide structure was investigated. It turned out, that there is no significant difference between the two concepts with respect to the necessary BOX thickness. A BOX layer larger than 2 μm is sufficient to ensure a leakproof structure. The main part of this chapter was dedicated to the lateral

leakage mechanism in symmetric SOI rib-type slot waveguides. It was demonstrated that by solving the transcendent eigenmode equation of the slot waveguide slab system and using the effective index method a leakage criterion for symmetric rib-type slot waveguides can be defined. We proved the validity of this approach by comparing with rigorous numerical simulations employing VMM. Taking structural deviations into account a stricter criterion for laterally leak-proof rib-type slot waveguide was obtained. Furthermore, a parameter region of leaky geometries was found, which can be of interest by exploiting resonance effects at certain widths, which reduce losses by orders of magnitude.

Moreover, as the studies revealed, even for asymmetric rib-type slot waveguides geometry parameters can be found which ensure both low loss operation and high optical power confinement in the slot. The results show that they can be designed to be sufficiently tolerant against variations of all geometry parameters. Therefore, rib-type slot waveguides have the potential to be utilized for applications where electric wiring or self-suspension are required without foregoing the inherent advantages of the horizontal configuration. It has to be mentioned in this context, that all presented studies assumed silica as slot material and similar calculation with air between the two waveguiding layers would reveal slightly other optimized geometry parameters.

For example, such self-suspended configurations could be advantageous, e.g. for sensing or for mechanically tunable devices. In addition, the requirements towards lithography are relaxed because single mode operation of these shallow structures is guaranteed also for wider waveguides.

7. Nonlinearities of slot waveguides

In all numerical studies of the preceding chapters linear behaviour was assumed, *i.e.*, the amplitude of the electric field has no impact on the optical properties of the material in which the light propagates. In practice, this holds only true for low electric field amplitudes. For high amplitudes the response of any dielectric material to light becomes nonlinear. The arising optical nonlinear effects are a very important part of photonics, because they allow to manipulate light in an all-optical way, *e.g.*, it is possible to change the frequency of light. Second harmonic generation or the frequency shift - typically from the infrared in the visible range - have to be mentioned in this context. Another important nonlinear optical effect is four wave mixing, where in presence of two input wavelengths two additional wavelengths are generated.

However, these effects can only be efficiently exploited if a sufficiently high electric field amplitude is obtained in the nonlinear material. Following an estimation in [88] the power of 10mW must be concentrated within an area of about $1\mu\text{m}^2$ in order to allow exploitation of nonlinear optical effects. Apart from increasing the optical power, concentrating the light in a smaller region increases the nonlinear optical interaction between light and matter. Here the slot waveguide comes into play. As pointed out already fundamentally in section 2.2.2, the concentration of light inside a small cross sectional area filled with a low index material is a unique feature of the slot waveguide structure. In order to take full advantage of this light concentration for nonlinear optical effects it is necessary to perform an optimization of the slot waveguide geometry.

7.1. Fundamentals

The response of any dielectric to light becomes nonlinear for intense electric fields \vec{E} . The electric polarization field \vec{P} can be written as [88, 119]:

$$\vec{P} = \epsilon_0 \vec{\chi}^{(1)} \vec{E} + \epsilon_0 \vec{\chi}^{(2)} \vec{E} \vec{E} + \epsilon_0 \vec{\chi}^{(3)} \vec{E} \vec{E} \vec{E} + \dots \quad (7.1)$$

The linear susceptibility $\chi^{(1)}$ contributes mainly to the polarization \vec{P} . The second order susceptibility $\chi^{(2)}$ is nonzero only for media made of molecules without inversion symmetry but even for these materials, $\chi^{(2)}$ is much lower than the linear susceptibility. Therefore, second order nonlinear effects such as second-harmonic generation and sum-frequency generation [120] occur only at high electric field amplitudes. In media with inversion symmetry the third-order susceptibility $\chi^{(3)}$ is responsible for phenomena such as third-harmonic generation, four-wave mixing, and in particular nonlinear refraction. In order to illustrate the origin of nonlinear refraction, let us evaluate eqn. (7.1)

for third order nonlinearity assuming linear polarized, monochromatic light :

$$P(\omega) = \epsilon_0 [\chi^{(1)} + \frac{3\chi^{(3)}Z_0}{2n} I(\omega)] \tilde{E}(\omega), \quad (7.2)$$

with \tilde{E} being the frequency dependent electric field amplitude and I the intensity, which follows from $I = n\tilde{E}\tilde{E}^*/2Z_0$. $Z_0 = \sqrt{\mu_0/\epsilon_0}$ is the so-called free space wave impedance. In contrast to the linear case, an intensity dependent term contributes to the polarization. The term in the square brackets can be seen as 'effective' susceptibility

$$\chi = \chi_0 + \Delta\chi(I), \quad (7.3)$$

or in a more convenient form as intensity dependent refractive index

$$n = n_0 + n_2 I. \quad (7.4)$$

The parameter n_2 is the so-called nonlinear refractive index defined as

$$n_2 \equiv \frac{3Z_0}{4n_0^2} \chi^{(3)}. \quad (7.5)$$

In other words, for a material with a sufficient high $\chi^{(3)}$, the refractive index depends on the optical intensity. This is the so-called 'Kerr-effect' [88, 119] which can be exploited in order to modulate the phase of the light by changing its intensity. Moreover, this modulation is not restricted to a single wavelength. It is possible to use light with one wavelength to change the propagation in the nonlinear material for another wavelength. Such a cross phase modulation (XPM) enables important devices for telecom applications such as e.g. optical switches [119].

For all applications a maximized nonlinear effect is advantageous. As immediately can be deduced from eqn. (7.4), this can be done firstly by choosing a material with a high nonlinear refractive index n_2 . Typically, polymers feature a high nonlinear refractive index. The second possibility to maximize the nonlinear effect is to increase the light intensity I . This necessitates a waveguide structure allowing for strong optical confinement. In the case of polymers, conventional waveguides cannot achieved a strong confinement due to the low refractive index n_0 of polymers.

However, employing the slot waveguide structure it is possible to strongly confine light in a polymer embedded between two silicon wires and thus efficiently exploit the nonlinear behaviour of the polymer. The amount of third order nonlinear interaction in a waveguide is expressed by the nonlinearity coefficient $\gamma = k_0 n_2 / A_{\text{eff}}$, where k_0 is the angular wave number and A_{eff} the effective area. The effective area can be seen as a figure of merit of how well the waveguide geometry supports the nonlinear interaction. The smaller the effective area provided by the waveguide structure the higher the nonlinear interaction. Therefore, the effective area is the relevant parameter to evaluate the suitability of a certain waveguide structure for third order nonlinear optical applications.

Much effort has been spent already in the study and experimental demonstration of slot waveguide structures exploiting third order optical nonlinearity [15–27]. In particular the work of Koos

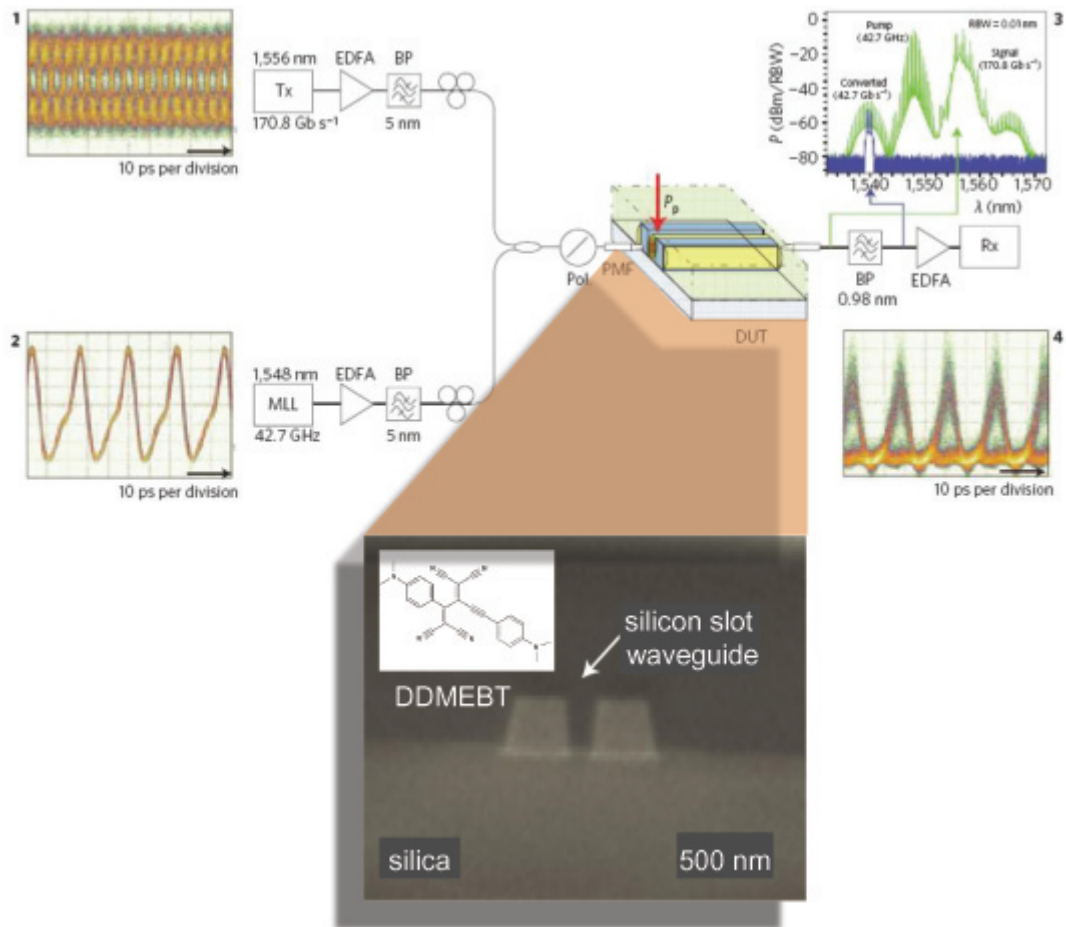


Figure 7.1.: Demultiplexing concept based on four wave mixing as described in [27]. The slot waveguide structure (see bottom) was filled with the highly nonlinear polymer DDMEBT. With this waveguide structure a demultiplexing speed of 42.7 Gb/s was achieved.

et al. has attracted much attention. There the authors showed that silicon-organic hybrid integration overcomes intrinsic limitations due to the slow dynamics of two-photon generated free carriers by combining the best of two worlds. Mature CMOS processing is used for the fabrication of a slot waveguide structure and molecular beam deposition is employed to cover it with organic molecules that efficiently mediate all-optical interaction without introducing significant absorption. A 4 mm long silicon-organic hybrid waveguide was fabricated with a record nonlinearity coefficient of $\gamma = 0.1 \text{ W}^{-1} \text{ mm}^{-1}$ to perform all-optical demultiplexing of 170.8 Gb s^{-1} to 42.7 Gb s^{-1} using a four wave mixing concept (see Fig. 7.1). A demultiplexer separates a signal consisting of multiple data streams transmitted via a shared medium back into single channels.

The potential of the vertical slot waveguide structure with respect to nonlinear effects has also been theoretically investigated by Koos *et al.* [20]. The dependence of the effective area of slot waveguides on the geometry was presented and it was predicted that the vertical slot waveguide can enable nonlinearity coefficients of up to $7 \text{ W}^{-1} \text{ mm}^{-1}$.

Their analysis focused on the vertical slot waveguide which can be fabricated from a single monocrystalline silicon layer but puts high demands on the fabrication process due to the small fea-

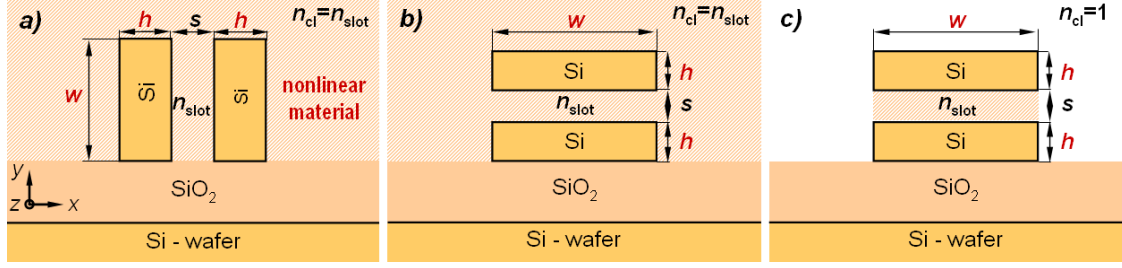


Figure 7.2.: Cross sections of the three investigated implementations of slot waveguides filled and/or covered with a low index optically nonlinear material: a) vertical slot waveguide, b) and c) horizontal slot waveguides.

ture sizes. The minimum achievable slot thickness is practically limited to >50 nm. This explains why the authors of [20] restricted their studies to slot thicknesses $s > 50$ nm. As described in detail in section 2.4 for the horizontal type such a restriction is not given. It is possible to realize horizontal slot waveguides with ultra thin slot layers by taking advantage of the possibilities of thinfilm technology as demonstrated in [41, 42].

Another report [18] theoretically evaluated both vertical and horizontal silicon-based slot waveguide structures with respect to their nonlinear behavior. However, no multi parameter optimization with respect to all geometry parameters was performed in order to find the waveguide geometry that provides maximum nonlinear interaction. Moreover, the low index contrast approximation was used for calculating the effective area of nonlinear interaction instead of the precise equation [20], which can give quantitatively misleading results as will be discussed later on.

The first thorough theoretical study taking the advantage of horizontal slot waveguides fully into account has been reported in [24]. There, for the first time it was pointed out, that the slot waveguide structure has an absolute optimum with respect to nonlinear interaction which can be achieved in the horizontal concept only. The results were compared with the optimized values of the vertical slot structure and, in addition, a possibility was pointed out how the nonlinear interaction can be further increased.

7.2. Simulation model and technique

Figure 7.2 illustrates the cross section of the investigated vertical and horizontal slot waveguide structures. In the case of the vertical slot waveguide for practical reasons it was assumed that the whole structure is covered with the nonlinear material. Horizontal slot waveguides, on the other hand, can be implemented either with a thin low index layer with the thickness s and a linear refractive index of n_{slot} embedded between two silicon wires. The lower cladding is a silicon dioxide layer, the upper cladding is either air ($n_{\text{cl}}=1$) or the same nonlinear material as in the slot region ($n_{\text{cl}}=n_{\text{slot}}$). In this model, it was assumed that the nonlinear interaction only occurs in the low index material in the slot region. The amount of third order nonlinear interaction in a waveguide is expressed by the nonlinearity coefficient $\gamma = k_0 n_2 / A_{\text{eff}}$, where k_0 is the angular wavenumber, n_2 the nonlinear refractive index of the nonlinear material, and A_{eff} the effective area. The effective area

can be seen as a figure of merit of how well the waveguide geometry supports the nonlinear interaction. The smaller the effective area provided by the waveguide structure the higher the nonlinear interaction. In high index contrast waveguide structures the effective area is defined by [20]:

$$A_{\text{eff}} = \frac{Z_0^2}{n_{NL}^2} \frac{\left| \int \int_{D_{\text{total}}} \text{Re}[\vec{\mathcal{E}}(x,y) \times \vec{\mathcal{H}}^*(x,y)] \cdot \vec{e}_z dx dy \right|^2}{\int \int_{D_{NL}} |\vec{\mathcal{E}}(x,y)|^4 dx dy}, \quad (7.6)$$

where $Z_0 = \sqrt{\mu_0/\epsilon_0}$ is the free space wave impedance, n_{NL} the refractive index of the nonlinear material, $\vec{\mathcal{E}}(x,y)$ the vectorial electric, and $\vec{\mathcal{H}}(x,y)$ the vectorial magnetic field profiles of the waveguide mode of interest. In the context of nonlinear interaction the modes of interest are the TE-like mode for the vertical slot waveguide and the TM-like mode for the horizontal slot waveguide as explained before. The upper integral extends over the whole cross section D_{total} , whereas the lower integral is limited to the area covered by the nonlinear material D_{NL} .

We employed the finite element method (FEM) based mode solver (see section 3.1) for the calculation of the waveguide eigenmodes. The $4 \times 4 \mu\text{m}$ simulation domain was surrounded by $0.4 \mu\text{m}$ thick perfectly matched layers. An adaptive mesh refinement was used to ensure sufficient accuracy. For that purpose, the mesh was refined as long as the calculated effective area of two consecutive simulations showed a difference larger than $10^{-5} \mu\text{m}^2$. This ensures that the simulation domain was meshed sufficiently to obtain convergence of the desired value of the effective area.

In order to find the waveguide cross section that provides a minimum effective area, *i.e.*, maximum nonlinear interaction, for a given slot thickness we implemented an iterative search. In a first step, a course grid of width and height values was defined comprising the structure featuring maximum nonlinear interaction. Then, the corresponding effective areas were calculated using the FEM tool. Next, a two dimensional fit was performed followed by a search for the minimum effective area within this two dimensional fit. Around this minimum, the grid of width and height values was refined and the effective areas were calculated again. This procedure was repeated until the difference of the obtained minimum effective areas between two iterations was smaller than $10^{-4} \mu\text{m}^2$ and until the resolution of the grid was better than 1 nm. In order to obtain the effective area, the upper integral of equation (7.6) was carried out numerically over the entire simulation domain excluding the perfectly matched layers. For the denominator of equation (7.6) the area where the nonlinear material is present was used for the integration.

7.3. Results

First, we studied a horizontal slot waveguide slab system as depicted in Fig. 7.3 a), where the slot is filled with an optically nonlinear material. The refractive index of the nonlinear material is set to 1.46. By solving the analytic eigenmode equation of this five layer system as described in 2.2.2 the electric and magnetic mode field profiles of the TM mode in y -direction can be calculated. The integration was numerically carried out using an Mathematica routine [93] and finally the effective area was calculated using equation (7.6). Figure 7.3 a) plots the optical power confined in the slot region and the effective area per unit length in x -direction as a function of the silicon layer

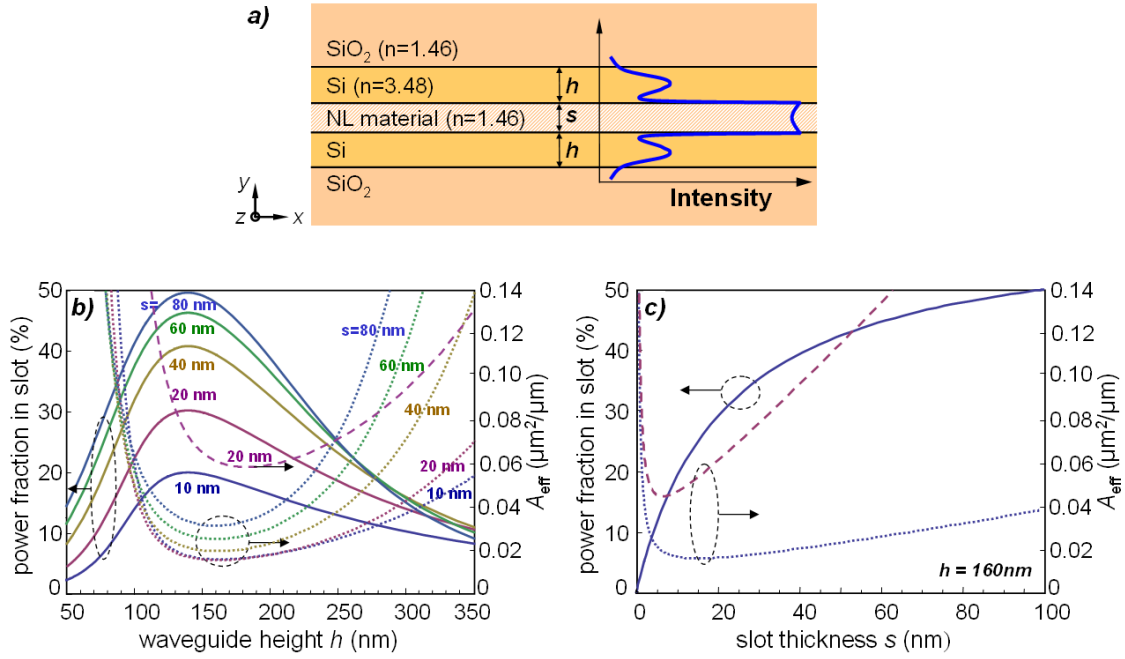


Figure 7.3.: a) Cross section of a horizontal slot waveguide slab system and intensity profile of the TM slot mode; b) optical power in the optically nonlinear slot region (solid lines) and effective area (dotted lines) as a function of the silicon layer thickness for different slot thicknesses, and c) as a function of the slot thickness at a constant silicon layer thickness close to the found optimum of $h = 160$ nm. The dashed lines in b) and c) represent the low index approximation as used in [18].

thickness h for different slot thicknesses s ranging from 10 to 80 nm. A silicon layer thickness of 160 nm provides maximum confinement and, thus, maximum nonlinear interaction irrespective of the slot thickness. It has to be pointed out that the optimum layer thickness h for maximum nonlinear interaction is almost identical to the layer thickness where maximum power confinement in the slot region is achieved. As a consequence, all results of the preceding chapters about modal behavior and lateral leakage, where the studies were restricted to waveguide thicknesses around this found optimum, still apply.

Figure 7.3 b) shows the power confinement in the slot region and the effective area as a function of the slot thickness at a constant silicon layer thickness of 160 nm. The plot reveals, that an absolute optimum for the nonlinear interaction can be achieved at small slot thicknesses. The maximum is obtained for slot thickness of $s = 15$ nm. The dashed lines in Fig. 7.3 b) and c) show the low index approximation used in [18] demonstrating the significant deviation of the absolute value of A_{eff} and the location of the minimum with respect to the height h and the slot thickness s .

Interestingly, the curvature in the vicinity of the optimized nonlinear interaction calculated with the low index approximation is noticeable higher compared to the exact formulation of (7.6).

Next, we studied the nonlinear behavior of vertical slot waveguide structures (see Fig. 7.2 a)) with respect to the strongly confined TE-like mode for different refractive indices of the nonlinear cover medium ranging from 1.5 to 1.8. Using the optimization procedure described above, we determined the minimum achievable effective area as a function of the slot thickness s (see Fig. 7.4 a)). Figure

7.4 d) plots the corresponding values of the optimized geometry parameters h and w .

The results for $s > 50$ nm match well with those reported by Koos *et al.* [20], who restricted their simulations to this practically relevant area. For the sake of comparison with the horizontal slot waveguide structure, we considered also smaller slot widths with $s < 50$ nm. The smallest effective areas are achieved at slot thicknesses around 20 nm, which is in good agreement with the result obtained for the slab system. The corresponding optimum geometry parameters are around 270 nm in vertical and 190 nm in lateral direction, where the height shows less dependence on the slot thickness compared to the width w . The width increases from 260 nm for a slot thickness of 10 nm to approximately 330 nm for a slot thickness of 100 nm.

Moreover, the refractive index in the slot region influences the effective area to a large amount. With increasing refractive index, the effective area is increased as well but shows almost no impact on the optimized geometry parameters. The optimized height differs by only ~ 10 nm over a slot range of 10 – 100 nm.

Figures 7.4 b) and e) show the minimum achievable effective areas and the corresponding optimum geometry parameters for the strongly confined TM-like modes in horizontal waveguide structures filled and covered with the nonlinear material (see Fig. 7.2 b)). The results are almost identical to that of vertical slot waveguides both in terms of minimum achievable effective areas and in terms of optimum geometry parameters. This is due to the fact that the refractive index profiles of the cladding surrounding the two silicon wires are very similar for these two configurations. For a nonlinear material with a refractive index of 1.46 the results would be identical. The only difference arises from the fact, that in the vertical configuration the nonlinear material covers both interfaces with the length w , whereas for the horizontal type one length with w borders the lower silica buffer layer, but on the other hand both length with the length h are exposed to the nonlinear material.

If we do not cover the horizontal slot waveguide structure with the nonlinear material and use air as cladding instead, the confinement of the light in the slot is improved due to the increased refractive index contrast between silicon and air. As the results on the minimum achievable effective area as a function of the slot thickness s plotted in Fig. 7.4 c) reveal, the additional nonlinear interaction due to the stronger confinement in the slot region outbalances the nonlinear interaction in the cladding region in the case of a structure covered with the nonlinear material. The higher the refractive index of the nonlinear material, the stronger this effect becomes in comparison to the slot waveguide structure covered with the nonlinear material. But still the smallest effective area is reached for the lowest refractive index in the slot region. The values of the optimized geometry parameters are plotted in Fig. 7.4 f). The optimum of the width w is decreased in contrast to the optimum height h which can be found at higher values compared to the slot waveguide structure with nonlinear material acting as slot and cover material. The optimum width can be found at 230 nm and the optimum height at 210 nm. The smallest effective areas range from $0.027 \mu\text{m}^2$ to $0.05 \mu\text{m}^2$ depending on the slot index and are obtained for slot thicknesses of around 15 to 25 nm with silicon wires of ~ 210 nm height and ~ 220 nm width.

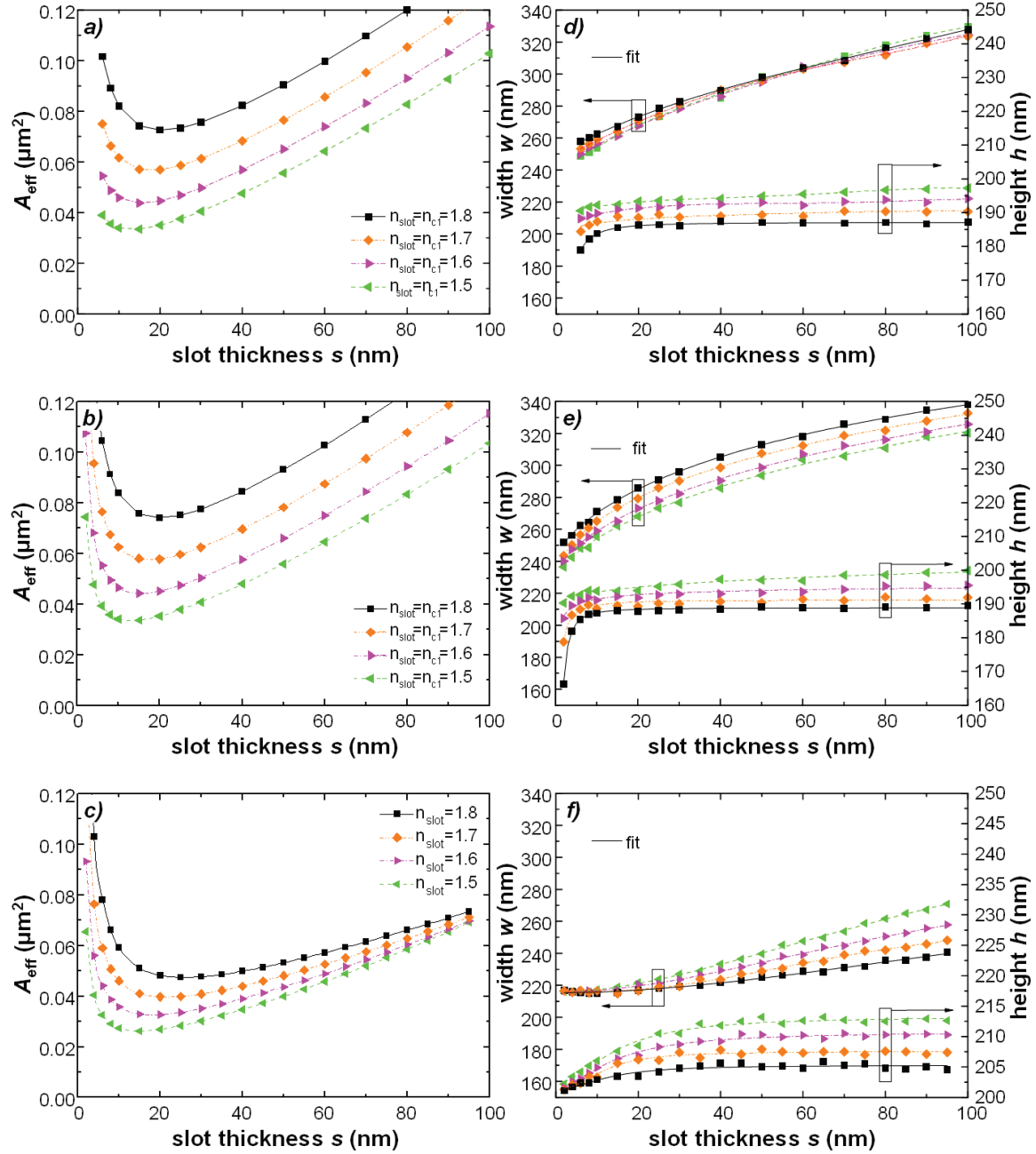


Figure 7.4.: Dependence of the minimum achievable effective area on the slot thickness s for different refractive indices of the nonlinear material in a) a vertical slot waveguide completely covered with the nonlinear material, b) a horizontal slot waveguide filled and covered with the nonlinear material, and c) a horizontal slot waveguide filled with the nonlinear material and covered with air. At each point, the geometry is optimized with respect to the parameters h and w such that a minimum effective area is obtained. The corresponding values of the optimized geometry parameters are plotted in d)-f). The results in a) and d) for slot thicknesses $s > 50$ nm match with those published in [20].

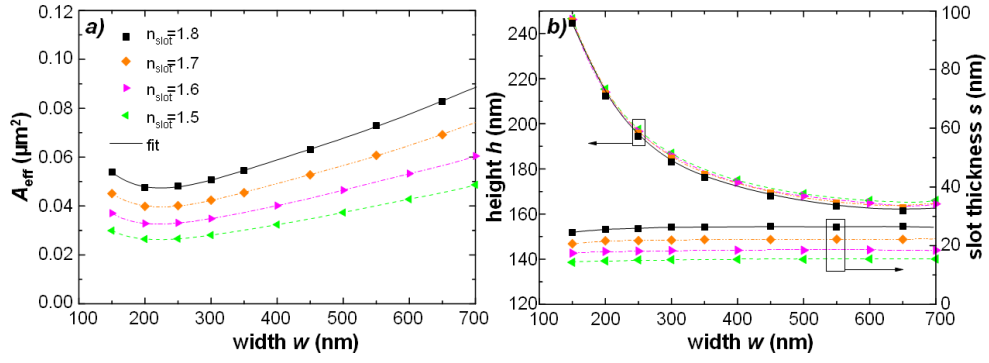


Figure 7.5.: a) Dependence of the minimum achievable effective area in a horizontal slot waveguide on the width w for different refractive indices of the nonlinear material filled in the slot region. The upper cladding is air. At each point, the geometry is optimized with respect to the waveguide height h and slot thickness s . The corresponding values of the optimized geometry parameters are plotted in b).

Finally, it was clarified how the width of an air-covered horizontal slot waveguide influences the nonlinear interaction. In order to answer this question, we used our optimization procedure with respect to the waveguide height h and slot thickness s to determine the minimum achievable effective area as a function of w .

The results plotted in Fig. 7.5 a) indicate that the waveguide width can be considerably increased to values of 400 to 500 nm without significantly sacrificing nonlinearity. This can help reducing scattering losses induced by rough waveguide side walls. The optimum slot thickness remains almost constant over the plotted range of w , while the optimum height decreases rapidly to a value of 160 nm (see Fig. 7.5(b)).

7.4. Conclusion

The eigenmode analysis of vertical and horizontal slot waveguide structures in this chapter provides the optimized set of geometry parameters for which a minimum effective area and, thus, maximum nonlinear interaction is achieved. The results indicate that air-covered horizontal slot waveguides facilitate the exploitation of nonlinear effects in nonlinear materials with a comparatively low refractive index because they allow for much thinner slot layers and thus smaller effective areas than vertical slot waveguides. Ultra-thin vertical slots not only represent a challenge in fabrication but would also be difficult to fill with nonlinear materials. In addition, air-covered vertical slot waveguides appear difficult to realize from a technological point of view, thus prohibiting higher light confinement and smaller effective areas. Horizontally sandwiched structures with very thin slot layers, on the other hand, can be fabricated by CVD methods [13, 17, 41, 74, 121, 122], which are also applicable to organic nonlinear materials [21]. Incorporating for example the highly nonlinear organic material PTS, which has a linear refractive index of $n_{\text{slot}}=1.7$ and a nonlinear refractive index of $n_2=2.2 \times 10^{-16} \text{ m}^2\text{W}^{-1}$ [20], in an optimized horizontal slot waveguide structure will give a nonlinearity coefficient $\gamma=n_2 k_0 / A_{\text{eff}}$ of $>20 \text{ W}^{-1}\text{mm}^{-1}$, where we assumed an $A_{\text{eff}} = 0.04 \mu\text{m}^2$ based on the results in Fig. 7.4 c).

8. The V-groove structure

Finally, a novel photonic waveguide structure is introduced: The V-groove waveguide. As presented for the first time in [85] the V-shaped groove features a significant slot effect, while at the same time the accessibility of the slot region is improved compared to the vertical slot waveguide. The structure is numerically studied with respect to three interesting applications: Evanescent wave sensing, support of nonlinear interaction and lasing.

8.1. Introduction

Irrespective whether the horizontal or vertical slot waveguide concept is considered, both approaches have some intrinsic drawbacks with regard to the accessibility of the narrow slot region. One major result of chapter 7 is that for the effective exploitation of nonlinear effects a narrow slot thickness of the order of 30 nm is advantageous. Filling such a narrow slot with a nonlinear material or a gain medium is a challenging task. The same holds true when using the slot region as sensitive interaction region into which a sensitive medium and an analyte have to be introduced. Also for such linear applications a narrow slot thickness is beneficial as the results in [34] show.

In order to overcome this limitation, in this thesis the so-called V-groove waveguide (see Fig 8.1)

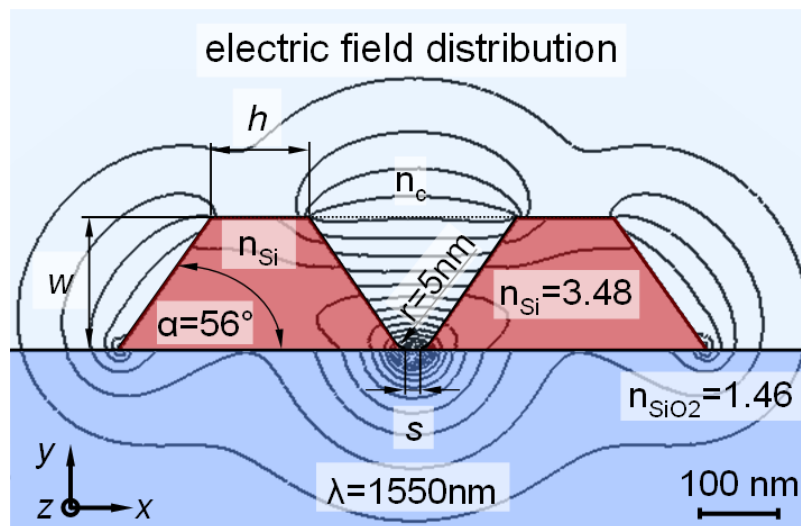


Figure 8.1.: Cross section of a V-groove waveguide. In a waveguide consisting of two wires with isosceles-trapezoidal cross section, quasi-TE polarized light is strongly concentrated near the bottom as indicated by the contour plot representing the electric field profile.

will be discussed in detail, as proposed in [85]. First studies taking angled side walls of the slot into account have been presented in [83, 84]. However, in a waveguide consisting of two silicon wires with isosceles-trapezoidal cross section which are placed close together, the light is strongly concentrated near the bottom of the structure. This effect is caused by the combination of increased waveguide at decreased slot thickness with towards the bottom of the structure. Figure 8.1 shows the electric field profil of the quasi-TE polarized eigenmode as contour plot for a typical structure consisting of two wires with a height w of 150 nm, a width h of 100 nm and a separation s of 10 nm. The parameters w and h are defined accordingly in order to stay consistent with the preceding chapters. It has to be noted that the separation is defined as distance in the flat region of the groove. The two radii are not included.

The underlying effect is comparable to the slot effect, though it offers the advantage of eased accessibility of the slot region compared to other slot based concepts. Such structures can be obtained by anisotropic etching of a silicon wire with KOH oriented in the $\langle 110 \rangle$ direction, which results in a side wall angle of $\alpha = 56^\circ$.

The technological feasibility of such silicon nanostructures has already been demonstrated in the context of nanoelectronic devices [95–97] (see section 8.5 for details). In the following, simulations are carried out on V-groove waveguide geometries shown in Fig. 8.1 in order to investigate the suitability of the structure for three major applications: Surface sensitive sensing, exploitation of nonlinear effects in low index materials and to lasing introducing quantum dots as gain material. These three applications cover the major characteristics of the structure. As depicted in Fig 8.1 the simulation model includes a radius of 5 nm at the bottom of the groove which takes into account technological imperfections and ensures that the slot like effect is comparable to a realized structure. At the outside of the two isosceles-trapezoidal shaped cores no radius was assumed due to the low field concentration observed at these interfaces.

8.2. Optimization for surface sensing

8.2.1. Fundamentals

Realtime label-free detection of biomolecules is a promising field of application for optical waveguide devices. For a waveguide thickness below the wavelength, the propagation constant is noticeably influenced by the surrounding media due to the evanescent field [123]. This fact can be exploited for biochemical sensing by functionalizing the waveguide surface with a biosensitive layer that specifically captures one particular molecule species. When the solution containing the analyte is introduced to the sensor surface only complementary molecules are bound. These binding events change the effective index of the structure, which can be detected in a highly sensitive way by employing interferometric configurations such as planar integrated Mach-Zehnder interferometers (MZI) [124–128]. So far, rib- and wire-type waveguides have been used for the realization of such surface sensitive devices.

Due to its unique feature of concentrating light in low index material vertical slot waveguides have also been considered as promising sensitive waveguide structure. A theoretical study [28] de-

terminated the sensitivity under the assumption that the surface functionalization is applied selectively to the top and the bottom horizontal interfaces of a vertical slot waveguide but not to the vertical side walls. The results indicated that in this case the surface sensitivity is comparable to SOI wires. However, the assumption that the side walls are not functionalized does not take into account the advantage of the unique features of the slot effect. In [34] it was assumed, that the inside surfaces of a vertical slot waveguide is functionalized with a biosensitive layers resulting in much higher values of sensitivity compared to [28]. On the other hand as mentioned before, the high concentration of the light inside the slot only becomes effective for narrow slots of <100 nm thickness. This makes the access of the biosensitive material difficult, which is usually deposited in a liquid phase, as well as for the biomolecules in the analyte which must be able to enter the slot region. Recently, less sensitive silicon nitride slot waveguides with $w = 300$ nm and a slot thickness of $s = 200$ nm were used for homogeneous measurements with liquids of different refractive indices and surface sensitive experiments [29, 30, 32–34, 54]. The results of this experimental study suggested that the slot region can be filled only partially due to the poor accessibility of the slot region. For an extremely high sensitive SOI slot waveguide this problem intensifies due to the significantly narrower slot width. Therefore, with respect to the ease of surface coverage with the biofunctionalization layer and of the penetration of the analyte into the region where the light interaction becomes effective, the V-groove structure with its strongly angled side walls provides a much better environment than the vertical slot waveguide. In the following it was assumed that the V-groove structure is covered with a thin sensitive layer of the thickness $t_0=10$ nm and the typical refractive index $n_{f0}=1.5$ of an organic materials (as shown in Fig. 8.2).

In order to quantify the sensitivity, we employ the sensitivity parameter [129]

$$S = \frac{\partial n_{\text{eff}}}{\partial \eta}, \quad (8.1)$$

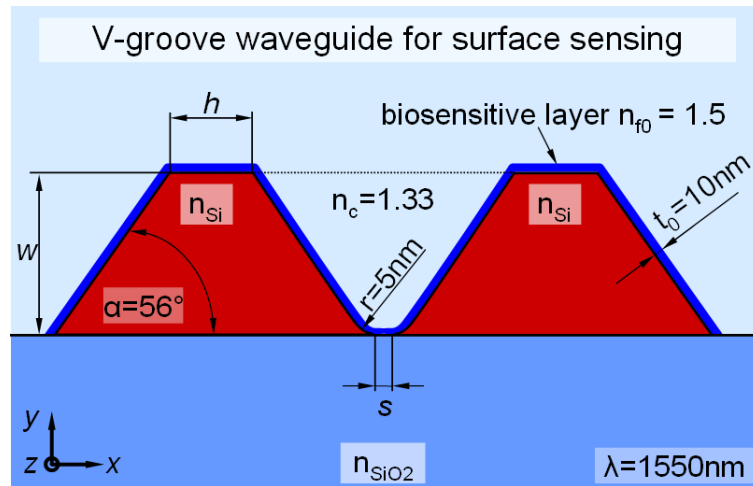


Figure 8.2.: Simulation model for the optimization of the surface sensitivity. Two wires with the height h and the top width w and $\alpha = 56^\circ$ angled side walls are separated by s . The entire waveguide is coated with a sensitive film of the thickness $t_0=10$ nm and the refractive index $n_{f0}=1.5$. At the bottom the inner side walls have a radius of 5 nm.

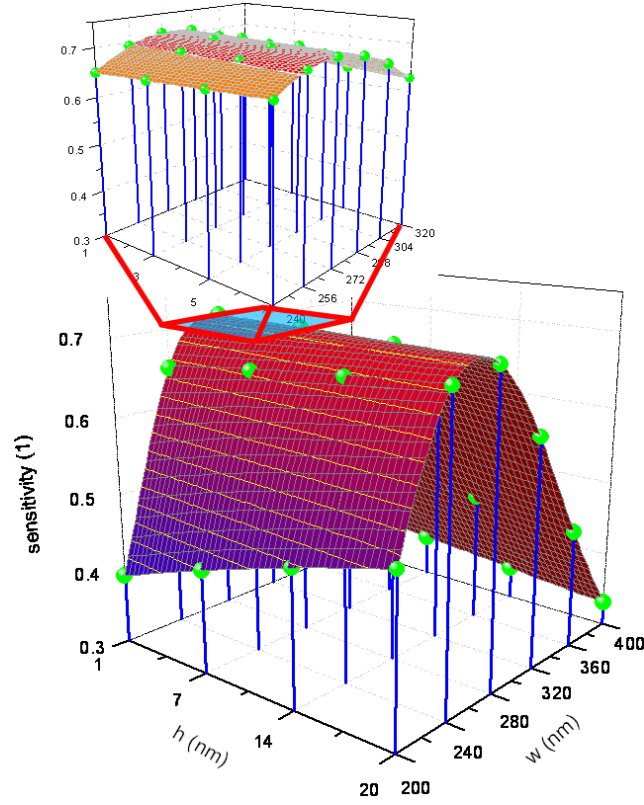


Figure 8.3.: Simulation procedure in order to determine the optimized structure with ensuring maximum surface sensitivity. At first, a course grid of w - and h -values was generated and simulations with these parameters were performed. The parameter set that provided maximum sensitivity was then used as starting point for a further optimization with a refined grid in a narrower parameter range.

where $\eta = k_0 t (n_f^2 - n_c^2)$ the so-called dielectric load term. The refractive index n_c of the aqueous solution acting as upper cladding is set 1.33. The sensitivity S is normalized to the wavelength, the film thickness, and the difference of the squared refractive indices $n_f^2 - n_c^2$. This general definition of the sensitivity can be rewritten in two ways depending whether the effective index change is induced by a refractive index change

$$S_n = (2k_0 t n_f)^{-1} \left. \frac{\partial n_{\text{eff}}}{\partial n_f} \right|_{n_{f0}} \approx (2k_0 t n_f)^{-1} \left. \frac{\Delta n_{\text{eff}}}{\Delta n_f} \right|_{n_{f0}}, \quad (8.2)$$

or by a thickness change of the sensitive layer

$$S_t = [k_0 (n_{f0}^2 - n_c^2)]^{-1} \left. \frac{\partial n_{\text{eff}}}{\partial t} \right|_{t_0} \approx [k_0 (n_{f0}^2 - n_c^2)]^{-1} \left. \frac{\Delta n_{\text{eff}}}{\Delta t} \right|_{t_0}. \quad (8.3)$$

8.2.2. Simulation technique

The goal of these investigations was to find the geometry providing maximum surface sensitivity as defined in the preceeding section. For this purpose, the dependence of the sensitivity on the

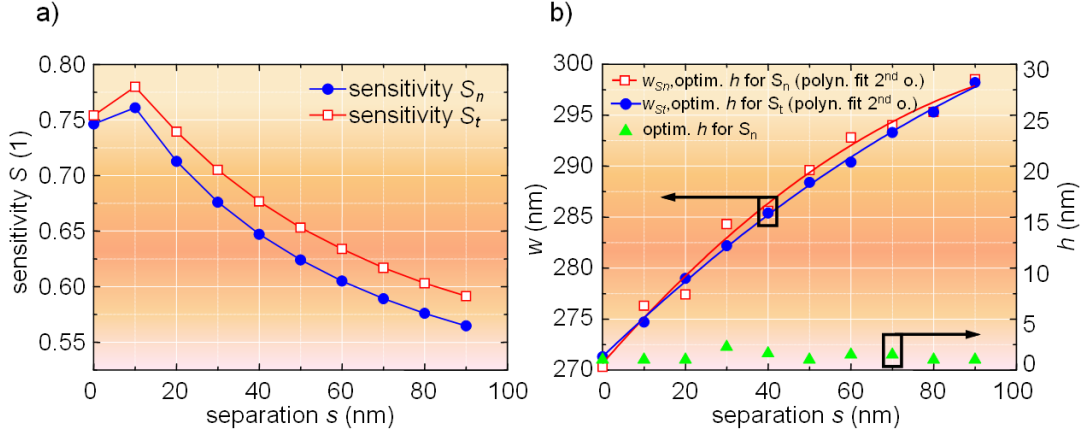


Figure 8.4.: a) Maximum sensitivities S_n and S_t as a function of the separation s for geometries optimized with respect to w and h ; b) corresponding values of w and h .

separation s for optimized width and height was studied. In order to determine the optimized height and width for a given separation, at first, a course grid of w - and h -values comprising the optimized geometry was generated and simulations with these parameters were performed. The parameter set that provided maximum sensitivity was then used as starting point for a further optimization with a refined grid in a narrower parameter range (see Fig 8.3). This process was repeated iteratively until the step size of both width and height was less than 1 nm and the difference in the calculated sensitivity of two consecutive iterations was smaller than 10^{-3} . In addition, an adaptive mesh refinement was employed to ensure sufficient accuracy at the sensitive maximum. The optimized mesh typically consisted of 300.000 elements. This ensures, that all dielectric corners and radii are resolved sufficiently.

8.2.3. Results of optimization

Figure 8.4 a) shows the surface sensitivity of the structure as a function of the separation. The sensitivity has its maximum at a separation of ~ 10 nm. For higher separations, the sensitivity approaches the value of independent wires. The difference between the sensitivity S_n and S_t indicates that the change of the refractive index of the sensitive layer is not completely equivalent to the change of its thickness. The values of the optimized geometry parameters w and h are shown in Fig. 8.4 b). The optimized w increases slightly from $w=272$ nm for $s=0$ nm to $w=297$ nm for $s=90$ nm. This is consistent with the behavior of standard slot waveguide structures. A comparison with Fig. 5.1 a) reveals that a standard slot waveguide with a width of 400 nm shows an increased optimized height with increased slot thickness s which is of the same order as observed for the V-groove waveguide. The difference between the optimum heights calculated with respect to S_n and S_t are negligible. The higher variation of w_{S_t} can be explained by the varying finite element mesh for two thicknesses t of the film compared to the calculations of w_{S_n} , which can be performed with the same mesh. This indicates the limit of accuracy of these simulations. The optimum width h , on the other hand, approaches zero for all values of s , which results in an optimized structure with two

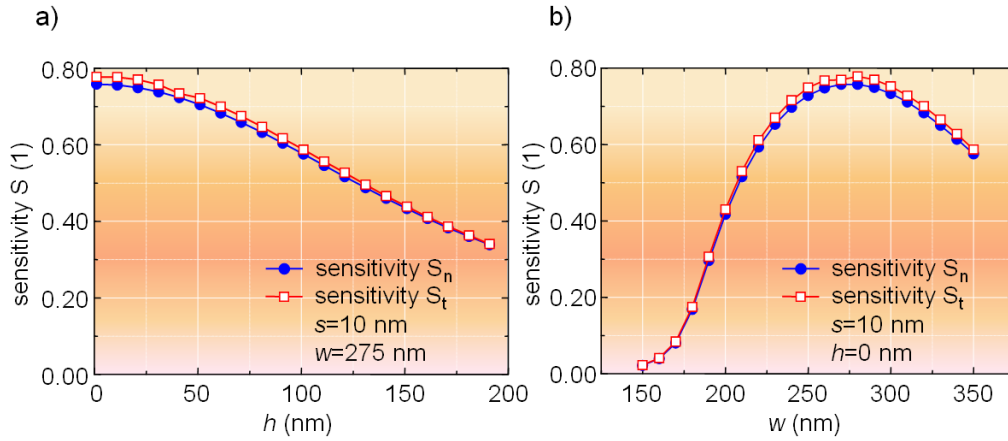


Figure 8.5.: Dependence of the sensitivities S_n and S_t on a) h and b) w . The remaining geometry parameters are kept constant at the optimized values given in Fig. 8.4.

triangular shaped cores.

In practice, the geometry will vary from the design values due to deviations in the fabrication process in particular for this thoroughly challenging structure in terms of realization. Therefore, the dependence of the sensitivity under variation of the width or height is of particular interest. In Fig. 8.5 a) the sensitivity is plotted for the optimized w in dependence of the h , whereas Fig. 8.5 b) shows the characteristic of the sensitivity under variation of w . Compared to the impact of the separation, the influence of h and w is small near the optimum. The sensitivity is approximately halved by increasing h from zero to $h = 150$ nm. The height of the waveguide can vary from $w = 200$ nm to more than $w = 350$ nm without reducing the sensitivity to less than 50%. This demonstrates the quite fabrication tolerant characteristic of the structure. Certainly the most interesting issue is a comparison of the sensitivity values with other highly sensitive waveguides. Table 8.1 summarizes typical surface sensitivities of different silicon photonic structures. The sensitivity of the rib was approximated analytically using a four layer slab waveguide for an optimized geometry with a height of $h=55$ nm. The sensitivity of the wire was calculated for the geometry parameters of [126]. The value in the brackets is the theoretical limit for a TE-operated wire with infinite height corresponding to the most sensitive wire based structure. The sensitivity of the vertical slot waveguide was calculated for a typical geometry with a slot width of 70 nm, a height of 300 nm, and optimized wire width with a biosensitive layer of 10 nm thickness applied to all interfaces of the two wires. Although the optimized sensitivity of the vertical slot waveguide is twice as large as that of the

Table 8.1.: Comparison of the surface sensitivity of different silicon photonic structures.

	SOI rib (TE)	SOI wire (TM) [126]	vertical SOI slot (TE)	SOI V-groove (TE)
S_t	0.22	0.41 (0.67 TE)	1.6 TE	0.78

V-groove structure it is more of theoretical relevance because of the afore mentioned problems regarding the filling of the narrow slot region. But compared to standard waveguides such as ribs and wires, the V-groove shows its potential. The sensitivity is more than three times higher compared to an optimized rib waveguide, and still exceeds the value of the most sensitive wire based structure. Moreover, the latter is only a theoretical value which hardly can be approached in practice. Thus, the V-groove waveguide represents a highly attractive structure for surface sensing.

8.3. Optimization for nonlinear effects

8.3.1. Fundamentals

Due to their unique light confining characteristics slot waveguides are of particular interest for the efficient exploitation of third order nonlinear optical effects in low index materials as explained in chapter 7. But as shown in chapter 7, the full potential of the slot waveguide structure can only be exploited for geometries with very low slot thicknesses regardless whether the configuration is vertical or horizontal.

While the horizontal slot waveguide [24, 25] provides a better confinement in the nonlinear material than the vertical type, it requires a nonlinear material that can be deposited with thicknesses of ~ 10 nm to ~ 50 nm and that is compatible with the deposition process of a second silicon layer. The vertical slot waveguide structure, on the other hand, suffers from the difficulty of filling a narrow slot of ~ 50 nm width and ~ 400 nm height with a nonlinear material. Therefore, the V-groove waveguide could offer a good compromise between these two options. In order to study the V-groove structure in this context, the model shown in Fig. 8.6 was used, where the nonlinear material with the typical refractive index of $n_c=1.7$ for practical reasons covers the entire waveguiding structure. Again, for determining how well the waveguide structure supports the nonlinear interaction in the nonlinear material the effective area A_{eff} was calculated using (7.6).

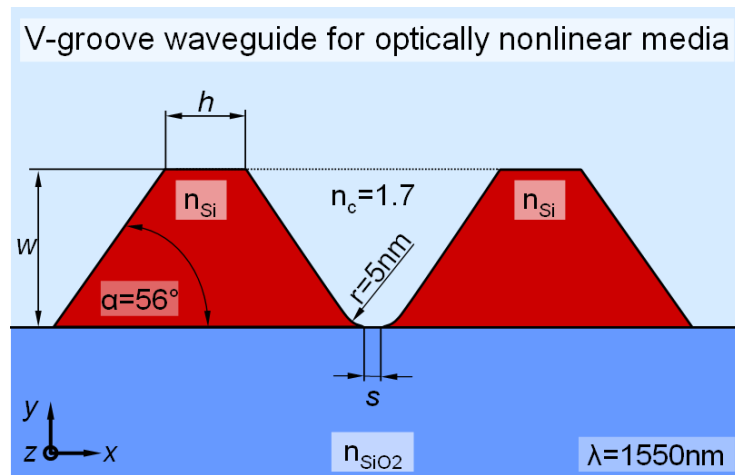


Figure 8.6.: Simulation model for the optimization of the effective area A_{eff} in a V-groove waveguide structure covered with a nonlinear medium of the refractive index $n_c=1.7$.

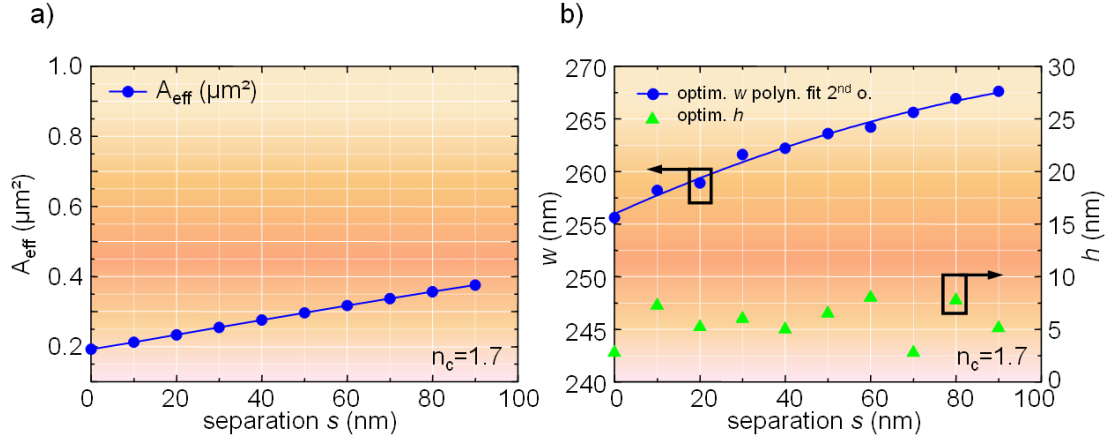


Figure 8.7.: a) Minimum effective area A_{eff} for optimized geometry parameters w and h in dependence on the separation s , and b) the corresponding values of w and h .

8.3.2. Simulation results

In order to determine the V-groove geometry that provides maximum nonlinear interaction in a nonlinear material with a refractive index of $n_c = 1.7$, we used the same optimization procedure as described in section 8.2.2. This time the algorithm was adapted in order to find the minimum of the effective area with respect to the geometry parameters h and w for different values of separation s . Similar to the surface sensitivity, the separation s has a strong influence on the effective area. In fact, the impact of the separation is noticeably stronger compared to the surface sensitivity. An increase of the separation from 0 nm to 100 nm more than doubles the effective area. Again, the optimum is at $s = 0$ as Fig. 8.7 a) reveals. The corresponding optimized height h shown in Fig. 8.7 b) is about 20 nm lower than h_{S_n} and h_{S_t} found in the previous section for the surface sensitivity. The width w for minimum A_{eff} is close to zero. In practice, the optimum geometry again consists of two triangularly shaped wires. Compared to the structure optimized with respect to the

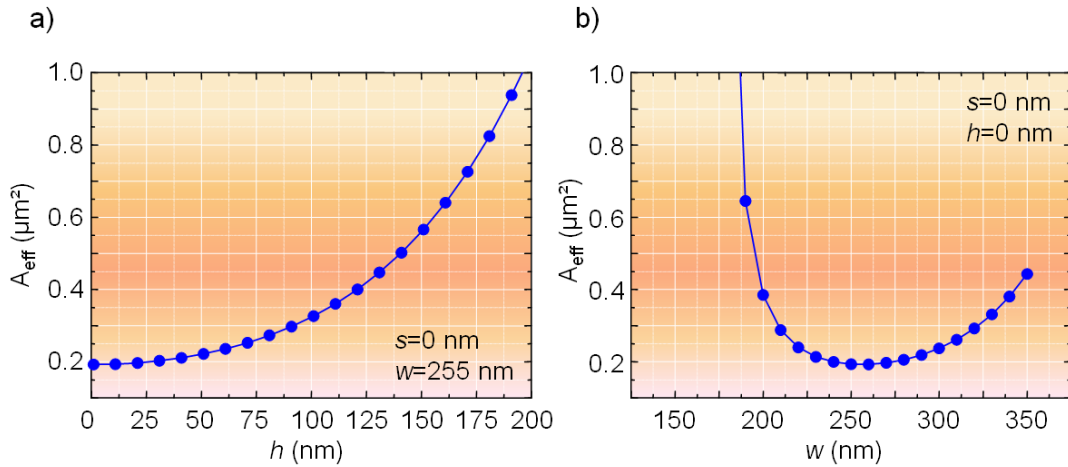



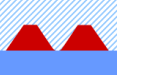


Figure 8.8.: Dependence of the effective area A_{eff} on a) the h and b) the w . The remaining geometry parameters are kept constant at the optimized values given from Fig. 8.7.

Table 8.2.: Comparison of the effective area of different silicon photonic nanostructures. The shaded areas indicate the optically nonlinear medium.

	wire (TM) [20]	vert. slot (TE) [20]	horiz. slot (TM) [24]	V-groove (TE)
				
$A_{\text{eff}} (\mu\text{m}^2)$	0.33	0.1	0.045	0.19

sensitivity, the dependence of the effective area on the height and width (see Fig. 8.8) is stronger. In particular, this holds true for the dependence of the effective area on w corresponding to the thickness of the monocrystalline silicon layer as plotted in Fig. 8.8 b). For w significantly below 200 nm the effective area increases by orders of magnitudes. On the other hand, an increase of h from the optimum of $h = 0$ nm to $h = 100$ nm approximately only doubles the effective area. Higher deviations should be avoided due to the increased gradient for $h \gg 100$ nm. Bearing the possibilities of thin film technologies in mind, where the realization of layers within an accuracy of a view tens of nanometers over a whole wafer is standard, from the practical point of view the crucial geometry parameter is still the separation.

Table 8.2 provides a comparison between minimum achievable effective areas of different SOI structures employing a nonlinear medium with a refractive index of $n_c = 1.7$. Except for the horizontal slot waveguide the nonlinear medium covers the whole structure. In the case of the horizontal slot waveguide structure the nonlinear material is limited to the slot region and the upper cladding is assumed to be air [24, 25], which provides the minimum A_{eff} for this structure in general. The effective area of the V-groove waveguide versus the effective area of a standard wire waveguide is only 57% which is a significant increase. In comparison to the slot waveguide structures, the V-groove waveguide provides a two to four times larger effective area. Nevertheless, considering the advantages offered by the V-groove shape this structure can be an attractive alternative to slot waveguides.

8.4. Application to lasing

8.4.1. Fundamentals

Monolithically integrated silicon based lasers and amplifiers are highly desired photonic components. Much research effort is dedicated to this topic in order to overcome inherent problems of silicon such as the high two photon absorption. The V-groove waveguide structure represents an attractive platform for the realization of such devices. It facilitates the self-assembly of gain media such as nanocrystals or quantum wires, which cannot act as waveguides on their own, at the bottom of the V-groove, *i.e.*, at the location where the light of the guided mode is strongly concentrated. Here, the characteristic of the V-groove waveguide — the very low mode volume in two directions, not only in one as supported by standard slot waveguides — is fully exploited. As an example, we

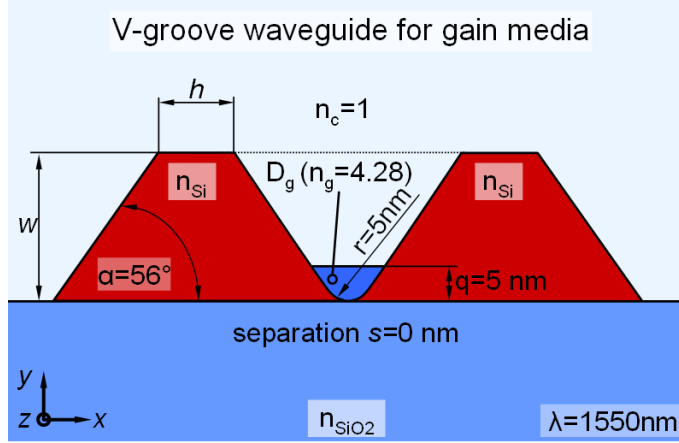


Figure 8.9.: Simulation model of a V-groove waveguide structure for optimization of the gain parameter where between the two cores an gain medium such as a germanium wire ($n_g=4.28$) is placed. We assume a homogeneous filled V-groove of 5 nm height q .

chose a model as sketched in Fig. 8.9, where a germanium quantum wire is located at the bottom of the groove. In a first approximation we assumed a homogeneous filling area of $q=5$ nm height with a refractive index for germanium of $n_g=4.28$ at a wavelength of $\lambda=1550$ nm. In this particular configuration the silicon V-groove with its lower refractive index of $n_{Si}=3.48$ can be seen as supporting structure to ensure guidance of the light in the area of the quantum wire.

As the gain related figure of merit we choose the parameter γ_A which was derived for ultra high index waveguides recently for the first time in [130]

$$\gamma_A = \frac{\epsilon_g \int_{D_g} |\vec{\mathcal{E}}|^2 dx dy}{\int \int_{D_{Tot}} \epsilon(x,y) |\vec{\mathcal{E}}|^2 dx dy}, \quad (8.4)$$

where $\epsilon(x,y)$ is the permittivity distribution of the waveguide structure, ϵ_g the permittivity of the optical gain medium, D_g the area with the optical gain medium, D_{Tot} the entire simulation domain, and $\vec{\mathcal{E}}$ the electric field of the quasi-TE polarized eigenmode. The gain parameter γ_A allows the optimization of structures with respect to a low lasing threshold.

8.4.2. Simulation results

In analogy to the previous sections, we used the same procedure to obtain the V-groove geometry for the maximum gain γ_A (evaluating the simulation results with equation (8.4)), which corresponds to the minimum possible lasing threshold. In contrast to the optimization with respect to surface sensitivity and nonlinearity, the separation s is set to zero due to the limited cross section of the assumed germanium wire. From the optimization with respect to the other applications examples, where the optimum structure was always close to a separation of $s = 0$ nm, it can be assumed, that this is not a disadvantage.

The dependence of the gain on h as shown is Figure 8.10 a) for this figure of merit is not monotonically. Contrary to the other studied applications, the optimized height deviates from $w =$

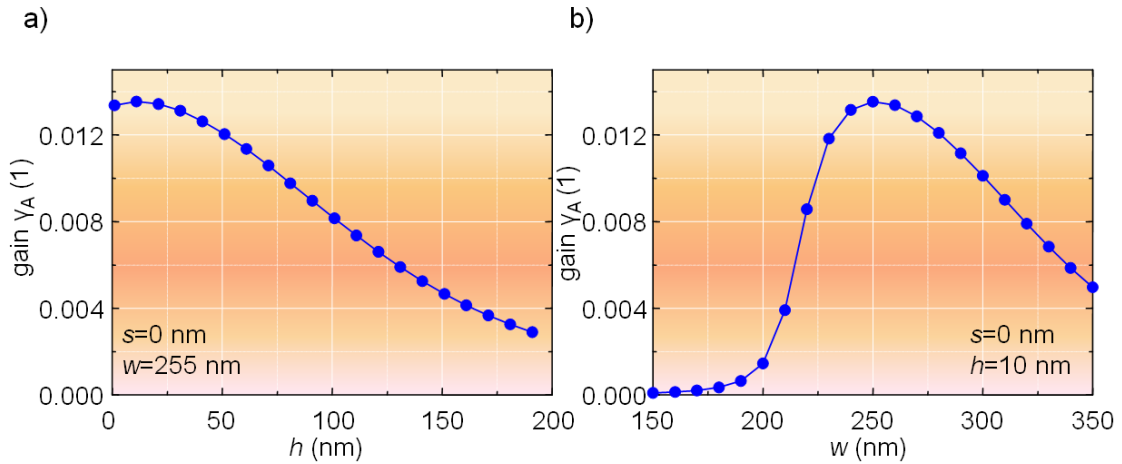


Figure 8.10.: a) Dependence of the gain parameter γ_A on h . In b) the influence of w is shown. The corresponding simulation were carried out for a constant separation $s = 0$ nm and an optimized parameter a) $h = 10$ nm and b) $w = 255$ nm..

0 nm. This can be attributed to the higher index contrast between silicon and the surrounding air, which shifts the optimized value to $h = 10$ nm. The decrease of the gain for a w larger than the optimized value is comparable to the behavior as observed for the surface sensing. The dependence of γ_A on the height h and width w was calculated. It turns out, that the optimized parameters are $w = 10$ nm and $h = 250$ nm. Figure 8.10 b) plots the dependence on w . The gain decreases rapidly for w below the maximum value and approaches zero for $w = 150$ nm. For values of w exceeding the maximum, the decrease is weaker and for a layer thickness of $w = 350$ nm the gain γ_A is about 30% of the maximum value. Overall, the behavior of the gain is very similar to the inverse characteristic of the V-groove waveguide optimized with respect to nonlinear applications. Taking into account the similarity of equation (7.6) and (8.4) this comes not unexpected.

8.5. Feasibility

All these characteristics are certainly only of interest if such a V-groove waveguide with optimized parameters is technologically feasible. As mentioned at the beginning of this chapter, ensuring an orientation of the wires in the $\langle 110 \rangle$ direction, KOH etching automatically results in a side wall angle of 56 degrees. This is a well established process for structures in the micrometer range but it can also be applied to structures in the nanometer range as Fig. 8.11 shows. In Fig. 8.11 a) a trapezoidal shaped wire is shown where the bottom width of the wire is only about 200 nm [96, 97]. Even V-grooves of desired shape have been demonstrated in the context of electronic devices [95] as Fig. 8.11 b illustrates. However, wires with lengths of several millimeters up to centimeters are still a challenging task. Furthermore, it has to be pointed out that the orientation in the $\langle 110 \rangle$ direction has to be ensured. This restricts the waveguide design at first to - more or less - straight wires. Nevertheless, by employing etch simulation software [131] also more complicated structures can be imagined once the etch process of simple structures is established.

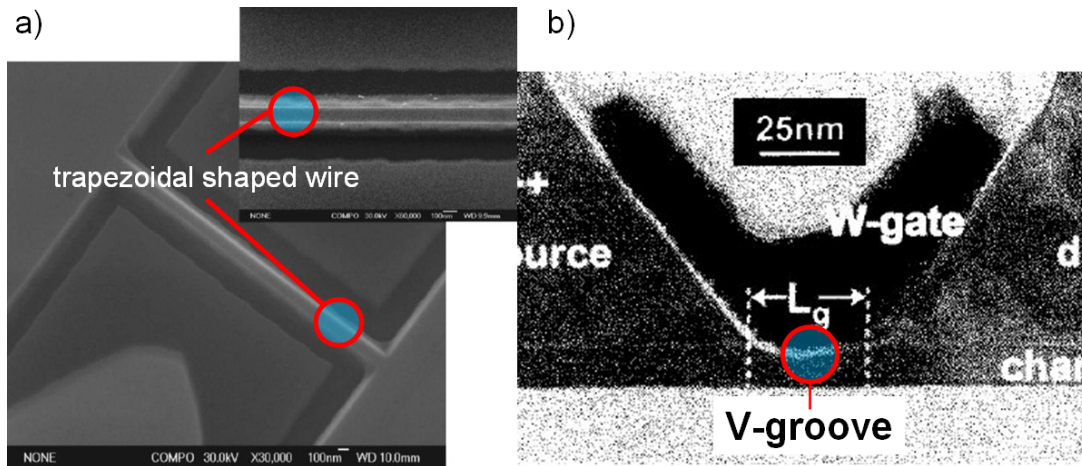


Figure 8.11.: a) Experimental realized trapezoidal shaped wire with a bottom width of 200 nm [96, 97]. b) V-groove realized in the context of an nanoelectronic device with a bottom width of the groove of 25 nm [95].

8.6. Conclusion

The suitability of the V-groove waveguide structure for surface sensing and for the exploitation of nonlinear optical effects in low index materials was studied. With respect to surface sensing, the highly angled side walls of the two wires facilitate the coating of the waveguide interfaces with a thin sensitive layer and offer a better access of the analyte to the sensitive region. This makes V-groove waveguides a promising candidate for exploiting the slot effect for surface sensing applications. The results of our numerical in-depth studies indicate, that a corresponding device offers a significant higher sensitivity compared to rib and wire type waveguides used so far.

With respect to the exploitation of nonlinear optical effects in low index materials, the V-groove waveguide structure could also allow overcoming practical limitations related to the filling of narrow slots of slot waveguides with a nonlinear medium, while providing a smaller effective area than optimized wire waveguides.

One major advantage of the V-groove waveguide is the confinement of the light in two directions resulting in a very small mode volume. Nanodots or nanowires could exploit this property in a very efficient way. A new approach for the realization of a silicon based laser could be the consequence. The realization of V-groove structures with optimized geometry parameters appears feasible. Similar silicon nanostructures have already been fabricated in the field of electronics by anisotropic etching with KOH. In terms of fabrication, the crucial parameter is the separation, which should be ensured within 20 nm. For the layer thickness w a deviation of about ± 20 nm is acceptable with respect to the optimized values, which is possible assuming the accuracy of typical SOI wafers. The upper width of the cores h is with ± 30 nm less critical in principle. Bearing in mind that this geometry parameter is a result of an etch step, achieving this accuracy could be a challenging task as well.

9. Summary

The first chapter of this work was dedicated to the origins of the slot effect. With the use of common methods such as Taylor series expansion and rarely used procedures like the Lagrange series it was possible to develop approximations where the most fundamental but at the same time most important characteristics of slot waveguides could be derived directly from Maxwell's equations. The Lagrange series enabled a transformation of the transcendent effective index equation into an approximation allowing for qualitative statements just by investigation of its analytic properties.

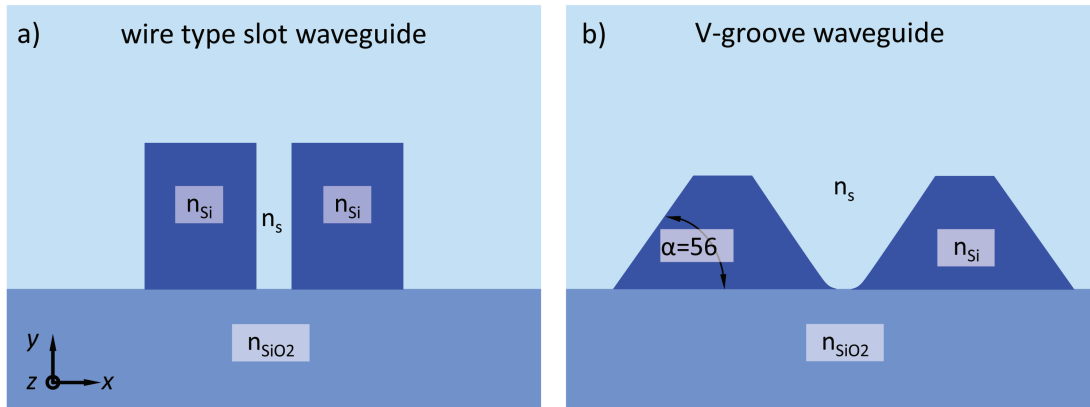
By comparing the solution of the numerical correct formulation of the effective index equation with the results of standard wire waveguides it was found that an optimized value with respect to the waveguide thickness h exists where the slot effect shows maximum impact on the effective index. Later, equations for the confined light power were developed and, as the studies revealed, again an optimized waveguide thickness exists where the slot waveguide provides maximum light intensity in the slot region. Moreover, by taking the optical power distribution of a wire waveguide with comparable geometry into account the unique power distribution of the slot waveguide was reasoned.

Next, an analytic approximation enabling the qualitative analysis of the characteristic of the confined power in the slot region was derived. Furthermore, the investigation of the slab slot waveguide was completed by the study of the modal behavior. The complex eigenmode spectrum was explained and in order to analyze higher order lateral modes as well as radiating modes, two different simulation methods were introduced. Fundamental characteristics of the modes were described resulting in a single mode criterion for a typically used slot waveguide structure.

The main part of this thesis was dedicated to the in-depth study on important aspects of different types of slot waveguides. Six different types were analyzed. The major aspect of all studies was the investigation of the characteristics of these slot waveguide types with regard to the realization of these structures in practice. Therefore, much computational effort was spend in order to take deviations in the fabrication processes into account in order to indentify which types of slot waveguides (introduced in section 2.4) can be used in practice.

For the sake of simplicity, the picture of the different types Fig. 2.12 is repeated here (see Fig. 9.1 on next page):

I. Vertical slot waveguides



II. Horizontal slot waveguides

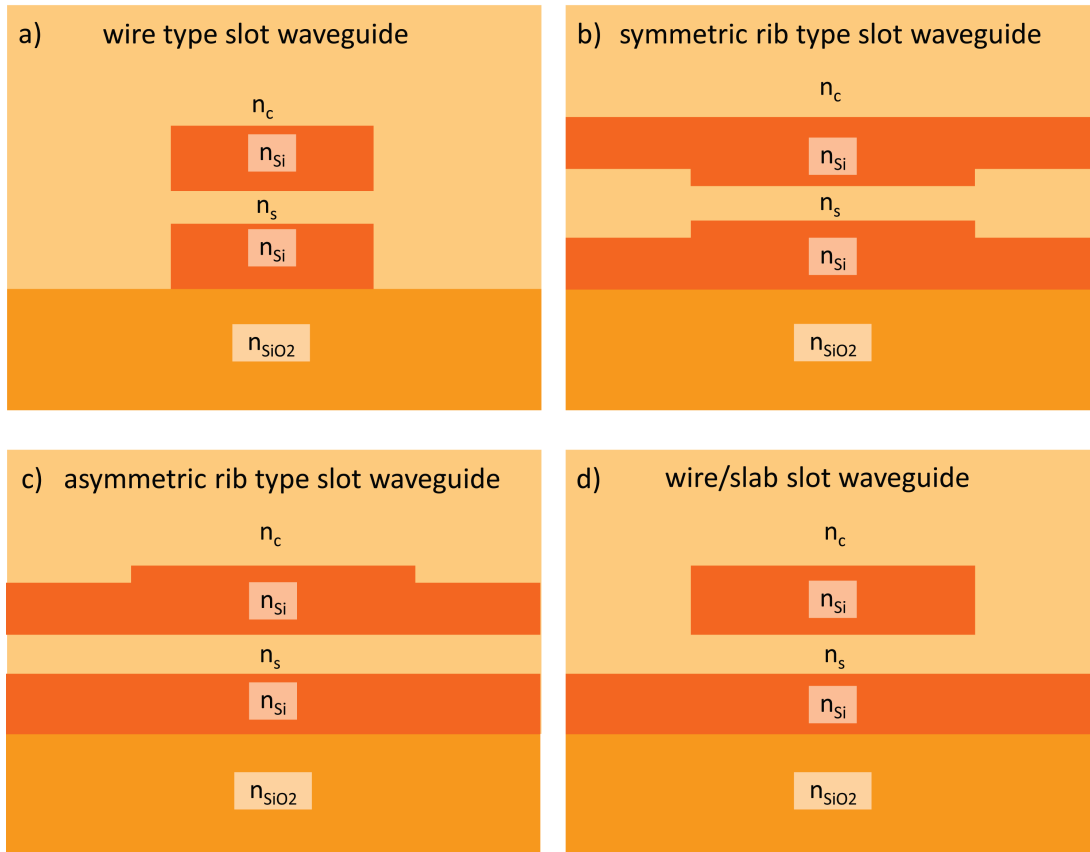


Figure 9.1.: Types of slot waveguides investigated and evaluated in context of this thesis.

I. Vertical slot waveguides

The vertical slot waveguide is the standard within the slot waveguide configurations. It was the first practical implemented slot structure [5] with the major advantage that it can be realized only by means of a single monocrystalline silicon layer as a prerequisite. Moreover, any material which ensures an entire filling of the slot region can be used as low index material.

a) Wire based

However, the results of two chapters of this thesis showed, that in the vertical approach (see Fig. 9.1 I. a)) it is not possible to exploit the full potential of the slot effect in practice. As pointed out in chapter 5 in order to obtain maximum power in the slot region of $< 50\%$ a w/h ratio of more than 4:1 is needed. The realization of such a height ratio would be a very challenging task.

For the exploitation of nonlinear optical effects in addition two restrictions of the vertical approach must be taken into account as the results of chapter 7 demonstrate. An optimized slot waveguide structure for the efficient exploitation of nonlinear optical effects in low index media has a slot thickness of tens of nanometers. Such a small slot thickness can hardly be realized with e-beam lithography which is necessary in order to fabricate a vertical slot waveguide. In addition, the ultimate low effective area ensuring maximum nonlinear interaction can only be achieved for a structure where the confinement is increased by air which surrounds the slot waveguide. But this necessitates a slot material which can be deposited in the slot region only and this is not possible in the vertical concept where the slot waveguide is filled and entirely covered by the slot material.

b) The V-groove waveguide

A new kind of slot waveguide is the so called V-groove waveguide proposed in [85] (see 9.1 I. b)). The acute angle in the center of the structure leads to a strong confinement at the bottom of the waveguide. An additional advantage arises from increased width on top of the slot compared to a vertical slot structure of Fig. 9.1 I. a). This could ease the problems of filling a narrow slot of the order of tens of nanometers.

As the studies exposed in chapter 8 demonstrated, the structure has a good applicability for surface sensitive sensors and nonlinear devices. Although the discussed figure of merits are lower compared to the optimized horizontal slot waveguide type they still exceed significantly the values of standard SOI waveguide types as wires and ribs. Furthermore, the good accessibility of the slot region makes the V-groove to an interesting alternative to slot waveguides as well.

High potential can be attributed to applications where an ultra small mode volume in two directions is necessary such as for quantum wires and dots. For these types of slot material, the V-groove waveguide could be a very effective host structure enabling ultra strong confinement at — maybe — moderate fabrication effort compared to e.g. photonic crystal waveguides.

The realization of such a structure would be a challenging task. However, V-grooves of similar size have been realized successfully in the past in context of electronic micro- and nanodevices [95–97]. Therefore, the realization seems to be feasible.

II. Horizontal slot waveguides

In contrast to the vertical slot waveguide for the horizontal slot waveguide a second high index layer is indispensable. This makes bonding techniques [42, 98] or the deposition of a second high refractive index layer e.g. amorphous silicon [41, 99] necessary. This holds true for the slot material. Here, only a depositable material where the thickness can be sufficiently controlled can be used. On the other hand, from this disadvantage follows one important advantage of the horizontal slot waveguide, studied in-depth for the first time in [57]: All slot interfaces border to deposited layers, which typically have smooth surfaces. In addition, the thickness of the slot is only limited by the controllability of its deposition. Even layer thicknesses in the nanometer range are conceivable.

Due to the layered configuration it is possible to cover the slot waveguide with a different material with respect to the slot. By using air as cladding, one can achieve an ultimately high index contrast. Furthermore, the requirements in terms of realization are significantly relaxed, because the smallest feature size for the lithography is given by the width of the slot waveguide and not by the one order of magnitude smaller slot. This enables the use of faster and cheaper fabrication methods than e-beam such as deep-UV lithography. Finally, the high achievable width-to-height ratio has to be mentioned which is unlimited from the practical point of view.

a) Wire based

The simplest possible horizontal slot waveguide is a type consisting of two wires as shown in Fig. 2.12 II. a). As shown in chapter 5 for such wide structures, the lateral second order mode becomes an issue, but as a result of this chapter a power optimized structure still ensuring single mode behavior can be obtained for a well designed horizontal slot waveguide.

b) Symmetric horizontal slot waveguide based on ribs

The possibility of electric wiring is one main advantage of all rib-type slot waveguides enabling the realization of important active devices such as amplifiers, modulators or lasers. Obviously the advantages and disadvantages of the layered composition as depicted above for the horizontal wire type are still valid. Furthermore, the continuous waveguide layer makes the realization of a suspended waveguides possible. This could enable the realization of new types of sensors. Nevertheless, a structure as shown in Fig. 9.1 II. b) is a very challenging task in realization. But as shown in chapter 6 the high symmetry of this type elevates this structure to a role model for the investigation of the important effect of lateral leakage. For a fully symmetric structure without imperfections coupling to the odd TE slab mode can occur. If the symmetry of the waveguide

is broken by assuming deviations of the waveguide thickness between the upper and the lower layer for instance, also coupling to the even TE slab mode arises. The results of this effect are leakage losses, which easily can exceed 10^2 dB/cm. But as described in chapter 6 for certain waveguide width these losses are avoided due to a destructive interference effect. Again, it is important to which TE slab mode — even or odd — the rib waveguide mode can couple.

c) Asymmetric horizontal slot waveguide based on rib/slab

Much more appealing from the practical point of view compared to Fig. 9.1 II. b) is a structure consisting of a slab and a rib waveguide on top (see Fig. 9.1 II.c)). This would combine all advantages of the horizontal rib- and wire type structures at a minimum of effort in terms of realization. From the practical point of view, this structure is very interesting, because it enables electric wiring as well. Nevertheless, as the in-depth study in chapter 6 revealed, due to the asymmetry of the structure high leakage losses are observed in particular for structures with geometry parameters in the range of optimized slot waveguide structures.

However, by exploiting the resonance characteristic, low loss operation is possible for waveguides with shallow etched ribs and low slot thicknesses where typical deviations due to fabrication processes were taken into account. Moreover, such small slots are no disadvantages as the optimization to linear (see chapter 5) and nonlinear application (see chapter 7) demonstrated.

d) Asymmetric horizontal slot waveguide based on wire/slab.

An special case of Fig. 9.1 II. c) is illustrated in Fig. 9.1 II. d), where the rib on top gives way to a wire. This structure has an increased lateral confinement compared to Fig. 9.1 II. c). Beyond that, due to the slab waveguide as basis, this configuration would be interesting for active devices based on Fig. 9.1 II. c) in sections where no electric wiring is necessary due to the higher lateral confinement.

But as the in-depth studies of the lateral leakage of this structure show, no sufficient parameter region for low loss operation can be found — again, considering deviations due to fabrication tolerances. This can be explained by the fact that the etched wire on top stays in contrast to the above statement for the asymmetric horizontal slot waveguide based on rib/slab where low loss operation only could be ensured for shallow etch depth on top. In other words, the lateral leakage completely renders this configuration useless in practice.

Bibliography

- [1] Y.-H. Kuo, H. Rong, V. Sih, S. Xu, M. Paniccia, and O. Cohen. Demonstration of wavelength conversion at 40 Gb/s data rate in silicon waveguides. *Optics Express*, 14:11721–11726, 2006.
- [2] S. F. Preble, Q. Xu, B. S. Schmidt, and M. Lipson. Ultrafast all-optical modulation on a silicon chip. *Optics Letters*, 30(21):2891–2893, November 2005.
- [3] Q. Xu, D. Fattal, R.G. Beausoleil, Q. Xu, D. Fattal, and R. G. Beausoleil. Silicon microring resonators with 1.5 μm radius. *Optics Express*, 16(6):4309–4315, April 2008.
- [4] J. D. Joannopoulos, S. G. Johnson, J. N. Winn, and R. D. Meade, editors. *Photonic Crystals: Molding the Flow of Light*. Princeton University Press, New Jersey, 2008.
- [5] V. R. Almeida, Q. Xu, R. R. Panepucci, C. A. Barrios, and M. Lipson. Light guiding in low index materials using high-index-contrast waveguides. In *Proceeding of the Mat. Res. Soc. Symp.*, volume 797, page W6.10, 2004.
- [6] Q. Xu, A. R. Vilson, R.R. Panepucci, and M. Lipson. Experimental demonstration of guiding and confining light in nanometer-size low-refractive-index-matrical. *Optics Letters*, 29(14):1626–1628, July 2004.
- [7] V. R. Almeida, Q. Xu, C. A. Barrios, and M. Lipson. Guiding and confining light in void nanostructure. *Optics Letters*, 29(11):1209–1211, June 2004.
- [8] T. Baehr-Jones, M. Hochberg, G. Wang, R. Lawson, Y. Liao, P.A. Sullivan, L. Dalton, A. K.-Y. Jen, and A. Scherer. Optical modulation and detection in slotted silicon waveguides. *Optics Express*, 13(14):5216–5226, July 2005.
- [9] M. Hochberg, T. Baehr-Jones, G. Wang, J. Huang, P. Dalton L. Sullivan, and A. Scherer. Towards a millivolt optical modulator with nano-slot waveguides. *Optics Express*, 15(13):8401–8410, June 2007.
- [10] G. Wang, T. Baehr-Jones, M. Hochberg, and A. Scherer. Design and fabrication of segmented, slotted waveguides for electro-optic modulation. *Applied Physics Letters*, 91:143109–1–143109–3, 2007.
- [11] S. Xiao, F. Wang, X. Wang, Y. Hao, X. Jiang, M. Wang, and J. Yang. Electro-optic polymer assisted optical switch based on silicon slot structure. *Optics Communications*, 282:2506–2510, March 2009.

- [12] C. A. Barrios and M. Lipson. Electrically driven silicon resonant light emitting device based on slot-waveguide. *Optics Express*, 13(25):10092–10101, December 2005.
- [13] K. Preston, J.T. Robinson, and M. Lipson. Slot waveguide cavities for electrically-pumped slot waveguide cavities for electrically-pumped silicon-based light sources. In *Proceedings of the CLEO*, page CThT2, May 2008.
- [14] Y. C. Jun, R. M. Briggs, H. A. Atwater, and M. L. Brongersma. Broadband enhancement of light emission in silicon slot waveguides. *Optics Express*, 17(9):7479–7490, April 2009.
- [15] T. Fujisawa and M. Koshiha. Guided modes of nonlinear slot waveguides. *IEEE Photonics Technology Letters*, 18(14):1530–1532, July 2006.
- [16] T. Fujisawa and M. Koshiha. All-optical logic gates based on nonlinear slot-waveguide couplers. *Journal of the Optical Society of America B*, 23(4):684–691, April 2006.
- [17] E. Jordana, J.-M. Fedeli, L. El Melhaoui, P. Lyan, J. P. Colonna, N. Daldosso, L. Pavesi, P. Pellegrino, B. Garrido, A. Vila, and Y. Lebour. Deep-UV lithography fabrication of slot waveguides and sandwiched waveguides for nonlinear applications. In *Proceedings on the ECIO*, page WB4, April 2007.
- [18] P. Sanchis, J. Blasco, A. Martinez, and J. Marti. Design of silicon-based slot waveguide configurations for optimum nonlinear performance. *Journal of Lightwave Technology*, 25(5):1298–1305, May 2007.
- [19] S. P. Savaidis and N. A. Stathopoulos. Optical confinement in nonlinear low index nanostructures. *Journal of Modern Optics*, 54(11):2699 – 2722, June 2007.
- [20] C. Koos, L. Jacome, C. Poulton, J. Leuthold, and W. Freude. Nonlinear silicon-on-insulator waveguides for all-optical signal processing. *Optics Express*, 15(10):5976–5990, May 2007.
- [21] C. Koos, P. Vorreau, P. Dumon, R. Baets, B. Esembeson, I. Biaggio, T. Michinobu, F. Diederich, W. Freude, and J. Leuthold. Highly-nonlinear silicon photonics slot waveguide. In *Proceedings of the OFC*, page PDP25, March 2008.
- [22] T. Baehr-Jones, B. Penkov, J. Huang, P. Sullivan, J. Davies, J. Takayesu, J. Luo, T.-D. Kim, L. Dalton, A. Jen, M. Hochberg, and A. Scherer. Nonlinear polymer-clad silicon slot waveguide modulator with a half wave voltage of 0.25 V. *Applied Physics Letters*, 92:163303–1–163303–3, 2008.
- [23] T. Vallaitis, S. Bogatscher, L. Alloatti, D. Pumon, R. Baets, L. M. Scimeca, I. Biaggio, F. Diederich, C. Koos, W. Freude, and J. Leuthold. Optical properties of highly nonlinear Siliconorganic hybrid (SOH) waveguide geometries. *Optics Express*, 17(20):17357–17368, September 2009.
- [24] P. Muellner, M. Wellenzohn, and R. Hainberger. Nonlinearity of optimized silicon photonic slot waveguides. *Optics Express*, 17(11):9282–9287, May 2009.

- [25] R. Hainberger and P. Muellner. Nonlinearities of optimized horizontal slot waveguides. In *Proceedings of the IEEE Winter Topicals*, pages 1–2, January 2008.
- [26] T. Baehr-Jones and M. Hochberg. Silicon photonics: Slot machine. *Nature Photonics*, 3(4):193–194, April 2009.
- [27] C. Koos, P. Vorreau, T. Vallaitis, P. Dumon, W. Bogaerts, R. Baets, B. Esembeson, I. Biaggio, T. Michinobu, F. Diederich, W. Freude, and J. Leuthold. All-optical high-speed signal processing with silicon-organic hybrid slot waveguides. *Nature Photonics*, 3:216–219, January 2009.
- [28] F. Dell’Olio and V. M. N. Passaro. Optical sensing by optimized silicon slot waveguides. *Optics Express*, 15(8):4977–4993, April 2007.
- [29] C. A. Barrios, K. B. Gylfason, B. Sanchez, A. Griol, H. Sohlström, M. Holgado, R., and Casquel. Slot-waveguide biochemical sensor. *Optics Letters*, 32(21):3080–3082, November 2007.
- [30] C. A. Barrios, M. J. Banuls, V. Gonzalez-Pedro, K. B. Gylfason, B. Sanchez, A. Griol, A. Maquieira, H. Sohlström, M. Holgado, and R. Casquel. Label-free optical biosensing with slot-waveguides. *Optics Letters*, 33(7):708–710, April 2008.
- [31] C. A. Barrios. Optical slot-waveguide based biochemical sensors. *Sensors*, 9(6):4751–4765, June 2009.
- [32] C. A. Barrios, K. B. Gylfason, B. Sanchez, A. Griol, H. Sohlström, M. Holgado, R., and Casquel. Slot-waveguide biochemical sensor: erratum. *Optics Letters*, 33(21):2554–2555, November 2008.
- [33] C. F. Carlborg, K. B. Gylfason, A. Kamierczak, F. Dortu, M. J. Bañuls Polo, A. Maquieira Catala, G. M. Kresbach, H. Sohlström, T. Moh, L. Vivien, J. Popplewell, G. Ronan, C. A. Barrios, G. Stemme, and W. van der Wijngaart. A packaged optical slot-waveguide ring resonator sensor array for multiplex label-free assays in labs-on-chips. *Lab on a chip*, 10(3):281 – 290, February 2010.
- [34] T. Claes, J. G. Molera, K. De Vos, E. Schacht, R. Baets, and P. Bienstman. Label-free biosensing with a slot-waveguide-based ring resonator in silicon on insulator. *IEEE Photonics Journal*, 1(3):197–204, 2009.
- [35] V. M. N. Passaro, F. Dell’Olio, C. Ciminelli, M. N., and Armenise. Efficient chemical sensing by coupled slot SOI waveguides. *Sensors*, 9:1012–1032, 2009.
- [36] P. Muellner, N. Finger, and R. Hainberger. Lateral leakage in symmetric SOI rib-type slot waveguides. *Optics Express*, 16(1):287–294, January 2008.
- [37] P. Muellner, N. Finger, and R. Hainberger. Leakage studies on SOI slot waveguide structures. In *Proceedings of the SPIE*, volume 6898, pages 1–10, 2008.

- [38] P. Muellner, N. Finger, and R. Hainberger. Resonance based rib-type slot waveguides. In *Proceedings of the ECIO*, volume ThP05, pages 1–4, 2008.
- [39] R. Hainberger, P. Muellner, and M. Wellenzohn. Lateral confinement in horizontal SOI slot waveguide structures. In *Proceedings of the SPIE*, volume 7138, pages 1–8, 2008.
- [40] R. Hainberger, N. Finger, and P. Muellner. Lateral leakage in symmetric SOI rib-type slot waveguides. In *Proceedings of the AOE*, pages 336–338, 2007.
- [41] R. M. Pafchek, J. Li, R. S. Tummidi, and T. L. Koch. Low-loss Si – SiO₂ 8nm slot waveguides. In *Proceedings of the CLEO*, page CThT3, May 2008.
- [42] R. M. Briggs, M. Shearn, A. Scherer, and H. A. Atwater. Wafer-bonded single-crystal silicon slot waveguides and ring resonators. *Applied Physics Letters*, 94:021106–1–021106–3, 2009.
- [43] M. Koshiba, K. Kakihara, and K. Saitoh. Reduced lateral leakage losses of TM-like modes in silicon-on-insulator ridge waveguides. *Optics Letters*, 33:2008–2010, 2008.
- [44] K. Kakihara, K. Saitoh, and M. Koshiba. Generalized simple theory for estimating lateral leakage loss behavior in silicon-on-insulator ridge waveguides. *Journal of Lightwave Technology*, 27(23):5492–5499, December 2009.
- [45] Y. Carts-Powell. Low-index slot serves as waveguide. *Laser Focus World*, February 2004.
- [46] T. Fujisawa and M. Koshiba. Polarization-independent optical directional coupler based on slot waveguides. *Optics Letters*, 31(1):56–58, January 2006.
- [47] L. Chen, J. Shakya, and M. Lipson. Subwavelength confinement in an integrated metal slot waveguide on silicon. *Optics Letters*, 31(14):2133–2135, July 2006.
- [48] T. Baehr-Jones, M. Hochberg, C. Walker, and A. Scherer. High-Q optical resonators in silicon-on-insulator-based slot waveguides. *Applied Physics Letters*, 86:811011–811013, February 2005.
- [49] P. A. Anderson, B. S. Schmidt, and M. Lipson. High confinement in silicon slot waveguides with sharp bends. *Optics Express*, 14(20):9197–9202, October 2006.
- [50] P. Muellner and R. Hainberger. Structural optimization of silicon-on-insulator slot waveguides. *IEEE Photonics Technology Letters*, 18(24):2557–2559, December 2006.
- [51] P. Muellner and R. Hainberger. Power-optimized single-mode slot waveguides. In *Proceedings of the ICPS*, page WeA2s.5, June 2006.
- [52] R. Hainberger and P. Muellner. Modal behavior of SOI slot waveguides. In *Proceedings of the Symposium on Photonics Technologies for 7th Framework Program*, pages 282–285, October 2006.

- [53] C. A. Barrios, Q. Xu, J. Shakya, C. Manolatou, and M. Lipson. Compact silicon slot-waveguide disk resonator. In *proceedings of the Conference on Electro-Optics and Lasers*, page CTuCC3, 2006.
- [54] C. A. Barrios, B. Sanchez, K. B. Gylfason, A. Griol, H. Sohlstroem, M. Holgado, and R. Casquel. Demonstration of slot-waveguide structures on silicon nitride / silicon oxide platform. *Optics Express*, 15(11):6846–6856, May 2007.
- [55] J. Blasco and C.A. Barrios. Compact slot-waveguide/channel-waveguide mode-converter. In *Proceedings of the CLEO*, page 607, June 2005.
- [56] M. Galli, D. Gerace, A. Politi, M. Liscidini, M. Patrini, L. C. Andreani, A. Canino, M. Miritello, R. Lo Savio, A. Irrera, and F. Priolo. Direct evidence of light confinement and emission enhancement in active silicon-on-insulator slot waveguides. *Applied Physics Letters*, 89(24):241114, December 2006.
- [57] C. A. Barrios. Ultrasensitive nanomechanical photonic sensor based on horizontal slot-waveguide resonator. *Photonics Technology Letters*, 18(22):2419–2421, November 2006.
- [58] J. V. Galan, P. Sanchis, J. Blasco, and J. Marti. Study of high efficiency grating couplers for silicon-based horizontal slot waveguides. *IEEE Photonics Technology Letters*, 20(12):985–987, June 2008.
- [59] Vivien L, D. Marris-Morini, A. Griol, K. B. Gylfason, D. Hill, J. Alvarez, H. Sohlström, J. Hurtado, D. Bouville, and E. Cassan. Vertical multiple-slot waveguide ring resonators in silicon nitride. *Optics Express*, 16(22):17237–17242, June 2009.
- [60] R. Sun, P. Dong, Feng, N., Hong, C., J. Michel, M. Lipson, Kimerling, and L. Horizontal single and multiple slot waveguides: Optical transmission at $\lambda = 1550$ nm. *Optics Express*, 15(26):17967–17972, December 2007.
- [61] A. Armaroli, A. Morand, P. Benech, G. Bellanca, and S. Trillo. Comparative analysis of a planar slotted microdisk resonator. *Journal of Lightwave Technology*, 27(18):4009–4016, September 2009.
- [62] A. Di Falco, C. Conti, and G. Assanto. Quadratic phase matching in slot waveguides. *Optics Letters*, 31(21):3146–3148, November 2006.
- [63] N.-N. Feng, R. Sun, L. C. Kimerling, and J. Michel. Lossless strip-to-slot waveguide transformer. *Optics Letters*, 32(10):1250–1252, May 2007.
- [64] C.-Y. Chao. Simple and effective calculation of modal properties of bent slot waveguides. *Journal of the Optical Society of America B*, 24(9):2373–2377, September 2007.
- [65] A. Katigbak, J. F. Strother, and J. Lin. Compact silicon slot waveguide polarization splitter. *Optical Engineering*, 48:080503–1–080503–3, 2009.

- [66] N.-N. Feng, R. Sun, J. Michel, L. C., and Kimerling. Low-loss compact-size slotted waveguide polarization rotator and transformer. *Optics Letters*, 32(15):2131–2133, August 2007.
- [67] H. G. Yoo, Y. Fu, D. Riley, J. H. Shin, and P. M. Fauchet. Birefringence and optical power confinement in horizontal multi-slot waveguides made of Si and SiO₂. *Optics Express*, 16(12):8623–8628, June 2008.
- [68] S.-H. Yang, M. L. Cooper, P. R. Bandaru, S., and Mookherjea. Giant birefringence in multi-slotted silicon nanophotonic waveguides. *Optics Express*, 16(11):8306–8316, May 2008.
- [69] X. Tu, X. Xu, S. Chen, J. Yu, Q., and Wang. Simulation demonstration and experimental fabrication of a multiple-slot waveguide. *IEEE Photonics Technology Letters*, 20(5):333–335, March 2008.
- [70] J. Mu, H. Zhang, and W.-P. Huang. A theoretical investigation of slot waveguide bragg gratings. *IEEE Journal of Quantum Electronics*, 44(7):622–627, July 2008.
- [71] Z. Zheng, M. Iqbal, and J. Liu. Dispersion characteristics of SOI-based slot optical waveguides. *Optics Communications*, 281:5151–5155, 2008.
- [72] A. H. J. Yang, S. D. Moore, B. S. Schmidt, M. Klug, M. Lipson, and Erickson D and. Optical manipulation of nanoparticles and biomolecules in sub-wavelength slot waveguides. *Nature*, 457:71–75, January 2009.
- [73] K. Foubert, L. Lalouat, B. Cluzel, E. Picard, D. Peyrade, E. Delamadeleine, F. de Fornel, and E. Hadji. Near-field modal microscopy of subwavelength light confinement in multimode silicon slot waveguides. *Applied Physics Letters*, 93:251103–1–251103–3, 2008.
- [74] K. Preston and M. Lipson. Slot waveguides with polycrystalline silicon for electrical injection. *Optics Express*, 17(3):1527–1534, February 2009.
- [75] L. Zhang, Y. Yue, Y. Xiao-Li, R. G. Beausoleil, and A. E. Willner. Highly dispersive slot waveguides. *Optics Express*, 17(9):7095–7101, April 2009.
- [76] J. Schrauwen, J. Van Lysebettens, T. Claes, K. De Vos, P. Bienstman, D. Van Thourhout, and R. Baets. Focused-ion-beam fabrication of slots in silicon waveguides and ring resonators. *IEEE Photonics Technology Letters*, 20(23):2004–2006, December 2008.
- [77] M. P. Hiscocks, C.-H. Su, B. C. Gibson, A. D. Greentree, L. C. L. Hollenberg, and F. Ladouceur. Slot-waveguide cavities for optical quantum information applications. *Optics Express*, 17(9):7295–7303, April 2009.
- [78] B. Redding, S. Shi, and D. W. Prather. Electromagnetic analysis of ring-cavity-assisted amplified spontaneous emission in Er : SiO₂/a-si horizontal slot waveguides. *Quantum Electronics*, 45(7):825–829, July 2009.

- [79] C. Maa, Q. Zhang, and E. Van Keuren. Analysis of symmetric and asymmetric nanoscale slab slot waveguides. *Optics Communications*, 282:324–328, June 2009.
- [80] J.-M. Lee, D.-J. Kim, G.-H. Kim, K. O Kwon, K. J. Kim, and G. Kim. Controlling temperature dependence of silicon waveguide using slot structure. *Optics Express*, 16(3):1645–1652, February 2009.
- [81] L. Zhou, K. Okamoto, and S. J. B. Yoo. Athermalizing and trimming of slotted silicon microring resonators with UV-sensitive PMMA upper-cladding. *IEEE Photonics Technology Letters*, 21(17):1175–1177, September 2009.
- [82] G. Z. Mashanovich, M. Milosevic, P. Matavulj, S. Stankovic, B. Timotijevic, P. Y. Yang, E. J. Teo, M. B. H. Breese, A. A. Bettiol, and G.T. Reed. Silicon photonic waveguides for different wavelength regions. *Semiconductor Science and Technology*, 23:064002–1–064002–, May 2008.
- [83] A. Saynatjoki, T. Alasaarela, A. Khanna, L. Karvonen, P. Stenberg, M. Kuittinen, A. Tervonen, and S. Honkanen. Angled sidewalls in silicon slot waveguides: conformal filling and mode properties. *Optics Express*, 17(23):21066–21076, November 2009.
- [84] A. Saynatjoki, T. Alasaarela, A. Khanna, L. Karvonen, A. Tervonen, and S. Honkanen. Advantages of angled sidewalls in slot waveguides. In *Proceedings of the Integrated Photonics and Nanophotonics Research and Applications*, page ITuE2, July 2009.
- [85] P. Muellner and R. Hainberger. Optical characteristics of V-groove waveguide structures. In *Proceedings of the SPIE*, volume 77203, pages 1–9, January 2009.
- [86] C. F. Carlborg, K. B. Gylfason, A. Kamierczak, F. Dortou, M. J. Bañuls Polo, A. Maquieira Catala, G. M. Kresbach, H. Sohlström, T. Moh, L. Vivien, J. Popplewell, G. Ronan, C. A. Barrios, G., and van der Wijngaart W. Stemme. A packaged optical slot-waveguide ring resonator sensor array for multiplex label-free assays in labs-on-chips. *Lab on a chip*, 2010.
- [87] H. Nishihara, M. Haruna, and T. Suhara. *Optical Integrated Circuits*. McGraw-Hill, New York, 1989.
- [88] G. A. Reider. *Photonik - Eine Einfuehrung in die Grundlagen*. Springer, Wien, 2nd edition, 2005.
- [89] K. Okamoto. *Fundamentals of Optical Waveguides*. Academic Press, San Diego, 2000.
- [90] G. Lifante. *Integrated Photonics - Fundamentals*. Wiley, West Sussex, 2003.
- [91] A. W. Snyder and J. D. Love. *Optical Waveguide Theory*. Springer, New York, 1983.
- [92] C. R. Pollock and M. Lipson. *Integrated Photonics*. Kluwer Academic Publisher, Massachusetts, 2003.

- [93] Wolfram Research Inc. *Mathematica 7.0.0*. Champaign IL USA.
- [94] S. P. Pogossian. A new approach to determining the waveguide mode index distribution. *Optical and Quantum Electronics*, 25:417–422, January 1993.
- [95] J. Appenzeller, R. Martel, P. Avouris, J. Knoch, J. Scholvin, J. A. del Alamo, P. Rice, and P. Solomon. Sub-40 nm SOI V-groove n-MOSFETs. *IEEE Electronic device letters*, 23(2):100–102, February 2002.
- [96] G. Pennelli and M. Piotto. Fabrication of silicon nanostructures by geometry controlled oxidation. *Journal of Applied Physics*, 101:104502–1–104502–8, 2007.
- [97] G. Pennelli and M. Piotto. Fabrication and characterization of silicon nanowires with triangular cross section. *Journal of Applied Physics*, 100:054507–1–054507–9, 2006.
- [98] W. P. Maszara, G. Goetz, A. Caviglia, and J. B. McKitterick. Bonding of silicon wafers for silicon-on-insulator. *Journal of Applied Physics*, 64:4943–4950, 1988.
- [99] M. J. A. de Dood, A. Polman, T. Zijlstra, and E. W. J. M. van der Drift. Amorphous silicon waveguides for microphotonics. *Journal of Applied Physics*, 92(2):649–453, July 2002.
- [100] J. Jin. *The Finite Element Method in Electromagnetics*. John Wiley & Sons, New York, 2 edition, 2002.
- [101] Comsol. *Femlab 3.1.0.163*. Berliner Str. 4, 37073 Göttingen, Germany.
- [102] J. C. Nedelec. Mixed finite elements in R^3 . *Numerical Methods*, 35:315–341, 1980.
- [103] The MathWorks, Natick, Massachusetts, USA. *Matlab 7.0.1.24704 (r14) service pack 1*.
- [104] N. Finger, C. Pacher, and W. Boxleitner. *Optical simulation toolkit, online access to MaxWave*. AIT - Austrian Institute of Technology GesmbH., <http://qist.ait.ac.at/maxwave/>.
- [105] A. S. Sudbo. Film mode matching: A versatile numerical method for vector mode field calculations in dielectric waveguides. *Pure and Applied Optics*, 2:211–233, 1993.
- [106] A. S. Sudbo. Improved formulation of the film mode matching method for mode field calculations in dielectric waveguides. *Pure and Applied Optics*, 3:381–388, 1994.
- [107] N. Finger, C. Pacher, and W. Boxleitner. Simulation of guided-wave photonic devices with variational mode-matching. In *Proceedings of the AIP*, volume 893, pages 1493–1494, 2007.
- [108] N. Finger, C. Pacher, and W. Boxleitner. Variational mode-matching: An advanced simulation method for guided-wave photonic devices. In *Proceedings of the NUSOD 05*, 2005.
- [109] F. Grillot, V. Laurent, S. Laval, and E. Cassan. Propagation loss in single-mode ultrasmall square silicon-on-insulator optical waveguides. *IEEE Journal of Lightwave Technology*, 24(2):891–896, February 2006.

-
- [110] J. Berenger. A perfectly matched layer for the absorption of electromagnetic waves. *Journal of Computational Physics*, 114:185–200, 1994.
- [111] Multiphysics 3.2 Comsol. *Electromagnetics Module - User's Guide*. Femlab GmbH., Berliner Strasse 4, Göttingen, 2005.
- [112] E. D. Palik, editor. *Handbook of Optical Constants of Solids I*. Academic Press, San Diego, 1998.
- [113] P. Muellner and R. Hainberger. Power-optimized single-mode slot waveguides. In *AIP Proceedings of the ICPS*, volume 893, pages 1463–1464, July 2006.
- [114] G. T. Reed, editor. *Silicon Photonics*. Wiley, West Sussex, 2008.
- [115] Peng, T.-S., and A. A. Oliner. Guidance and leakage properties of a class of open dielectric waveguides: Part i - mathematical formulations. *IEEE Transactions on microwave theory and techniques*, 29(9):843–855, September 1981.
- [116] A. A. Oliner, Peng, T.-S., T.-I-Hsu, and A. Sanchez. Guidance and leakage properties of a class of open dielectric waveguides: Part ii - new physical effects. *IEEE Transactions on microwave theory and techniques*, 29(9):855–869, September 1981.
- [117] V. Ramaswamy. Strip loaded film waveguide. *Bell System Technical Journal*, 53(4):697–705, April 1974.
- [118] M. A. Webster, R. M. Pafchek, A. Mitchell, and A. Koch. Width dependence of inherent tm-mode lateral leakage loss in silicon-on-insulator ridge waveguides. *IEEE Photonics Technology Letters*, 19(6):429–431, March 2007.
- [119] G. P. Agrawal. *Nonlinear Fiber Optics*. Academic Press, San Diego, 1995.
- [120] Y. R. Shen. *Principles of Nonlinear Optics*. Wiley, New York, 1984.
- [121] A. Harke, M. Krause, and J. Mueller. Low-loss singlemode amorphous silicon waveguides. *Electronic Letters*, 41(25):1377–1378, December 2005.
- [122] L. Wosinski, L. Liu, M. Dainese, and D. Dai. Amorphous silicon in nanophotonic technology. In *Proceedings of the ECIO*, volume ThB1, 2007.
- [123] K. Tiefenthaler and W. Lukosz. Sensitivity of grating couplers as integrated-optical chemical sensors. *J. Optical Soc. Am. B*, 6(2):209–220, February 1989.
- [124] R. G. Heidemann, G. J. Veldhuis, E. W. H. Jager, and P. V. Lambeck. Fabrication and packaging of integrated chemo-optical sensors. *Sensors and Actuators B*, 35:234–240, 1996.
- [125] F. Prieto, B. Sepulveda, A. Calle, A. Llobera, C. Dominguez, A. Abad, A. Montoya, and L.M. Lechuga. An integrated optical interferometric nanodevice based on silicon technology for biosensor applications. *Nanotechnology*, 14:907–912, July 2003.

- [126] A. Densmore, D.-X. Xu, S. Janz, P. Waldron, T. Mischki, G. Lopinski, A. Del  ge, J. Lapointe, P. Cheben, B. Lamontagne, J. H., and Schmid. Spiral-path high-sensitivity silicon photonic wire molecular sensor with temperature-independent response. *Optics Letters*, 33(6):596–598, March 2008.
- [127] D.-X. Xu, A. Densmore, J. H. Schmid, R. Ma, M. Vachon, S. Janz, R. McKinnon, J. Lapointe, A. Del  ge, E., and Cheben P. Post. Spiral cavity Si wire resonators as label-free biosensors. *Integrated Photonics and Nanophotonics Research and Applications*, page IMB2, 2009.
- [128] D.-X. Xu, A. Densmore, A. Del  ge, P. Waldron, R. McKinnon, S. Janz, J. Lapointe, G. Lopinski, T. Mischki, E. Post, P. Cheben, and J.H. Schmid. Folded cavity SOI microring sensors for high sensitivity and real time measurement of biomolecular binding. *Optics Express*, 16(19):15137–1548, September 2008.
- [129] O. Parriaux and G.J. Veldhuis. Normalized analysis for the sensitivity optimization of integrated optical evanescent-wave sensors. *IEEE Journal of Lightwave Technology*, 16(4):573–582, April 1998.
- [130] J. T. Robinson, K. Preston, O. Painter, and Michal Lipson. First-principle derivation of gain in high-index contrast waveguides. *Optics Express*, 16:16659–16669, 2008.
- [131] O. Than and S. B  ttgenbach. Simulation of anisotropic chemical etching of single crystalline silicon using cellular-automata. *Sensors and Actuators A: Physical*, 45:85–89, October 1994.
- [132] W. C. Rheinboldt. *Methods for Solving Systems of Nonlinear Equations*. Society for Industrial Mathematics, Philadelphia, 1987.
- [133] R. Larson and D. C. Falvo. *Elementary Linear Algebra*. Houghton Mifflin Harcourt Publishing Company, Boston, 2009.
- [134] A. Jeffrey and H.-H. Dai. *Handbook of Mathematical Formulas and Integrals*. Academic Press, San Diego, 2008.

Abstract

English

Silicon photonics has attracted much attention in the last decade. Apart from the advantage stemming from the CMOS compatibility, the high refractive index of silicon enables the realization of extremely small waveguide structures, *e.g.* microring resonators with diameters of only a few microns. However, silicon photonics is more than about shrinking component sizes and also allows for the utilization of unique effects such as 'slow light' in photonic crystal defect waveguides.

In 2005 another novel effect entered the stage of silicon photonics: The so-called photonic slot effect, which confines a significant amount of the guided optical power in a narrow low index region between two silicon waveguide cores. This unique feature is highly beneficial for various applications such as sensors, modulators or for nonlinear optical devices.

In this thesis some fundamental aspects of slot waveguides are studied with analytical and numerical methods. All investigations focus on the possible realization of the slot waveguide in practice. At first, an analytical framework is developed in order to qualitatively show the origin of the slot effect using a 2D model. Then, a structural optimization of the 3D structure is performed employing numerical methods. The results show, that it is possible to further increase the confined power significantly in the slot region while maintaining single mode operation - a crucial prerequisite for most applications. Next, two leakage loss mechanisms are studied. One is the rarely known lateral leakage, which is studied for the horizontal slot waveguide concept for the first time in context of this work. One main result is that the lateral leakage renders some - from the practical point of view - very interesting slot waveguide concepts useless due to the high amount of leakage which occurs. A main area of application for the slot waveguide structure is the efficient exploitation of nonlinear effects. As exposed in this thesis, the horizontal concept reveals some noticeable advantages compared to other concepts with respect to such applications. Finally, the last chapter is dedicated to a novel type of slot waveguide - the so-called V-groove waveguide which was a result of the preceding work. There, the slot is replaced by a V-shaped groove.

Deutsch

Der Bereich der Silizium-Photonik ist ein noch junger und sehr viel versprechender Zweig der Photonik. Neben der CMOS Kompatibilität ermöglicht der hohe Brechungsindexunterschied zwischen dem Wellenleitermaterial Silizium und dem umgebenden Material extrem kompakte Strukturen, wie zum Beispiel Microring-Resonatoren mit Durchmesser im Bereich von wenigen Mikrometern. Doch Silizium-Photonik ist mehr als nur ein „Skalierungsfaktor“ um hochkompakte Wellenleiterstrukturen zu erzielen. Der hohe Brechungsindexunterschied ermöglicht so einzigartige Effekte wie die extreme Verlangsamung des Lichts in „Photonic Crystal defect Waveguides“ die wegen den hohen Ansprüchen an die Herstellungstechnologie erst jetzt realisiert werden können.

2005 betrat ein neuer Effekt die Bühne der Silizium-Photonik: Der photonische „Slot Effekt“. Ein Slotwellenleiter besteht aus zwei durch einen Spalt (den sog. Slot) getrennte Wellenleiterkerne aus Silizium. Bei optimierter Auslegung im Bezug auf die Geometrie ist ein großer Teil des Lichts nicht im Wellenleiter selbst sondern im Slot dazwischen konzentriert.

In der vorliegenden Arbeit werden einige sehr grundlegende Aspekte von Slot Wellenleitern numerisch und analytisch untersucht, wobei stark auf die tatsächlichen Möglichkeiten der Herstellung Rücksicht genommen wird. Zu Beginn werden die analytischen Grundlagen anhand des 2D Modells erarbeitet um den physikalischen Ursprung des Effekts zu ergründen. Dem folgt die numerische Optimierung der 3D Struktur in Hinblick auf maximale Leistung. Wie gezeigt wird, ist es möglich die Lichtleistung im Spalt durch Erhöhung der Wellenleiterbreite deutlich zu erhöhen, ohne das für die meisten Anwendungen entscheidende Singlemode-Verhalten zu gefährden.

Weiters werden zwei Ursachen für Wellenleiter Verluste untersucht. Unter anderem ist dies die eher unbekannte „Lateral Leakage“. Diese wurde im Rahmen dieser Arbeit erstmals für horizontale Slot Wellenleiter studiert. Ein wichtiges Resultat dieser Studien ist, dass einige - vom praktischen Standpunkt aus - sehr interessante Slot Wellenleiterformen nur eingeschränkt oder wegen den hohen Verlusten gar nicht in der Praxis eingesetzt werden können. Ein wichtiges Anwendungsgebiet ist die Ausnutzung nichtlinearer Effekte. Ein Kapitel dieser Arbeit optimiert die horizontale Struktur numerisch in Hinblick auf diese Anwendung und zeigt, daß hier durch das horizontale Konzept feststellbare Vorteile in der Praxis entstehen. Der letzte Abschnitt der Dissertation widmet sich einer im Rahmen dieser Arbeit entdeckten neuartigen Struktur dem sog. V-Groove Wellenleiter bei dem der Spalt durch eine V-förmigen Bereich ersetzt wird.

Publications

P. Muellner, R. Hainberger. Single-mode criterion for rib waveguides with small cross sections. In *Proceedings of the SPIE 6115 Physics and Simulation of Optoelectronic Devices XIV*, 2006.

P. Muellner and R. Hainberger. Power-optimized single-mode slot waveguides. In *Proceedings of the ICPS*, page WeA2s.5, 2006.

P. Muellner and R. Hainberger. Structural optimization of silicon-on-insulator slot waveguides. *IEEE Photonics Technology Letters*, 18(24):2557-2559, 2006.
cited by 14 publications

R. Hainberger and P. Muellner. Modal behavior of SOI slot waveguides. In *Proceedings of the Symposium on Photonics Technologies for 7th Framework Program*, pages 282-285, 2006.

R. Hainberger, N. Finger and P. Muellner. Lateral leakage in symmetric SOI rib-type slot waveguides. In *Proceedings AOE 2007*, pages 336, 2007.

P. Muellner, N. Finger, and R. Hainberger. Leakage studies on SOI slot waveguide structures. In *Proceedings of the SPIE*, volume 6898, pages 1-10, 2008.

P. Muellner, N. Finger, and R. Hainberger. Lateral leakage in symmetric SOI rib-type slot waveguides. *Optics Express*, 16(1):287-294, 2008.
cited by 2 publications

P. Muellner, N. Finger, and R. Hainberger. Resonance based rib-type slot waveguides. In *Proceedings of the ECIO*, volume ThP05, pages 1-4, 2008.

R. Hainberger, P. Muellner, and M. Wellenzohn. Lateral confinement in horizontal SOI slot waveguide structures. In *Proceedings of the SPIE*, volume 7138, pages 1-8, 2008.

P. Muellner, R. Bruck, K. Roppert, and R. Hainberger. Integrated silicon photonic Mach-Zehnder interferometer for label-free biosensing. In *Proceedings of the ME2008 - Mikroelektroniktagung*, 2008.

R. Hainberger and P. Muellner. Nonlinearities of optimized horizontal slot waveguides. In *Proceedings of the IEEE Winter Topicals*, pages 1-2, 2008.

P. Muellner, M. Wellenzohn, and R. Hainberger. Nonlinearity of optimized silicon photonic slot waveguides. *Optics Express*, 17(11):9282-9287, 2009.

cited by 7 publications

P. Muellner and R. Hainberger. Optical characteristics of V-groove waveguide structures. In *Proceedings of the SPIE*, volume 77203, pages 1-9, 2009.

cited by 2 publications

R. Hainberger, R. Bruck, P. Muellner, K. Roppert, W. Boxleitner, C. Pacher and N. Finger. Design of silicon and polymer photonic waveguide structures for sensing applications. In *Proceedings of the SPIE*, volume 7386, pages 73862Q-73862Q-15, 2009.

R. Hainberger, P. Muellner and R. Bruck. SOI photonic wire Bragg gratings for interferometric sensor arrays. In *Proceedings of the ECIO 2010*, volume WeP39, 2010.

R. Hainberger, R. Bruck and P. Muellner. Silicon-photonic wire Bragg reflectors for wavelength-multiplexed interferometric sensor arrays. In *Proceedings of the Nanophotonics 2010*, 2010.

P. Muellner, R. Bruck, R. Hainberger, M. Karl, M. Baus and T. Wahlbrink. Silicon nanophotonic components for an integrated refractometric sensor array. In *Proceedings of Eurosensors XXIV*, 2010.

S. Schrittwieser, J. Schotter, T. Maier, R. Bruck, P. Muellner, N. Kataeva, K. Soulantika, F. Ludwig, A. Huetten and H. Brueckl. Homogeneous biosensor based on optical detection of the rotational dynamics of anisotropic nanoparticles. In *Proceedings of Eurosensors XXIV*, 2010.

A. Effective index approximation

As shown in [94], a transcendent equation of the form

$$x'y(x') = f[y], \quad (\text{A.1})$$

can be expanded in the series:

$$\begin{aligned} y(x') = & \frac{f[0]}{x'} + \frac{f[0]f^{(1)}[0]}{x'^2} + \frac{f[0][f^{(1)}[0]]^2 + f^2[0]f^{(2)}[0]/2}{x'^3} + \\ & + \frac{f[0][f^{(1)}[0]]^3 + 3f^2[0]f^{(1)}[0]f^{(2)}[0]/2}{x'^4} + \\ & + \frac{120f[0]f'[0]^4 + 360f[0]^2f'[0]^2f''[0] + 60f[0]^3f''[0]^2 + 80f[0]^3f'[0]f^{(3)}[0] + 5f[0]^4f^{(4)}[0]}{120x'^5} + \dots, \end{aligned} \quad (\text{A.2})$$

where the notation

$$[f^n(0)]^{(n-1)} = \left[\frac{d^{n-1}[f^n[y]]}{dy^{n-1}} \right]_{y=0}, \quad (\text{A.3})$$

is used. After collecting all terms which are of same order in $f[0]$ one obtains:

$$\begin{aligned} y(x') = & f[0] \left(\frac{1}{x'} + \frac{f^{(1)}[0]}{x'^2} + \frac{[f^{(1)}[0]]^2}{x'^3} + \dots \right) + \\ & + \frac{f^2[0]f^{(2)}[0]}{2} \left(\frac{1}{x'^3} + 3\frac{f^{(1)}[0]}{x'^4} + 6\frac{[f^{(1)}[0]]^2}{x'^5} + \dots \right) + \dots \end{aligned} \quad (\text{A.4})$$

The series' in the parenthesis are convergent for $|f^{(1)}/x'| < 1$ and can be replaced by:

$$\begin{aligned} \frac{1}{[x' - f^{(1)}[0]]^n} = & \frac{1}{x'^n} + \frac{nf^{(1)}[0]}{x'^{n+1}} + \dots \\ & + \frac{n(n+1) \dots (n+j-1)}{j!} \frac{[f^{(1)}[0]]^j}{x'^{n+j}} + \dots \end{aligned} \quad (\text{A.5})$$

Introduced to (A.4) this finally leads to:

$$y(x') = \frac{f[0]}{x' - f^{(1)}[0]} + \frac{f^2[0]f^{(2)}[0]}{2[x' - f^{(1)}[0]]^3} + \frac{f^3[0]f^{(3)}[0]}{6[x' - f^{(1)}[0]]^4} + \frac{f^3[0][f^{(2)}[0]]^2}{2[x' - f^{(1)}[0]]^5} + \dots \quad (\text{A.6})$$

With this expansion transcendent eigenmode equations can approximately be solved by keeping only terms of low order in $\frac{1}{[x' - f^{(1)}[0]]^n}$. For the sake of comparison, two eigenmode equations are solved using (A.6). The first describes an asymmetric three layer system as sketched in A.1 a) where

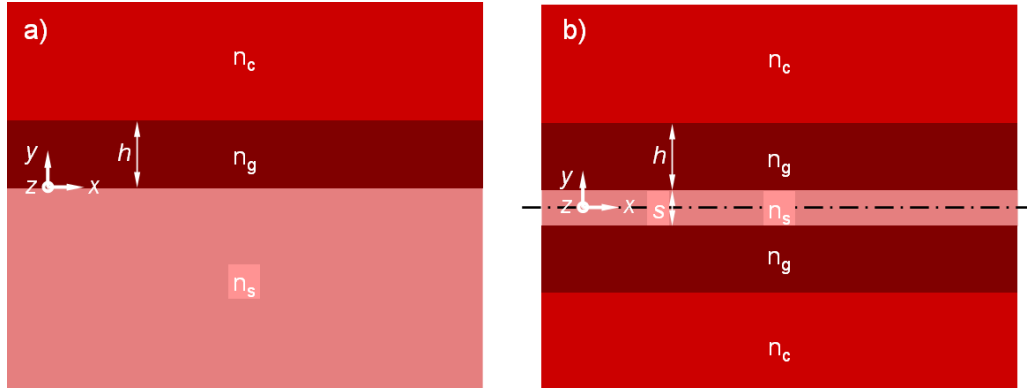


Figure A.1.: Geometry- and refractive index parameters of a) an asymmetric three layer waveguide and b) a symmetric slot waveguide. The propagation direction is in z .

n_c is the refractive index of the upper buffer and n_s of the lower buffer layer. n_g is the refractive index of the waveguiding layer and h its height:

$$k_0 h n_{ge} = \pi - \tan^{-1} \left(k_c \frac{n_{ge}}{n_{ec}} \right) - \tan^{-1} \left(k_s \frac{n_{ge}}{n_{es}} \right), \quad (\text{A.7})$$

for the fundamental mode, respectively [87]. For the TM mode $k_c = n_c^2/n_g^2$ and $k_s = n_s^2/n_g^2$ holds true. In addition, recalling that the $n_{ge,ec,es}$ are the index differences defined as:

$$\begin{aligned} n_{ge} &= \sqrt{n_g^2 - n_{\text{eff}}^2} \\ n_{es} &= \sqrt{n_{\text{eff}}^2 - n_s^2} \\ n_{ec} &= \sqrt{n_{\text{eff}}^2 - n_c^2} \end{aligned} \quad (\text{A.8})$$

The second transcendent equation specifies the symmetric slot waveguide as depicted in A.1 b). According to [7] the eigenmode equation can be rewritten resulting in:

$$k_0 h n_{ge} = \pi - \tan^{-1} \left(k_c \frac{n_{ge}}{n_{ec}} \right) - \tan^{-1} \left(k_s \frac{n_{ge}}{n_{es}} \cotanh(k_0 n_{es} s / 2) \right), \quad (\text{A.9})$$

where in extension to the three layer system $n_{es} = \sqrt{n_{\text{eff}}^2 - n_s^2}$ must be added. It has to be noted that (A.9) gives the same results as (2.9). Equations (A.7) and (A.9) only differ in the second term on the right side, involving the slot index n_s and the slot thickness s . The refractive index of the slot and of the lower buffer layer of the three layer system are intentionally equal. In this case for $s \gg \lambda$ in the second term of equation (A.9) $\cotanh(k_0 n_{es} s / 2) \rightarrow 1$ and (A.9) becomes identical to (A.7). To obtain equations depending on only one variable, the denominators of equation (A.7) are

expanded with $+n_g^2 - n_g^2$ resulting in:

$$k_0 h \sqrt{n_g^2 - n_{\text{eff}}^2} = \pi - \tan^{-1} \left(k_c \sqrt{\frac{n_g^2 - n_{\text{eff}}^2}{n_{\text{eff}}^2 - n_c^2 + n_g^2 - n_g^2}} \right) - \tan^{-1} \left(k_s \sqrt{\frac{n_g^2 - n_{\text{eff}}^2}{n_{\text{eff}}^2 - n_s^2 + n_g^2 - n_g^2}} \right). \quad (\text{A.10})$$

After rearranging and combining the refractive index differences obeying the rule $n_{xy} = \sqrt{n_x^2 - n_y^2}$ where the subscript e is an abbreviation for the effective index subscript 'eff' one obtains:

$$k_0 h n_{ge} = \pi - \tan^{-1} \left(k_c \frac{n_{ge}}{\sqrt{n_{gc}^2 - n_{ge}^2}} \right) - \tan^{-1} \left(k_s \frac{n_{ge}}{\sqrt{n_{gs}^2 - n_{ge}^2}} \right). \quad (\text{A.11})$$

Now, n_{ge} is left as only variable. Of course, other possibilities can be found to obtain similar results. In the same manner equation (A.9) can be altered resulting in:

$$k_0 h n_{ge} = \pi - \tan^{-1} \left(k_c \frac{n_{ge}}{\sqrt{n_{gc}^2 - n_{ge}^2}} \right) - \tan^{-1} \left(k_s \frac{n_{ge}}{\sqrt{n_{gs}^2 - n_{ge}^2}} \coth \left(k_0 \sqrt{n_{gs}^2 - n_{ge}^2} (s/2) \right) \right), \quad (\text{A.12})$$

By identifying

$$\begin{aligned} x' &= k_0 h \\ y(h) &= n_{ge} \\ f(y) &= \text{right side of (A.11) or (A.12)}, \end{aligned} \quad (\text{A.13})$$

equations (A.11) or (A.12) are of the form (A.1) and can be approximated by using (A.6). By restricting the studies to the first term in (A.6) only $f[0]$ and the first derivative with respect to n_{ge} $f[0]^{(1)}$ is needed. This results in:

for (A.11)		for (A.12)	
$f[0] = \pi$		$f[0] = \pi$	(A.14)
$f[0]^{(1)} = -\frac{k_c}{n_{gc}} - \frac{k_s}{n_{gs}}$		$f[0]^{(1)} = -\frac{k_c}{n_{gc}} - \frac{k_s}{n_{gs}} \coth(k_0 n_{gs} s/2)$	

Inserting this in (A.6) leads to:

$$\begin{array}{c|c}
 \text{for (A.11)} & \text{for (A.12)} \\
 \hline
 n_{\text{ge}} = \frac{\pi}{hk_0 + \frac{k_c}{n_{\text{gc}}} + \frac{k_s}{n_{\text{gs}}}} & n_{\text{ge}} = \frac{\pi}{hk_0 + \frac{k_c}{n_{\text{gc}}} + \frac{k_s}{n_{\text{gs}} \coth(k_0 n_{\text{gs}} s/2)}}
 \end{array} \quad (\text{A.15})$$

By using that $n_{\text{ge}} = \sqrt{n_g^2 - n_{\text{eff}}^2}$ the approximation of the two effective indices can be finalized:

$$\text{three layer: } n_{\text{eff}} = \sqrt{n_g^2 - \left(\frac{\pi}{hk_0 + \frac{n_c^2}{n_g^2 n_{\text{gc}}} + \frac{n_s^2}{n_g^2 n_{\text{gs}}}} \right)^2} \quad (\text{A.16})$$

$$\text{slot: } n_{\text{eff}} = \sqrt{n_g^2 - \left(\frac{\pi}{hk_0 + \frac{n_c^2}{n_g^2 n_{\text{gc}}} + \frac{n_s^2 \coth(k_0 n_{\text{gs}} s/2)}{n_g^2 n_{\text{gs}}}} \right)^2} \quad (\text{A.17})$$

Here, to enable an eased interpretation in chapter 2 $k_{s,c} = n_{s,c}^2/n_g^2$ was inserted.

B. The variational mode matching (VMM) method Of MaxWave

B.1. Introduction

MaxWave [104] is a collection of electromagnetic mode solvers for the computation of the optical field in guided-wave optoelectronic/photonic devices. The underlying field equations (time-harmonic Maxwell's equations) are solved rigorously by employing an advanced mode-matching technique — the so-called variational mode matching [104–108] technique — which combines numerical efficiency with a very high degree of numerical stability. Currently, MaxWave comprises powerful 2D simulation tools for the analysis of (a)periodic waveguide grating structures, tapers and waveguide junctions as well as mode solvers for 2D waveguide cross sections. The devices may incorporate lossy (and gainy) materials with potentially high refractive index differences which makes MaxWave suitable for the simulation of ultra-high-index-contrast materials or waveguide structures incorporating metals. In addition, anisotropic materials can be handled having a dielectric tensor of the form $\underline{\epsilon} = \text{diag}(\epsilon_{rr}, \epsilon_{rr}, \epsilon_{zz})$ where the (vertical) z -direction is the growth direction of the slab waveguides. This feature makes MaxWave attractive for the simulation of optoelectronic devices employing intersubband absorption/emission and birefringent waveguide structures. Though MaxWave primarily targets at guided-wave devices, unbounded radiating fields can be handled efficiently through the incorporation of perfectly-matched layers (PMLs) acting as artificial absorbers. Thus, leaky waveguide structures as well as grating coupled radiation fields and/or scattered fields at waveguide junctions can be analyzed accurately. Special effort has been put on a stable implementation of the variational mode-matching technique. Only a minimum a-priori knowledge on the modal structure of the simulated devices is required by the user.

B.2. General Information

The devices are modeled as a juxtaposition of different local slab waveguides (growth direction z) with piecewise constant dielectric permittivities. In all models wave propagation is along the sx -direction. In analogy to most other mode-matching (and partly also FDTD) approaches the range of possible geometries is subject to mild restrictions. However, in a large variety of practical devices this restriction is of minor severity. Compared to “brute-force” methods from the viewpoint of device physics (such as FEM and FDTD), however, the solutions of the MaxWave-solvers reveal much more insight into device physics and the structure of the optical field. For example, transmission, reflection, (and losses) from and into individual modes can be directly obtained. Moreover,

there is no need for concern on phase errors in long resonating devices. The MaxWave-solvers are optimally efficient if following prerequisites are satisfied: (i) The z -dimension does not exceed $L_z \sim 10$ wavelengths. Larger z -dimensions (up to ~ 50 wavelengths) can be dealt with. However, one should be aware that the computational effort depends on L_z in a cubic fashion. (ii) In general, the aspect ratio of the device should be kept rather low, since the computation time depends only linearly on the number of horizontal device sections. (iii) The addition of (also very long) homogeneous waveguide sections has no significant impact on the computational cost.

B.3. Detailed Description

MaxWave includes two different sets of simulation tools: a 2D simulator VMMXd and a solver suite CrossSecWG for waveguide cross-sections. In both cases the time harmonic Maxwell's equations

$$\text{rot} \vec{E} = ik_0 \vec{H} \quad (\text{B.1})$$

$$\text{rot} \vec{H} = -ik_0 \underline{\epsilon} \vec{E} \quad (\text{B.2})$$

where $k_0 = \frac{\omega}{c_0} = \frac{2\pi}{\lambda_0}$ are solved (time dependence $\exp(-i\omega t)$). Notice that the magnetic field has been rescaled: $\vec{H} = Z_0 \vec{H}^{(\text{phys})}$ where $Z_0 = \sqrt{\frac{\mu_0}{\epsilon_0}}$ is the vacuum impedance.

B.3.1. Perfectly Matched Layers (PMLs)

PMLs are introduced via the complex variable stretching technique: $z \mapsto \Re(z) + i \int_0^{\Re(z)} d\tau \sigma_z(\tau)$ with piecewise constant σ_z . Thus, PML layers are characterized by a complex layer thickness.

B.3.2. CrossSecWG

Purpose of the CrossSecWG-solvers is the computation of the optical modes in waveguide cross-sections. The horizontal direction is the y -direction. The left and the right boundary may have either PEC, PMC, or radiation boundary conditions. PML layers acting in the y -direction can be used. The modal fields to be computed have the general form

$$\vec{\Phi}(x, y, z; \lambda) = \vec{\Phi}(y, z) e^{ik_0 \lambda x} \quad (\text{B.3})$$

where $\vec{\Phi}$ denotes the electric or the magnetic field and λ is the effective refractive index of the mode.

Scalar approximation

The wave equation to be solved is

$$\partial_y \hat{c} \partial_y \Phi + \partial_z \hat{a} \partial_z \Phi + k_0^2 \hat{b} \Phi = k_0^2 \lambda^2 \hat{c} \Phi \quad (\text{B.4})$$

where $\Phi = E_y$ in TE- and $\Phi = H_y$ in TM-polarization. The other non-zero field components are $H_z, E_z = \mp \frac{i}{k_0} \hat{c} \partial_x \Phi = H_z$ [TE/TM], and $H_x, E_x = \pm \frac{i}{k_0} \hat{c} \partial_z \Phi = H_x$ [TE/TM]. It is important to note that in MaxWave the propagation is assumed in x -direction. A necessary condition for the validity of the scalar approximation is that the guiding in the y -direction is rather weak. In a layer l , $y_{l-1} \leq y \leq y_l = y_{l-1} + d_l$, with y -independent optical constants the optical field is expanded in terms of local waveguide modes:

$$\Phi(x, y, z; \lambda) = \sum_{\rho=1}^N \phi_{\rho}^{(l)}(z) \left[A_{\rho}^{(l)} e^{ik_0 \theta_{\rho}^{(l)}(y-y_{l-1})} + B_{\rho}^{(l)} e^{-ik_0 \theta_{\rho}^{(l)}(y-y_l)} \right] e^{ik_0 \lambda x} \quad (\text{B.5})$$

where $\theta_{\rho}^{(l)} = +\sqrt{(v_{\rho}^{(l)})^2 - \lambda^2}$. The local waveguide modes are thus defined to be $\{v_{\rho}^{(l)} = \sqrt{\lambda^2 + (\theta_{\rho}^{(l)})^2}, \phi_{\rho}^{(l)}(z)\}$. They are computed as explained in Appendix B.4. Across the interfaces $y = y_l$ the field components Φ and $-\frac{i}{k_0} \hat{c} \partial_y \Phi$ must be continuous. These continuity conditions are enforced in a weak sense using the shape functions $\varphi_j(z)$ as weights. The inverse scattering matrix is given by

$$\begin{bmatrix} \mathbf{t}_l \vec{A}_l \\ \mathbf{t}_{l+1} \vec{B}_{l+1} \end{bmatrix} = \underbrace{\begin{bmatrix} \mathbf{C}_l & -\mathbf{C}_{l+1} \\ \mathbf{D}_l & \mathbf{D}_{l+1} \end{bmatrix}^{-1} \cdot \begin{bmatrix} -\mathbf{C}_l & \mathbf{C}_{l+1} \\ \mathbf{D}_l & \mathbf{D}_{l+1} \end{bmatrix}}_{\begin{bmatrix} \hat{\mathbf{R}}_{l,l+1} & \hat{\mathbf{T}}_{l,l+1} \\ \hat{\mathbf{T}}_{l+1,l} & \hat{\mathbf{R}}_{l+1,l} \end{bmatrix}} \cdot \begin{bmatrix} \vec{B}_l \\ \vec{A}_{l+1} \end{bmatrix} \quad (\text{B.6})$$

with $\mathbf{t}^{(l)} = \text{diag}(e^{ik_0 \theta_{\rho}^{(l)} d_l})$, $(\mathbf{C}^{(l)})_{m\rho} = \langle \varphi_m | \phi_{\rho}^{(l)} \rangle$, and $(\mathbf{D}^{(l)})_{m\rho} = \langle \varphi_m | \theta_{\rho}^{(l)} \hat{c}^{(l)} \phi_{\rho}^{(l)} \rangle$. Upon swapping the materials in the l and $l+1$ the inverse scattering matrix transforms as follows:

$$\begin{bmatrix} \hat{\mathbf{R}}_{l,l+1} & \hat{\mathbf{T}}_{l,l+1} \\ \hat{\mathbf{T}}_{l+1,l} & \hat{\mathbf{R}}_{l+1,l} \end{bmatrix} \longrightarrow \begin{bmatrix} \hat{\mathbf{R}}_{l+1,l} & \hat{\mathbf{T}}_{l+1,l} \\ \hat{\mathbf{T}}_{l,l+1} & \hat{\mathbf{R}}_{l,l+1} \end{bmatrix} \quad (\text{B.7})$$

The outer boundary conditions at $y = y_0$ and $y = y_n$ are either PEC, PMC, or open boundary conditions. These are formulated as $\vec{A}_1 + \sigma_1 \mathbf{t}_1 \vec{B}_1 = 0$ and $\vec{B}_n + \sigma_n \mathbf{t}_n \vec{A}_n = 0$. For the combinations TE+PEC and TM+PMC $\sigma = -1$, for TM+PEC and TE+PMC $\sigma = 1$; $\sigma = 0$ for open boundary conditions. With these ingredients the continuity/boundary conditions are assembled in a banded

matrix scheme:

$$\begin{bmatrix}
 \mathbf{I} & \sigma_1 \mathbf{t}_1 & & & & & \\
 -\mathbf{t}_1 & \hat{\mathbf{R}}_{1,2} & \hat{\mathbf{T}}_{1,2} & & & & \\
 & \hat{\mathbf{T}}_{2,1} & \hat{\mathbf{R}}_{2,1} & -\mathbf{t}_2 & & & \\
 & & -\mathbf{t}_2 & \hat{\mathbf{R}}_{2,3} & \hat{\mathbf{T}}_{2,3} & & \\
 & & & \hat{\mathbf{T}}_{3,2} & \hat{\mathbf{R}}_{3,2} & -\mathbf{t}_3 & \\
 & & & & -\mathbf{t}_3 & \ddots & \ddots \\
 & & & & & \ddots & \ddots & -\mathbf{t}_{n-1} \\
 & & & & & & -\mathbf{t}_{n-1} & \hat{\mathbf{R}}_{n-1,n} & \hat{\mathbf{T}}_{n-1,n} \\
 & & & & & & & \hat{\mathbf{T}}_{n,n-1} & \hat{\mathbf{R}}_{n,n-1} & -\mathbf{t}_n \\
 & & & & & & & & \sigma_n \mathbf{t}_n & \mathbf{I}
 \end{bmatrix} \cdot \begin{bmatrix} \vec{A}_1 \\ \vec{B}_1 \\ \vec{A}_2 \\ \vec{B}_2 \\ \vec{A}_3 \\ \vdots \\ \vec{A}_{n-1} \\ \vec{B}_{n-1} \\ \vec{A}_n \\ \vec{B}_n \end{bmatrix} = 0 \quad (\text{B.8})$$

To solve this nonlinear eigenproblem for the eigenvalue λ and the eigenvector the matrix secant method described in Appendix B.5 is applied.

With the definition

$$\psi_\rho^{(l)}(y) = A_\rho^{(l)} e^{ik_0 \theta_\rho^{(l)}(y-y_{l-1})} + B_\rho^{(l)} e^{-ik_0 \theta_\rho^{(l)}(y-y_l)} \quad (\text{B.9})$$

the resulting electromagnetic field components in TE-polarization are given as follows:

$$E_x^{(l)}(y, z; \lambda) = 0 \quad (\text{B.10})$$

$$E_y^{(l)}(y, z; \lambda) = \Phi(y, z) = \sum_\rho \phi_{y\rho}^{(l)}(z) \psi_\rho^{(l)}(y) \quad (\text{B.11})$$

$$E_z^{(l)}(y, z; \lambda) = 0 \quad (\text{B.12})$$

$$H_x^{(l)}(y, z; \lambda) = \sum_\rho \phi_{x\rho}^{(l)}(z) \psi_\rho^{(l)}(y) \quad (\text{B.13})$$

$$H_y^{(l)}(y, z; \lambda) = 0 \quad (\text{B.14})$$

$$H_z^{(l)}(y, z; \lambda) = \sum_\rho \phi_{z\rho}^{(l)}(z) \frac{\lambda}{v_\rho^{(l)}} \psi_\rho^{(l)}(y) \quad (\text{B.15})$$

In TM-polarization one obtains

$$E_x^{(l)}(y, z; \lambda) = -\sum_\rho \phi_{x\rho}^{(l)}(z) \psi_\rho^{(l)}(y) \quad (\text{B.16})$$

$$E_y^{(l)}(y, z; \lambda) = 0 \quad (\text{B.17})$$

$$E_z^{(l)}(y, z; \lambda) = -\sum_\rho \phi_{z\rho}^{(l)}(z) \frac{\lambda}{v_\rho^{(l)}} \psi_\rho^{(l)}(y) \quad (\text{B.18})$$

$$H_x^{(l)}(y, z; \lambda) = 0 \quad (\text{B.19})$$

$$H_y^{(l)}(y, z; \lambda) = \Phi(y, z) = \sum_\rho \phi_{y\rho}^{(l)}(z) \psi_\rho^{(l)}(y) \quad (\text{B.20})$$

$$H_z^{(l)}(y, z; \lambda) = 0 \quad (\text{B.21})$$

The fields $\phi_{ip}^{(l)}$, $i = y, z, x$, are defined in (B.34).

Fully vectorial solver

The full set of Maxwell's equations for the optical fields with an x -propagation factor $e^{ik_0\lambda x}$ is solved employing an expansion in terms of rotated local eigenmodes of both TE(e)- and TM(h)-polarization. The scattering matrix has following substructure:

$$\begin{bmatrix} \hat{\mathbf{R}}_{l,l+1} & \hat{\mathbf{T}}_{l,l+1} \\ \hat{\mathbf{T}}_{l+1,l} & \hat{\mathbf{R}}_{l+1,l} \end{bmatrix} = \begin{bmatrix} \hat{\mathbf{R}}_{l,l+1}^{ee} & \hat{\mathbf{R}}_{l,l+1}^{eh} & \hat{\mathbf{T}}_{l,l+1}^{ee} & \hat{\mathbf{T}}_{l,l+1}^{eh} \\ \hat{\mathbf{R}}_{l,l+1}^{he} & \hat{\mathbf{R}}_{l,l+1}^{hh} & \hat{\mathbf{T}}_{l,l+1}^{he} & \hat{\mathbf{T}}_{l,l+1}^{hh} \\ \hat{\mathbf{T}}_{l+1,l}^{ee} & \hat{\mathbf{T}}_{l+1,l}^{eh} & \hat{\mathbf{R}}_{l+1,l}^{ee} & \hat{\mathbf{R}}_{l+1,l}^{eh} \\ \hat{\mathbf{T}}_{l+1,l}^{he} & \hat{\mathbf{T}}_{l+1,l}^{hh} & \hat{\mathbf{R}}_{l+1,l}^{he} & \hat{\mathbf{R}}_{l+1,l}^{hh} \end{bmatrix} \quad (\text{B.22})$$

Swapping the materials in layers l and $l+1$ results in the scattering matrix

$$\begin{bmatrix} \hat{\mathbf{R}}_{l+1,l}^{ee} & -\hat{\mathbf{R}}_{l+1,l}^{eh} & \hat{\mathbf{T}}_{l+1,l}^{ee} & -\hat{\mathbf{T}}_{l+1,l}^{eh} \\ -\hat{\mathbf{R}}_{l+1,l}^{he} & \hat{\mathbf{R}}_{l+1,l}^{hh} & -\hat{\mathbf{T}}_{l+1,l}^{he} & \hat{\mathbf{T}}_{l+1,l}^{hh} \\ \hat{\mathbf{T}}_{l,l+1}^{ee} & -\hat{\mathbf{T}}_{l,l+1}^{eh} & \hat{\mathbf{R}}_{l,l+1}^{ee} & -\hat{\mathbf{R}}_{l,l+1}^{eh} \\ -\hat{\mathbf{T}}_{l,l+1}^{he} & \hat{\mathbf{T}}_{l,l+1}^{hh} & -\hat{\mathbf{R}}_{l,l+1}^{he} & \hat{\mathbf{R}}_{l,l+1}^{hh} \end{bmatrix} \quad (\text{B.23})$$

Putting together all continuity and boundary conditions and introducing abbreviations results in a linear system of the same form as given in Equation (B.8). In case of PEC boundary conditions $\sigma^e = -1$ and $\sigma^h = 1$; in case of PMC boundary conditions $\sigma^e = 1$ and $\sigma^h = -1$; $\sigma^e = \sigma^h = 0$ for open boundary conditions. To solve the nonlinear eigenproblem for the eigenvalue λ and the eigenvector the matrix secant method described in Appendix B.5 is applied.

B.4. 1D Waveguide Modes

The wave equation to be solved in the computation of 1D slab waveguide modes with a propagation factor e^{ik_0vx} is¹

$$\partial_z \hat{a} \partial_z \phi + k_0^2 \hat{b} \phi = k_0^2 v^2 \hat{c} \phi \quad (\text{B.24})$$

The waveguide field is expanded in terms of shape functions: $\phi(z) = \sum_{j=1}^N C_j \varphi_j(z)$. The waveguide domain $[0, L_z]$ is subdivided into elements that are compatible with the material boundaries with a maximum size h_{\max} . The mathematical boundary conditions at $z = 0$ and $z = L_z$ are either Dirichlet (TE+PEC or TM+PMC) or Neumann (TE+PMC or TM+PEC). As shape functions φ_j local polynomials with a maximum degree p_{\max} which are compatible with the boundary conditions are employed. More specifically, linear hat functions and bubble functions with degree ≥ 2 are used.

¹ TE: $\phi = E_y$, $\hat{a} = \hat{c} = 1$, $\hat{b} = \epsilon_{rr}$; TM: $\phi = H_y$, $\hat{a} = 1/\epsilon_{rr}$, $\hat{b} = 1$, $\hat{c} = 1/\epsilon_{zz}$.

Within an element $z_1 \leq z \leq z_2$ of the mesh the following polynomials are chosen

$$f_0(\xi) = \frac{1-\xi}{2}, \quad f'_0(\xi) = -\frac{1}{2} \quad (\text{B.25})$$

$$f_1(\xi) = \frac{1+\xi}{2}, \quad f'_1(\xi) = \frac{1}{2} \quad (\text{B.26})$$

$$f_k(\xi) = \frac{P_k(\xi) - P_{k-2}(\xi)}{2}, \quad f'_k(\xi) = (k - \frac{1}{2})P_{k-1}(\xi) \quad \text{for } k \geq 2 \quad (\text{B.27})$$

where $P_k(\xi)$ are the Legendre polynomials and $\xi = \frac{2z-z_1-z_2}{z_2-z_1}$.

By applying a Galerkin scheme (i.e., using the ϕ_m 's as weight functions) one obtains the $N \times N$ generalized EVP

$$\sum_j E_{mj} C_{j\rho} = v_\rho^2 \sum_j V_{mj} C_{j\rho} \quad (\text{B.28})$$

with the banded (bandwidth $2p_{\max} + 1$), complex symmetric matrices

$$V_{mj} = \int dz \phi_m \hat{c} \phi_j \quad (\text{B.29})$$

$$E_{mj} = \int dz \phi_m \hat{b} \phi_j - \frac{1}{k_0^2} \int dz (\partial_z \phi_m) \hat{a} \partial_z \phi_j \quad (\text{B.30})$$

The number of DoFs N is determined by the domain size, h_{\max} , and p_{\max} . Since \mathbf{V} is invertible the EVP

$$\mathbf{V}^{-1} \mathbf{E} \vec{C} = v^2 \vec{C} \implies v_\rho, \vec{C}_\rho, \quad \rho = 1, 2, \dots, N \quad (\text{B.31})$$

is solved rather than (B.28). To ensure that v_ρ describes a mode either propagating or decaying in the $+x$ -direction the branch of $\sqrt{v_\rho^2}$ is chosen such that $\Re(v_\rho) + \Im(v_\rho) > 0$. The orthogonality relation $\int dz \phi_\rho \hat{c} \phi_\tau \propto \delta_{\rho\tau}$ holds for the waveguide modes. The discretized version reads $\sum_{j,k} C_{j\rho} V_{jk} C_{k\tau} \propto \delta_{\rho\tau}$. The electromagnetic field components of the waveguide modes propagating (or decaying) in the $+x$ -direction are as follows:

$$\text{TE:} \quad \vec{E}_\rho(x, z) = \begin{bmatrix} 0 \\ \phi_{y\rho}(z) \\ 0 \end{bmatrix} e^{ik_0 v_\rho x}, \quad \vec{H}_\rho(x, z) = \begin{bmatrix} \phi_{x\rho}(z) \\ 0 \\ \phi_{z\rho}(z) \end{bmatrix} e^{ik_0 v_\rho x} \quad (\text{B.32})$$

$$\text{TM:} \quad \vec{E}_\rho(x, z) = \begin{bmatrix} -\phi_{x\rho}(z) \\ 0 \\ -\phi_{z\rho}(z) \end{bmatrix} e^{ik_0 v_\rho x}, \quad \vec{H}_\rho(x, z) = \begin{bmatrix} 0 \\ \phi_{y\rho}(z) \\ 0 \end{bmatrix} e^{ik_0 v_\rho x} \quad (\text{B.33})$$

where the definitions

$$\phi_{y\rho} := \phi_\rho, \quad \phi_{z\rho} := v_\rho \hat{c} \phi_\rho, \quad \phi_{x\rho} := \frac{i}{k_0} \hat{a} \partial_z \phi_\rho \quad (\text{B.34})$$

have been applied. The Poynting vector $\vec{S}_\rho = \frac{1}{Z_0} \vec{E}_\rho \times \vec{H}_\rho^* + c.c$ takes the explicit form

$$\vec{S}_\rho(x, z) = \frac{1}{Z_0} \begin{bmatrix} \phi_{y\rho}^*(z) \phi_{z\rho}(z) \\ 0 \\ \phi_{y\rho}^*(z) \phi_{x\rho}(z) \end{bmatrix} + c.c. \quad (\text{B.35})$$

The optical power in mode ρ is

$$P_\rho = \frac{V_\rho}{Z_0} \sum_{j,k} C_{j\rho}^* \underbrace{\int dz \phi_j^* \hat{c} \phi_k}_{=V_{jk}^{\text{pow}}} C_{k\rho} + c.c. \quad (\text{B.36})$$

Since the slab waveguide structure has rotational symmetry around the z -axis (i.e., $\epsilon_{xx} = \epsilon_{yy} =: \epsilon_{rr}$) the waveguide modes can be rotated by an — in general complex valued — rotation angle ϑ :

$$\begin{aligned} \text{TE : } \quad \vec{E}_\rho &= \begin{bmatrix} -\sin \vartheta \\ \cos \vartheta \\ 0 \end{bmatrix} \phi_{y\rho} e^{ik_0 V_\rho (x \cos \vartheta + y \sin \vartheta)}, \quad \vec{H}_\rho = \begin{bmatrix} \phi_{x\rho} \cos \vartheta \\ \phi_{x\rho} \sin \vartheta \\ \phi_{z\rho} \end{bmatrix} e^{ik_0 V_\rho (x \cos \vartheta + y \sin \vartheta)} \\ \text{TM : } \quad \vec{E}_\rho &= \begin{bmatrix} -\phi_{x\rho} \cos \vartheta \\ -\phi_{x\rho} \sin \vartheta \\ -\phi_{z\rho} \end{bmatrix} e^{ik_0 V_\rho (x \cos \vartheta + y \sin \vartheta)}, \quad \vec{H}_\rho = \begin{bmatrix} -\sin \vartheta \\ \cos \vartheta \\ 0 \end{bmatrix} \phi_{y\rho} e^{ik_0 V_\rho (x \cos \vartheta + y \sin \vartheta)} \end{aligned}$$

B.5. Matrix Secant Method

The nonlinear eigenvalue problem solver is based on the matrix secant method [132]. The equation to be solved is

$$\mathbf{M}(\lambda) \vec{x} = 0 \quad (\text{B.37})$$

Linearization around λ_i where $\mathbf{M}(\lambda_i) =: \mathbf{M}_i$ is non-singular gives

$$\mathbf{M}(\lambda_i + \delta) \vec{x} \approx (\mathbf{M}_i + \delta \dot{\mathbf{M}}_i) \vec{x} = \delta \mathbf{M}_i \left(\frac{1}{\delta} \mathbf{I} + \mathbf{M}_i^{-1} \dot{\mathbf{M}}_i \right) \vec{x} = 0 \quad (\text{B.38})$$

We obtain the eigenvalue problem

$$\mathbf{M}_i^{-1} \dot{\mathbf{M}}_i \vec{x} = -\frac{1}{\delta} \vec{x} \quad (\text{B.39})$$

Replacing $\dot{\mathbf{M}}_i$ by $\frac{1}{\lambda_i - \lambda_{i-1}} (\mathbf{M}_i - \mathbf{M}_{i-1})$ results in the eigenvalue problem

$$(\mathbf{I} - \mathbf{M}_i^{-1} \mathbf{M}_{i-1}) \vec{x} = -\frac{\lambda_i - \lambda_{i-1}}{\delta} \vec{x} = \theta \vec{x} \quad (\text{B.40})$$

which is solved for the largest eigenvalue in magnitude θ_{\max} . Thus, $\lambda_{i+1} = \lambda_i + \delta = \lambda_i - \frac{\lambda_i - \lambda_{i-1}}{\theta_{\max}}$. To find the eigenpair corresponding to θ_{\max} the power method [133] is used.

B.6. Numerical Quadrature

For the numerical integration the highly efficient Gaussian quadrature was implemented [134]:

$$\int_{z_1}^{z_2} dz F(z) \approx \frac{z_2 - z_1}{2} \sum_{i=1}^N W_i F\left(\frac{z_1 + z_2}{2} + \frac{z_2 - z_1}{2} \xi_i\right) \quad (\text{B.41})$$

where ξ_i are the roots of the Legendre polynomial $P_N(\xi)$ and $W_i = \frac{2(1-\xi_i^2)}{[(N+1)P_{N+1}(\xi_i)]^2} = \frac{2}{(1-\xi_i^2)[P'_N(\xi_i)]^2}$. Polynomials up to degree $2N - 1$ are integrated exactly.

Curriculum Vitae

Name:	Paul Muellner / Paul Müllner.
Birth:	02.01.1973 in Vienna, Austria
Nationality:	Austrian
1979-1988	After four years elementary school, five years high school at 'Bundesrealgymnasium' Kandlgasse 39, 1070 Vienna.
1988-1993	Five years education as plastic engineer at TGM (Technologisches Gewerbe Museum, Vienna). Abitur/Matura passed with distinction.
1993-1994	Education as disposal engineer, passed with distinction.
1994-1995	Military service at the military brass band 'Gardemusik' as clarinetist.
1995-1996	Start of studies in Physics, University of Vienna.
1996-1998	Break of studies in physics, build up of a recording studio. Work as a sound engineer & producer.
1998-1999	Contributor to the 'Whitebook Project' of the market research company AC-Nielsen.
1999-2001	Editor for the Austrian computer magazine WCM, topics 'Professional Audio' & 'Multimedia'.
2001-2005	Continue studies in Physics, University of Vienna.
2005-2006	Master student at the AIT - Austrian Institute of Technology, department Health & Environment, Nano Systems. The Master thesis was entitled ' <i>Optimization of an Mach-Zehnder interferometric biosensor</i> ' at University of Vienna. Graduated with distinction.
2006-2010	PhD student at AIT - Austrian Institute of Technology, department Health & Environment, Nano Systems.
since July 2010	Junior scientist at the AIT - Austrian Institute of Technology, department Health & Environment, Nano Systems. Activities include simulation of planar photonic components, in particular of slot waveguide structures, and device characterization.
Additional education:	Education in quality controls. Generally accepted 'Q2' exam passed successfully in 1994.

Acknowledgment

Rainer Hainberger

Without you not even one page of this thesis would exist. Thank you for your wisdom, integrity and friendship over the years.

Roland Ottensamer

Thanks for pimping my (LaTeX) style.

Roman Bruck

Thank you for your professional and non-professional support.

My family and friends

I'm sorry that i could not spend the time with you during the last years that you would have deserved.

Judith Zenta

For your love and patience. You are the most incredible person i have ever met.